Carbon nanotube field emitter array and its application to novel X-ray systems

by

Yunhan Li

A thesis
presented to the University of Waterloo
in fulfillment of the
thesis requirement for the degree of
Doctor of Philosophy
in
Systems Design Engineering

Waterloo, Ontario, Canada, 2018

Examining Committee Membership

The following served on the Examining Committee for this thesis. The decision of the Examining Committee is by majority vote.

External Examiner:	Akintunde I. Akinwande Professor, Dept. of Electrical Engineering and Computer Science, Massachusetts Institute of Technology
Supervisor:	John T. W. Yeow Professor, Dept. of Systems Design Engineering, University of Waterloo
Internal Member:	Eihab Abdel-Rahman Professor, Dept. of Systems Design Engineering, University of Waterloo
Internal Member:	Ning Jiang Assistant Professor, Dept. of Systems Design Engineering, University of Waterloo
Internal-External Member:	Karim S. Karim Professor, Dept. of Electrical and Computer Engineering, University of Waterloo

This thesis consists of material all of which I authored or co-authored: see Statement of Contributions included in the thesis. This is a true copy of the thesis, including any required final revisions, as accepted by my examiners.

I understand that my thesis may be made electronically available to the public.

Statement of Contributions

I hereby declare that I have contributed to the majority of research work in this thesis. This thesis contains five co-authored articles. My contributions to these articles include design, fabrication, characterization, testing and analysis of carbon nanotube (CNT) field emitter array (FEA) and X-ray devices. Below is a list of selected publications:

1. A comprehensive review of CNT field emitters and CNT field emission (FE) technology.
   This work is presented in Chapter 2 and published in:
   Li, Yunhan, Yonghai Sun, and J. T. W. Yeow. Nanotube field electron emission: principles, development, and applications. Nanotechnology, 26(24):242001, 2015.

2. A novel field emission microscopy method to study CNT FEA.
   This work is presented in Chapter 3 and published in:
   Li, Yunhan, Yonghai Sun, David A. Jaffray, and John TW Yeow. A novel field emission microscopy method to study field emission characteristics of freestanding carbon nanotube arrays. Nanotechnology, 28(15):155704, 2017.

3. Fundamental understanding of CNT field emitter failure mechanism.
   This work is presented in Chapter 4 and published in:
   Li, Yunhan, Yonghai Sun, David A. Jaffray, and John TW Yeow. Coulomb explosion of vertically aligned carbon nanofibre induced by field electron emission. RSC Advances, 7(64):4047040479, 2017.

4. Design and fabrication of individually ballasted CNT FEAs using silicon current limiter.
   This work is presented in Chapter 5 and published in:
   Li, Yunhan, Yonghai Sun, David A. Jaffray, and John TW Yeow. Individually ballasted carbon nanotube field emitter arrays using silicon current limiter. (Submitted)

5. Design of self-focusing X-ray source based on CNT FEA and resonant transformer.
   This work is presented in Chapter 7 and published in:
   Yonghai Sun, **Li, Yunhan**, David A. Jaffray, and John TW Yeow. Self-focusing X-ray source based on carbon nanotube field emission cathode and resonant transformer. (Patent pending)

Abstract

With the emergence of ever more demanding X-ray imaging applications, including radiotherapy, radiography, computed tomography and tomosynthesis, there is a tendency to use field emission (FE) to take the place of thermionic emission in X-ray generation. Carbon nanotube (CNT) field emitter array (FEA) is able to provide enhanced current and low energy dispersion for X-ray generation. The low operating temperature, instantaneous response, and small size of CNT FEA enable efficient and controllable FE performance for high spatial and temporal resolution X-ray imaging and instantaneous switching among multiple X-ray sources. Challenges are still remaining for CNT FEA study and development. The first is the insufficient understanding of FE uniformity of CNT FEA and CNT emitter failure mechanism, which limits the development of stable and reliable CNT FEA. The second is the lack of applications of CNT FEA for the emergence of novel X-ray imaging applications that require dose adjustments, fluence field modulation, and shape variation.

In this thesis, recent advances in CNT FE and field emitters are comprehensively reviewed. Issues related to the principles, characteristics, and applications of CNT based FE are discussed. The research starts with a fundamental study of understanding the FE uniformity and emitter failure mechanism of CNT FEA by designing and demonstrating a simple and reliable field emission microscopy method using PMMA (Poly (methyl methacrylate)) thin film with microscopic camera. This novel approach is able to resolve the challenges of observing FE uniformity of CNT FEA and CNT field emitter failure behaviour. The unique phenomenon of light emission and Coulomb explosion of CNT field emitter failure induced by FE is represented and systematically characterized, which is a combined effect of Joule heating and excessive charging. Then, individual ballast of vertically aligned CNT FEA using silicon current limiters is designed and fabricated, which exhibits improved reliability and stability. The CNT FEA is applied to a low-cost self-contained and self-focusing compact X-ray source integrated with resonant transformer. The X-ray source can be powered by low voltage to generate pulsed X-ray and achieve sub-millimetre resolution. Using finite element analysis and Monte Carlo simulation, CNT FEA based two dimensional multi-pixel X-ray source is designed and experimentally verified, which is feasible for X-ray fluence field modulation in next generation X-ray imaging systems.

Acknowledgements

Firstly, I would like to express my sincere gratitude to my supervisor, Prof. John T. W. Yeow. Five years ago, it was your wonderful presentation in Xi'an, China that brought me into the wonderland of nanotechnology. Thank you for offering me the opportunity to work in your energetic and innovative group to embark on my Ph.D. journey. Your thoughtful questions always enlightened me when I hesitated and led me academically. Your comments on my manuscripts were always of great help for improving my research quality. I am also grateful for supporting me all the equipment, materials, and clean-room access.

Secondly, I want to thank my committee members: Prof. Eihab Abdel-Rahman, Prof. Karim Karim, and Prof. Ning Jiang, for being there when I had questions. Your insightful questions and patient guidance during my comprehensive exams enabled me to improve my work significantly. I sincerely thank Prof. Akintunde Akinwande for acting as the external examiner and travelling to Waterloo to attend my thesis defence. Prof. Akinwande gave a very careful examination on my thesis, providing lots of thoughtful comments and pointing out some mistakes accurately. I am very grateful for all the work he has done to improve the quality of my thesis.

Thirdly, I would like to thank Dr. Fred Sun for the consistent help during my Ph.D. career. Thank you for providing lots of technical supports and constructive advices on my experiments. Thank you for sharing your idea and knowledge with me. I could not have completed my Ph.D. project without your assistance. Also, I would like to thank Dr. Gregory Bootsma for helping me with Monte Carlo simulation on X-ray fluence field. My research will not be possible without the Quantum NanoFab team, the Engineering Student Machine Shop, the Waterloo Institute for Nanotechnology, and the Department of Systems Design Engineering of the University of Waterloo. I am grateful for the great efforts from the staffs of the Quantum Nanofab in maintaining the lab equipment and making the lab an enjoyable place to work in. I would like to particularly thank Dr. Nathan Nelson-Fitzpatrick for answering me numerous questions on nano-fabrication.

My Ph.D. experience was enjoyable because of all the lab members and friends that I met. Specially thank Zhou Xu for picking me at the airport and treating me like your family member. Your kindness and reception helped me overcome the loneliness and the homesickness in my first year in Canada. Thank Shruti Nambiar for pushing me and helping me in my first year research.

I would also like to thank Siyuan, Chen, and Chengpei for being my good friends in Waterloo. I will never forget those happy moments with you. For all the lab members, I will always cherish my time in the lab together with you.

I am forever indebted to my parents, Xianhui Xie and Chongxue Li, for the unconditional love and support. You are my source of strength and inspiration.

The last words of the acknowledgement I would save for my beloved wife, Sainan He. Thank you so much for your love over the past 12 years. I could not have been able to make it this far without your companion throughout my Ph.D. career. I am a much happier, better, and more confident man because of you. I am also very grateful for the trust and support from my parents-in-law.

Dedication

To my parents.

Table of Contents

List of Tables

List of Figures

Abbreviations

2D two-dimensional 26

3D three-dimensional 26

AC alternating current 15

AFM atomic force microscopy 55

CMP chemical mechanical polishing 20

CNT Carbon nanotube 3

CT computational tomography 1

CVD chemical vapour deposition 15

DBT digital breast tomosynthesis 27

DC direct current 6

DRIE deep reactive ion etching 78

EBL electron beam lithography 11

EDS energy-dispersive X-ray spectroscopy 55

EGS Electron Gamma Shower 118

EPD electrophoresis deposition 15

F-N Fowler-Nordheim 11

FE Field emission 2

FEA field emitter array 3

FEM field emission microscopy 5

FFMCT fluence field modulated computational tomography 2

HIM scanning helium ion microscopy 43

HSQ hydrogen silsesquioxane 78

IGRT image guided radiation therapy 28

IPA isopropyl alcohol 16

MC Monte Carlo 117

MIBK methyl isobutyl ketone 34

MOSFET metal-oxide-semiconductor field-effect transistor 23

MWNT multi-walled carbon nanotube 16

NDT non-destructive testing 23

PECVD Plasma-enhanced chemical vapour deposition 18

PMMA poly(methyl methacrylate) 5

RIE reactive ion etching 20

SEM scanning electron microscopy 11

SPICE Simulation Program with Integrated Circuit Emphasis 93

SWNT single-walled carbon nanotube 16

TEM transmission electron microscopy 11

TMAH tetramethylammonium hydroxide 78

UHV ultra-high vacuum 13

Chapter 1

Introduction

1.1 Motivations

The discovery of X-ray and the development of X-ray imaging greatly facilitate advances of medical diagnosis and treatment in many aspects such as non-invasive and painless diagnosis disease, guiding surgery, and monitor of therapy. The applications of X-ray imaging technology in medical area includes but not limited to radiography, computational tomography (CT), tomosynthesis, imaging guidance, and radiotherapy. Despite the benefits of the X-ray imaging technology, there are still many drawbacks. Existing medical imaging modalities using X-ray suffer from unwanted ionizing radiation, moving-induced blurry in CT, and poor temporal resolution causing long data acquisition time. The unwanted radiation ionization during CT inspection can potentially cause cell damage and risk of cancer. One study estimates that on the order of 2% of future cancers in the USA may be attributable to radiation from current CT scanning procedures [1]. Nevertheless, balancing the benefits and risks of X-ray imaging, enhancing temporal and spatial resolution, and achieving rapid X-ray beam adjusting and pulsing continue to be challenges. In fact, all the issues in the existing X-ray imaging applications are inherently associated with the electron source used.

In conventional X-ray sources, thermionic emission of electrons from a heated tungsten filament is used to generate X-rays. Since thermionic emission needs to work at a high temperature,

it is energy consuming and slow in response. The excessive power dissipation of the thermionic emission often leads to destructive of the X-ray system. The large electron emission size requires complex focusing components. The lagging response of feedback controls In other words, it is the inherent drawbacks of the thermionic emission that cause the issues of the existing X-ray imaging applications.

With the emergence of ever more demanding medical and inspection techniques, including stationary tomosynthesis and X-ray fluence field modulation, there is a tendency to use Field emission (FE) to take the place of thermionic emission in X-ray generation. FE is a process of extracting electrons from a solid tunnelling through the surface potential barrier into vacuum by applying an electrostatic field. It provides more enhanced current and lower energy dispersion than thermionic emission. The electrons can be extracted from the field emitters instantly when an electrostatic field is applied. When compared with thermionic emission, FE has several intrinsic advantages over thermionic emission such as low operating temperature, instantaneous response, and small size. The electron extraction is more efficient and controllable as well. By exploiting these advantages, X-ray imaging based on FE have the potential for high spatial and temporal modulation. Besides, FE enables rapid switching among multi-pixel X-ray sources, which can replace the mechanical component of the conventional thermionic X-ray source in CT imaging. As a result, two major challenges of the modern CT imaging, motion-induced blur and long scanning time, can be resolved.

In addition, the idea behind the traditional X-ray dose management is to use an extra tool to either shape a filter to selectively attenuate the cone X-ray beam or dynamically vary an aperture to adjust exposure time. CT imaging system using X-ray fluence field modulation is called fluence field modulated computational tomography (FFMCT). This approach can benefit many cases when high image quality near the suspicious lesion is only desired such as locating the tip of a surgical instrument with respect to an anatomical landmark and a repeat diagnostic CT scan to explore a suspicious anomaly. However, filters and/or collimator that are fixed in the field of view throughout the CT scan are greatly limited in their ability to compensate for the complex heterogeneity of attenuation presented by real patient anatomy across the incident X-ray field. Besides, filters and collimator are made from high atomic number materials such as tungsten, which make these tool heavy and inflexible. Therefore, flexible fluence delivery is desired to

manage complex changes in attenuation across the field of view which can change significantly for different projection angles.

Carbon nanotube (CNT) was discovered in 1991 and its FE property was first reported in 1995 [2, 3]. Since then, CNT has been regarded as an ideal type of field emitters due to its outstanding high aspect ratio, high mechanical and chemical stability, high electrical and thermal conductivity, enhancing electron emission performance [4–6]. When comparing with CNT film emitters, defined patterned vertically aligned CNT field emitter array (FEA) are expected to have high FE efficiency and uniform FE current because of their relatively uniform geometry and less screen effect [7–9]. In the meantime, realizing stable and reliable CNT FEAs for more demanding applications continues to be a challenge. As a type of nano-material, CNT field emitters tend to have dissimilar size and morphology in CNT FEAs. It is understood that even a small variations in the tip radii or emitter heights of the FEA will result in a large variation in the local electric field enhancement among the tips and a large variation of FE current from each emitters [10]. Consequently, such unequal FE current contributions from emitters within a CNT FEA at a given control voltage leads to dominating CNT emitters overcurrent and irreversibly degraded [11, 12]. Therefore, CNT FE based cathode has not been widely applied for next generation X-ray imaging due to its non-uniform FE and short life-time.

Unfortunately, FE uniformity and the mechanism of emitter failure of CNT FEAs have not been well studied due to the difficulty of observing and quantifying FE performance of each emitter in CNT FEAs. For example, how uniform FE can a CNT FEA achieve; how much a CNT emitter can contribute to the overall FE performance; when a CNT emitter is active and damaged? Besides, the behaviour and mechanism of vertically aligned CNT field emitter failure induced by FE is still insufficiently studied, which is often simply attributed to uprooting or burnout of CNT emitters [12–14]. Thus, a better understanding of the FE uniformity of CNT s and CNT emitter failure mechanism is of great significance to optimize CNT FE devices for practical applications. Furthermore, there has been little to no work on effectively and straightforward individually ballasted CNT FEA to achieve stable and reliable FE performance. One main reason for the lack of previous work is the fabrication complexity. These challenges are limiting the development of potential applications such as, compact X-ray source, multi-beam X-ray sources, and X-ray fluence field modulation.

The first motivation behind the work of this thesis is to resolve the challenges of characterizing FE uniformity of CNT FEA, understanding of CNT emitter failure mechanism, and developing stable and reliable CNT FEA for the emergence of demanding X-ray imaging applications. Our group has been committed to developing CNT FEA based FE cathode with coaxial cylinder gate electrode to replace conventional hot filament as electron source. However, such CNT based FE cathode needs further investigation and optimization before applied to practical applications. The second motivation is to develop novel X-ray systems by exploiting the advantages of CNT FE technology such as compact X-ray source and FFMCT. Despite many of its advancements, a main disadvantage of CT is that it employs ionizing radiation in order to image a patient, which can potentially damage cell and increase cancer risk. Therefore, improving a better performance of CT but maintaining reasonable radiation exposure to limit unnecessary dose to patients is a development tendency of CT. The idea behind the traditional X-ray fluence field modulation is to use an extra tool to either shape a filter to selectively attenuate a cone X-ray beam or dynamically vary an aperture to adjust exposure time. Contrary to the fixed filtration patterns in conventional use, CNT FE based X-ray source has a capability of delivering spatially varying, user-prescribed X-rays but "as low as reasonably achievable" radiation exposure to limit unnecessary dose and cancer risk to patients without sacrificing image quality with limited dose. As a result, a heavy and inflexible filter/collimator can be eliminated. However, investigations on applying CNT FE for X-ray image dose adjustments, fluence field modulation, and shape variation are rarely reported. Therefore, to develop novel X-ray imaging system taking the advantages of CNT FE is worth of investigating.

1.2 Objectives

The ultimate goal of this study is to demonstrate a multi-pixel X-ray source based on well designed CNT FEA cathode to achieve flexible X-ray fluence field modulation for future X-ray imaging. To achieve it, this study will break down into four secondary objectives. The first objective is to develop a proper method that is able to observe and quantify the FE performance of each emitter in a CNT FEA. With this method, we are are able to provide a direct observa-

tion of FE uniformity of CNT FEAs and CNT field emitter failure induced by FE in CNT FEA. The second objective is to explore CNT field emitter failure behaviour induced by FE and understand its mechanism. Based on the FE uniformity and CNT field emitter failure mechanism study, the third objective is to design and fabricated individual ballast of vertically aligned CNT FEAs to improve the reliability and stability for X-ray fluence field modulation applications. The fourth objective is to integrate the proposed CNT FEA cathode in to X-ray source and explore the feasibility of X-ray fluence field modulation using CNT FE based technology.

1.3 Contributions

The first contribution of this study is developing a simple and reliable field emission microscopy (FEM) method using poly(methyl methacrylate) (PMMA) thin film to observe and quantify the FE performance of each emitter in a CNT FEA. In a CNT FEA, various FE currents from emitters lead to a different degree of electron exposure on a PMMA thin film. Utilizing these features, we are able to observe the FE current from each CNT emitter as a different morphology of FEM patterns on the PMMA thin film. In this way, the overall FE uniformity of the CNT FEA and FE current contribution from each emitter can be visualized and quantified. Any emitter can be located corresponding to its own FEM pattern. The relationship between CNT morphology and corresponding FE performance is built according to the FEM pattern on the PMMA thin film. The proposed approach is expected to resolve the major challenge of building the relationship between CNT FE performance and emitter morphology from three aspects: observation and quantification of FE uniformity of CNT FEAs, locating any CNT emitter from a CNT FEA corresponding to its FEM pattern, and real-time FE performance study.

The second contribution is representing the entire process of CNT field emitter failure and providing a deep understanding of its mechanism. CNT emitter failure process is successfully observed, which exhibits a light emission followed by an explosion. Starting with the direct observation of the unique behaviour by a microscopic video camera, a systematic characterization of the CNT emitter failure process using the PMMA thin film based FEM method combined with various techniques is performed. Finite element analysis and theoretical study are carried out to

explore the effect of Joule heating on the FE and the CNT explosion. The explosion of CNT, a combined effect of Joule heating and excessive charging, is characterized by the size and shape of the explosion impacts on the PMMA thin film, sputtered PMMA by charged fragments,and the melted area in the explosion centres. The detailed study of CNT emitter failure induced by FE allows an insight of destruction of other nanowires during electrical transport and a systematic design of FE devices for long-lasting operation in practical applications.

The third contribution is designing and fabricating the individual ballast of vertically aligned CNT FEAs using silicon current limiters. Each CNT emitter is patterned and synthesized in series with a well-designed silicon current limiter. Vertically aligned CNT field emitter is individually ballasted by using silicon current limiter to achieve uniform and long-lasting operation without compromising high FE efficiency and current level. However, there has been little work on individually ballasted CNT FEA using this approach. One main reason for the lack of previous work is the fabrication complexity. The systematic design and the successful development of individually ballasted CNT FEAs using silicon current limiter will enable stable and reliable operation of commercially viable CNT FEA as an electron source for applications such as miniature X-ray source and multi-beam X-ray source.

The fourth contribution is integrating the CNT FEA cathode into X-ray system. One type of X-ray source is a self-contained and self-focusing compact pulsed X-ray source based on a resonant transformer. By integrating CNT FEA with a resonant transformer, the X-ray source can be powered by a 12 V direct current (DC) power supply to have a sub-millimetre scale resolution. The X-ray source is able to generate pulsed X-ray beam. Self-focusing of the electron beam has successfully achieved by the magnetic field generated by the resonant transformer. The highly simplified structure of the X-ray source not only can increase reliability but also can reduce the cost of the device significantly. The proposed X-ray source enables the development of novel applications such as X-ray fluence field modulation, and multiple source X-ray systems for medical and industrial applications.

1.4 Thesis organization

This dissertation is organized in eight chapters.

Chapter 2 presents the background review on electron emission theory, CNT field emitter, recent advances in CNT FE based X-ray sources, and X-ray fluence field modulation.

Chapter 3 introduces a novel and effective FEM method based on PMMA thin film to study the FE uniformity and CNT emitter failure of free-standing CNT FEAs.

Chapter 4 represents the entire process of CNT field emitter failure and performs a systematic characterization of the CNT emitter failure process using the PMMA thin film based FEM method combined with various techniques.

Chapter 5 demonstrates a comprehensive design and fabrication of individually ballasted CNT FEAs using silicon current limiter.

Chapter 6 describes a self-contained and self-focusing compact pulsed X-ray source integrated with a vertically aligned CNT FEA cathode and a resonant transformer.

Chapter 7 provides a comprehensive design and feasibility study of two-dimensional multi-pixel X-ray source for X-ray fluence field modulation.

Chapter 8 is the summary of the thesis and future work.

Chapter 2

Background

2.1 Electron emission

Electron sources are basic components in many scientific and industrial devices, such as electron microscopes, microwave amplifiers, displays, cathode ray tubes and X-ray sources. There are two principal methods for emitting electrons from the surface of a material: thermionic emission and FE. Thermionic emission is the emission of electrons over a potential energy barrier from a material induced by heat, while FE is emission of electrons induced by applying an electrostatic field. These two electron emission processes can be explained on the basis of the FermiDirac distribution for a free electron gas in the metal and the classical image force barrier at the surface. Figure 2.1 shows the potential energy of electrons near the metal surface and the principles of different types of electron emission from metal. A general theoretical description of electron emission was provided by Murphy and Good [15] and later verified experimentally by Christov and Vodenicharov [16] for a wide range of surface electric fields and temperatures. The temperature determines the distribution of electrons and the electric field affects the shape of the surface barrier.

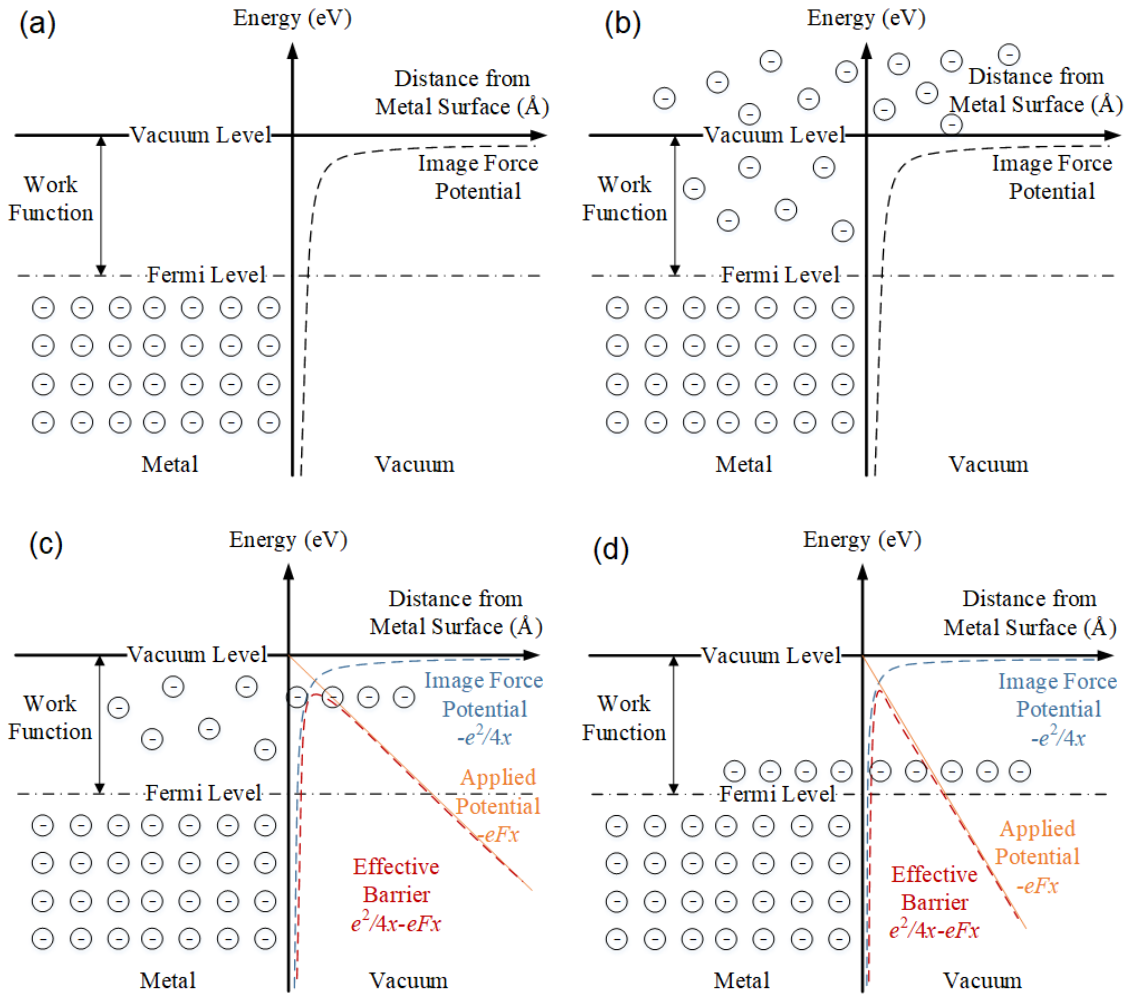

Figure 2.1: Schematic diagram of (a) electrons near the metal surface, (b) thermionic emission, (c) Schottky emission, and (d) FE.

2.1.1 Thermionic emission

In a solid, electrons tend to fill the lowest energy state. At room temperature, free electrons in metals possess inadequate energy to escape from the metal surface (Figure 2.1(a)). As the temperature of the material increases, the average energy of free electrons increases. When

the electrons acquire more energy than the work function of the metal, they will overcome the restraining surface barrier and leave the metal surface. The classical example of thermionic emission is the emission of electrons from a hot cathode into a vacuum (also known as the Edison effect) in a vacuum tube. For thermionic emission, emission over the barrier predominates and the temperature dependence of the distribution function is mainly responsible for variations in the emitted current (Figure 2.1(b)). The theoretical treatment of thermionic emission leads to the Richardson-Dushman Equation [17].

$$J = \lambda_R A_0 T^2 e^{-\frac{\varphi}{\kappa_B T}} \tag{2.1}$$

where J is the emission current density; T is the temperature of the metal; φ is the work function of the metal; κ_B is the Boltzmann constant; λ_R is a material-specific correction factor that is typically of order 0.5. Because of the wave-like nature of electrons, some proportion r_{av} of the outgoing electrons will be reflected as they reach the emitter surface, so the emission current density will be reduced and λ_R will have the value (1-r_{av}) [18]; and A_0 is a universal constant given by:

$$A_0 = \frac{4\pi m k^2 e}{h^3} = 1.20173 \times 10^6 \ \mathrm{A \cdot m^{-2} \cdot K^{-2}} \tag{2.2}$$

where m and e are the mass and charge of an electron and h is Plancks constant. Usually, a V-shape tungsten filament or a lanthanum hexaboride (LaB_6) works as a thermionic emission cathode.

2.1.2 Schottky emission

In electron emission devices there is an applied voltage on the anode and thus an electric field of E is created between the anode and the cathode. This electric field accelerates all the electrons from the cathode, but it also influences the emission surface. Without the field, the surface barrier seen by an escaping Fermi-level electron has a height φ equal to the local work function. The surface barrier is decreased by the electric field at an amount $\Delta\varphi$ and thus the emission current is increased. This is known as the Schottky effect or field enhanced thermionic emission (Figure 2.1(c)). It can be modeled by a simple modification of the Richardson-Dushman equation,

replacing φ by $(\varphi - \Delta\varphi)$, which results in the equation [19, 20]:

$$J = \lambda_R A_0 T^2 e^{-\frac{\varphi - \Delta\varphi}{\kappa_B T}} \tag{2.3}$$

$$\Delta\varphi = \sqrt{\frac{e^3 E}{4\pi\varepsilon_0}} \tag{2.4}$$

where ε_0 is the vacuum permittivity. This modified equation is often called the Schottky emission. It is relatively accurate for electric field strengths lower than 100 $\mathrm{V}\cdot\mu\mathrm{m}^{-1}$. For electric field strengths higher than 100 $\mathrm{V}\cdot\mu\mathrm{m}^{-1}$, so-called Fowler-Nordheim (F-N) tunnelling begins to contribute significantly to the emission current. Therefore, the Schottky emission can be divided into thermal enhanced FE and field enhanced thermionic emission, depending on the difference of the operating electric field and temperature. Schottky emission cathodes have many advantages over thermionic emission cathodes. For example, small effective source radius, high brightness, long lifetime and narrow electron energy distribution. They are widely used as point sources in electron devices and techniques, such as scanning electron microscopy (SEM), transmission electron microscopy (TEM), and electron beam lithography (EBL).

2.1.3 Field emission

FE is a process of extraction of electrons from a solid by tunneling through the surface potential barrier when an electrostatic field is applied. Unlike thermionic emission and Schottky emission, no heat is required for obtaining electrons in FE. The emission current depends directly on the local electric field at the emitting surface E, and its work function φ, as shown in Figure 2.1(d). In FE, electrons with energy below or close to Fermi level predominates and the emission current variation is determined by the field dependence of the barrier shape. The phenomenon of field electron emission was first discovered by R.W. Wood in 1897 from platinum [21]. Initial theoretical insight into this phenomenon was explained by W. Schottky in 1923 [22]. This phenomenon was explained by quantum tunneling of electrons through the surface potential barrier and a theory was developed by R.H. Fowler and L.W. Nordheim in 1928 [23]. In this theory, the system is simplified as a one dimensional structure along the direction of the external electric field. The emission tip is modelled as a semi-finite quantum well with the work function

of φ, and the applied electric field E, is approximated as a linear potential. By employing the Wentzel-Kramers-Brillouin approximation, the following F-N equation was obtained:

$$J = 6.2 \times 10^{-6} \frac{\mu^{1/2}}{\left(\mu + \varphi^{1/2}\right) \varphi^{1/2}} (\beta E)^2 \exp\left(-6.8 \times 10^7 \frac{\varphi^{3/2}}{\beta} E\right) \tag{2.5}$$

where J is in amperes per square centimeter of emitting surface; μ is the parameter of the electron distribution in Fermi-Dirac statistics, which is in volts; E is in volts per centimetre; The emitter tip is geometrically sharp and the electric field is intensified at the tip end, producing a much higher local electric field than the applied electric field. Thus, β here is the field enhancement factor, which is the ratio between the local and the applied field. For the nanotubes, β typically ranges between hundreds and thousands. In the original paper of F-N equation, Equation 2.5 is given with the numerical mistake of 2.1×10^8 instead of 6.8×10^7. This correction is important and favours satisfactory interpolation of the experimental results [24]. The F-N equation shows that the dependence of the emitted current on the local electric field and the work function is exponential-like. As a consequence, a small variation of the shape or surrounding of the emitter (geometric field enhancement) and/or the chemical state of the surface has a strong impact on the emitted current.

In 1929, R.A. Millikan and C.C. Lauritsen established linear dependence of the logarithm of current density on $1/E$ [25]. Reordering the Equation 2.5 results in the well-known F-N plot:

$$\ln\left(\frac{J}{E^2}\right) = a - 6.8 \times 10^7 \frac{\varphi^{3/2}}{\beta E} \tag{2.6}$$

The above equation gives $\ln(J/E^2)$ versus $1/E$ plot a straight line. The slope, m, of the F-N plot should be $m = 6.8 \times 10^7 \varphi^{3/2}/\beta$. Therefore, the field enhancement factor β can be extracted when work function is known [24, 26]. Theory of FE considered in details in recent books [22]. By 1930 basic physical understanding of the FE from bulk metals had been achieved with F-N equation derived. Initially, F-N theory was developed for FE from bulk metals and other bulk crystalline solids, but they are more frequently used as an approximation to identify and analyse FE from other materials. Up till now, F-N theory is still the criterion to identify FE and the tool to analyse FE performance from a material. FE occurs when the electric field strength is at the

scale of 10^9 $\mathrm{V \cdot m^{-1}}$. In order to produce such high electric fields, the emitter is usually formed into a tiny tip, which has an apex radius ranging from several nanometres to sub-micrometers. The electric field at the emitter tip narrows the potential barrier at the metal-vacuum interface to several nanometres. Therefore, the free electrons in the metal have a significant probability of tunnelling from the solid into the vacuum.

In FE, the electrons can be extracted from the field emitters instantly when an electrostatic field is applied. Compared with thermionic emission, FE has several intrinsic advantages such as low operating temperature, instantaneous response, and small size, which make electron extraction more efficient and controllable.

2.2 CNT field emitter cathode for X-ray sources

2.2.1 Development of field emitters

FE theory and field emitters have been researched for almost a century, but its applications still remains to be developed compared to thermionic emission counterparts. The reason is mainly due to the lack of the field emitters with stable FE performance and low cost of fabrication. Typical examples were Spindt-type FEAs [27,28] and silicon FEAs [29], which were primarily developed for field emission display staring from 1960s and 1970s. Spindt-type FEAs are fabricated using thin-film deposition and etching techniques together with EBL to build conical molybdenum or tungsten emitters on a silicon substrate. However Spindt-type emitter made of metal that is more active to heat, chemical reaction and ion bombardment. Thus, Spindt-type field emitters need ultra-high vacuum (UHV) conditions (1×10^{-8} Torr or lower) to minimize residual gas effects on the FE performance degradation [30].

Silicon field emitters is a potential alternative for Spindt-type field emitters due to the availability of silicon fabrication lines for integrated circuits industry. Silicon-based microfabricated FEAs were demonstrated in 1972 by Thomas et al. [29]. In 1980s, a series of studies on using silicon field emitters as cold cathode was carried out. Fabricating silicon FEA became well developed during that period using etching and oxidation sharpening techniques [31]. Research

on silicon FEA continues in 1990s [32, 33] and 21st century [34, 35]. Efforts on further improving the stability and uniformity are also reported [36–38]. Figure 2.2 shows a typical silicon FEA with individually ballast structure using silicon pillar current limiters [38]. Silicon FEAs were primarily developed for FED staring from 1970s. In 2010s, silicon FEAs are also reported to be as the electron source for X-ray generation such as portable X-ray source and low-Bremsstrahlung X-ray source [39, 40]. One drawback of silicon field emitters is the low melting point of silicon. Since Joule heating is commonly induced by FE, high FE current level or long time of FE operation would cause silicon field emitters melting, thus leading to device failure.

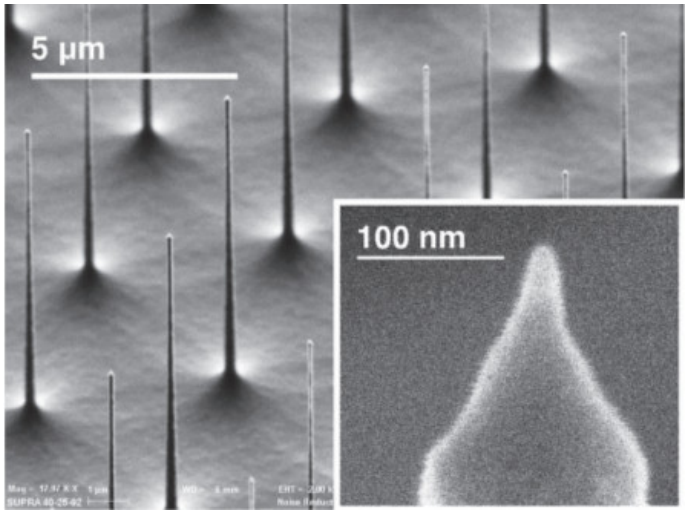

Figure 2.2: An SEM image of a typical silicon FEA with individually ballast structure using silicon pillar current limiters. (© 2012 IEEE)

Many other materials were studied as field emitters such as diamond thin film [41] and FEA [42], tungsten FEA [43, 44], zinc oxide nanowire emitters [45], and many other nanostructured semiconductor field emitters [46]. However, they are not well studied as Spindt-type field emitters or silicon field emitters. Besides, since the its FE property was first reported in 1995 [3], the study of FE and its applications turned to focus on CNT.

2.2.2 CNT field emitters

Compared with metallic Spindt-type field emitter and other field emitters, CNT has many advantages for FE: the high electrical and thermal conductivity, the chemical stability, the high aspect ratio, and small in size. Detailed information about CNT properties and CNT synthesis methods can be found in [47–56]. Increasing interest on CNTs FE applications has been aroused since the FE property was first reported in 1995. Because of the high aspect ratio, the field enhancement factor of CNT emitters is very large.

There are two forms of CNT field emitters. One is a pointed electron source consisting of a single CNT. While the other is a FE cathode with either CNT film or well-patterned CNT FEAs. The former is suitable for the formation of finely focused electron beam primarily applicable to fundamental research, high-resolution electron microscopy or lithography [57]. However, since a single CNT can provide only a few microamps of emission current [58], CNT thin films or free-standing vertically aligned CNT EFAs are employed to achieve sufficient current for X-ray generation. Free-standing vertically aligned CNT FEA cathodes are expected to allow higher FE efficiency and more uniform emission current because of their relatively more uniform geometry than CNT film cathodes [7, 8, 59, 60].

CNT thin film emitters

CNT film emitters can be prepared either by deposition or coating of pre-produced CNTs on a substrate, including spray coating, screen coating, and electrophoresis deposition (EPD), or by direct growth using chemical vapour deposition (CVD) technique [61–63].

Spray coating method to prepare CNTs films with various densities can be achieved by spraying CNTs suspension, which is made by CNTs dispersed in a solvent, onto a substrate. Screen printing method is to crush and mix CNTs with binders and surfactant to prepare pastes or slurries. The CNT concentration can be adjusted by adding conductive fillers or binders. After printing, CNTs films are heated at high temperature to vaporize the organic binders and to form electrical and mechanical contact between CNT field emitters and the metal electrode on the substrate. Yamamoto reported alternating current (AC) electrophoresis method to use coplanar

aluminium electrodes with an AC voltage of 80 V to evaporate in isopropyl alcohol (IPA) from a CNT suspension at room temperature [64]. The suspension is prepared by CNT ultrasonically dispersed in IPA. Choi et al deposited single-walled carbon nanotube (SWNT) by electrophoresis onto a patterned metal cathode for triode-type FED [65]. S. J. Oh reported a liquid-phase room temperature EPD method for fabrication of patterned CNT films, using CNTs produced by laser ablation method dispersed in OmniCoat SU-8 release [66]. CNT film emitter made with coating or deposition have a good uniformity, but the adhesive of the CNT to the substrate is sometimes not strong enough. CNTs can easily be peeled off from the substrate and lead to the emitter failure. Besides, problems of CNT film FE including short lifetime at high current density or high voltage, poor FE uniformity, and pixel-to-pixel inconsistency still remains to be solved [62]. To improve the adhesion of CNTs and the substrate based on the previous reported fabrication method in [66], researchers added glass frits as a binders into the EPD ink [62]. Also, they use an activation process, which is mechanically removal of a top surface layer of the composite film using an adhesive tape to make the CNTs vertically aligned [62], which is helpful for improving the field enhancement factors. CNT thin film FE cathode based on the above-mentioned coating method is already available commercially to be applied to some devices.

Direct growth of CNT thin film or "forest" on a cathode substrate using CVD technique offers the advantage of scalability for production. This method is based on the decomposition of a hydrocarbon gases over a catalytic metal to produce multi-walled carbon nanotube (MWNT) forest either randomly or vertically. The random CNT forest has a similar shape and similar field emission properties with those of the coated CNT film discussed above. Patterned CNT films can be obtained by controlling the catalyst deposition using standard lithographic techniques such as photo lithography and EBL. The vertical alignment of CNT forest grown by thermal CVD relies on a crowding effect and van der Waals interactions between the side wall of neighboring CNTs. Besides, thermal CVD always yields very dense spaghetti-like CNT forests that are densely aligned together. During the FE process, the electric field on one tube is screened by the proximity of neighboring tubes [67, 68].

Figure 2.3 shows a typical CNT thin film field emitter cathode [62]. Fabrication of CNT thin film cathodes by coating of pre-produced CNTs on a substrate is simple and cost saving but have several drawbacks. Firstly, CNT emitter film prepared by this method can easily be

peeled off from the substrate in electric field, causing FE failure. Thus, binders are needed to improve the adhesion of the CNT emitter film. Secondly, since CNT emitters are distributed into a suspension before curing, not all CNT film emitters are protrude out of the substrate, resulting in low efficiency of FE. Thirdly, for CNT film cathode using an external metal grid as the gate electrode, the emitter-gate gap is usually on the order of hundreds of microns, which results in very high control voltage (several kilovolts) for electron extraction. In addition, since the height of activated CNT emitters are random, which means the distance from the emitters tips to the gate electrode are various from tip to tip. The various distance will cause non-uniform FE. The taller emitters suffers from higher electric field and thus higher emission current than the shorter ones, which is more likely to be damaged.

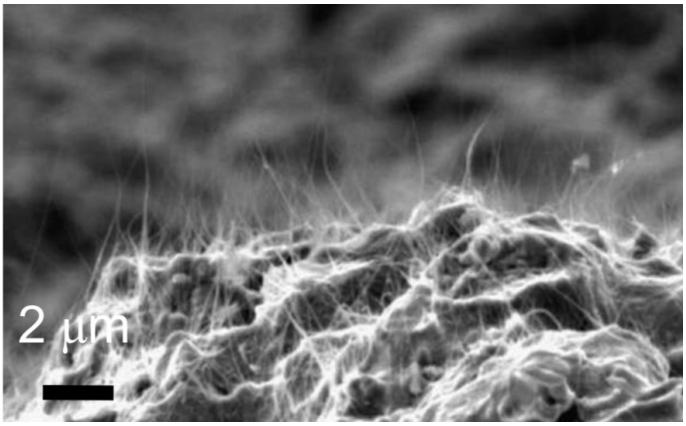

Figure 2.3: An SEM image of a typical CNT thin film field emitter cathode. (Reprinted with permission from IOP publishing via Copyright Clearance Center)

Vertically aligned CNT FEA

In order to achieve high FE current and high FE efficiency for practical applications, vertically aligned, spaced apart, well-patterned, and geometrically uniform CNT FEAs are desired. Patterned CNT emitters are important for applications that require individual addressable electron emission sources such as FED, FE based X-ray stationary computational tomosynthesis, and etc. Compared SWNT and MWNT with that can only be synthesized into very dense nanotube

forests for FE applications, such CNT FEA has a large number of exposed emitter tips and the well-controlled geometry to avoid screening effect [10, 68–71]. Plasma-enhanced chemical vapour deposition (PECVD) is used to selectively grow free-standing vertically aligned CNTs on pre-patterned catalyst sites using EBL. Such CNT field emitters have features such as the same dimensions, a constant pitch, and one CNT at each site to give a uniform and reproducible performance. Typical vertically aligned CNT FEA is fabricated by PECVD of acetylene and ammonia at 700 °C at precisely positioned nickel (Ni) catalyst dots [7, 72–74]. In the CNT FEA, each patterned catalyst site has a single vertically aligned CNT emitter with well-controlled size and a tubular conical structure. Figure 2.4 shows a typical free-standing vertically aligned CNT FEA synthesized using PECVD from our group. The CNT emitters consist of stacked curved graphite layers that form tubular cones with bamboo-type axial [8, 60]. This type of CNT is classified as a type of MWNT but often referred to as carbon nanofiber to distinguish it from the MWNT that consist of multiple concentric cylinder graphite layers [8, 71, 75, 76]. Because of their unique features such as small size and addressable control, CNT FEAs can be made into FE cathode arrays and potentially applied for multi-beam X-ray sources [77], and parallel EBL [78].

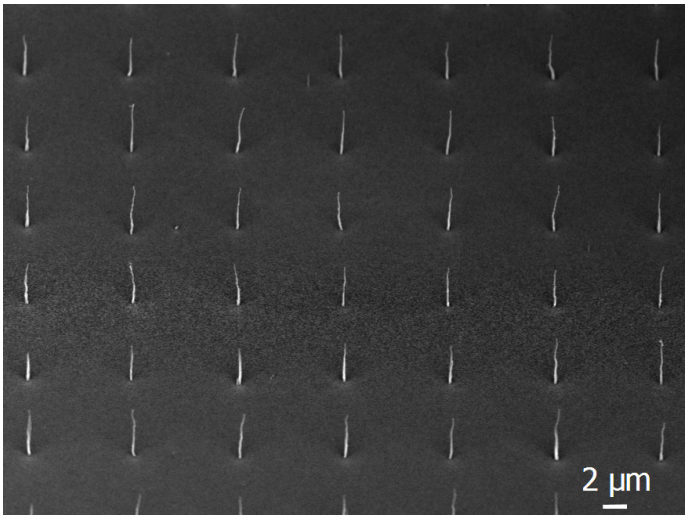

Figure 2.4: An SEM image of a typical free-standing vertically aligned CNT FEA synthesized using PECVD from our group. The image is taken at an tilted angle of 45°.

For both types of cathodes in X-ray sources, triode structures are widely applied: a gate

electrode is placed between the cathode and an anode to control FE from the cathode achieving a high switching rate of electron emission. Usually, a metal grid works as the gate electrode with an insulation spacer separated from the cathode. Integrating a separated gate electrode is easy and convenient, but leading to a large cathode-gate gap and thus a very high control voltage for the FE. For multi-pixel X-ray sources, high control voltage leads to control circuits more complex and makes it harder to allow fast current adjusting of CNT FE cathode. Therefore, a low control voltage is desired to improve the sensitivity of multi-pixel X-ray sources. To achieve it, a well-controlled smaller emitter-gate gap is needed. One advantage of individually vertically aligned CNT FEA is that gate electrode can be integrated with CNT field emitters using nano-fabrication technique to have a well-controlled smaller emitter-gate gap. There are two ways to fabricate such device: growing CNT field emitters in gate holes or placing round holes shape gate electrode around CNT field emitters. The former is a more general way, which can be summarized as follow. After sequentially growing cathode metal layer, insulator layer (separating the cathode and the gate electrode), and gate layer on a silicon substrate. Gate aperture size can be defined by photo lithography or electron beam lithography. Then the gate metal is etched, followed by the insulator layer to spare a room for CNT growth. Catalytic metal is then deposited by electron beam evaporation. Finally, catalyst layer on the gate electrode is removed and CNT field emitters are grown by CVD method.

For the later method to fabricate triode structure, the gate electrode is fabricated on the aligned CNT FEAs. Our group previously proposed a CNT FEA with coaxial cylinder gate cathode, which is able to have well controlled emitter-gate gap within hundreds of nanometers or a few microns and very low gate voltage. Detailed design and fabrication process are shown in Figure 2.5. First, a 20 nm conductive titanium nitride (TiN) thin film is deposited (previously chromium (Cr) is used) on a two-inch wafer substrate to form a bottom electrode and diffusion barrier to avoid the diffusion of catalyst into silicon substrate [71, 79]. (Figure 2.5(a)). Second, catalyst dot array is patterned and deposited on to the bottom electrode (Figure 2.5(b)-(c)). The catalyst sites will be the CNT field emitter sites. In order to achieve high yield (>88%) of single CNT emitters on each site, the lithographic defining dimensions of the catalyst must be 300 nm or smaller. It is reported that catalyst dot dimension of 100 nm giving a 100% yield of single CNT [7, 80]. Besides, after the annealing, the eventual catalyst particle size and the re-

sultant CNT diameter seem to correlate to catalyst film thickness. Thinner films in general lead to smaller particles and tube diameters [70, 81]. In this fabrication process, EBL is employed to pattern the CNT catalyst dots. PMMA A3 is used as an electron beam resist in EBL process. Then a catalyst (Ni) thin film is deposited and lifted off to form patterned catalyst sites (Figure 2.5(d)). Up till this step the sample is ready for CNT synthesis (Figure 2.5(e)). After the vertically aligned CNT field emitter synthesized by PECVD, an insulator layer is conformally deposited to separate the CNT emitter and the gate electrode. This conformal dielectric thin film can be achieved by either PECVD of silicon dioxide (SiO_2) and silicon nitride (SiN_x) or atomic layer deposition of aluminium oxide (Al_2O_3) deposition (Figure 2.5(f)) [67, 82]. Previously, this step was done by PECVD SiO_2 and achieved a thick insulation layer of about 300 μm. Next, the metal gate electrode is conformally deposited to form the coaxial cylinder gate. (Figure 2.5(g)). The uniform insulator layer thickness guarantees that the cylinder gate electrode is self-centred. Next, a supporting layer is deposited preparing for chemical mechanical polishing (CMP) to expose the emitter tip (Figure 2.5(h)-(i)). Then, reactive ion etching (RIE) is used to remove the dielectric layer between the CNT field emitter tip and the gate electrode (Figure 2.5(j)).

Several modifications has been made in the previous fabrication process. First, a TiN thin film layer is used to replace the chromium thin film layer in the previous cathode as bottom electrode and diffusion barrier. Followed the previous fabrication step, we found that after synthesis of CNT process the patterned catalyst Ni dots disappeared and no CNT field emitter was synthesized at the catalyst sites. This situation is due to the diffusion of Ni into the chromium layer. TiN is a hard ceramic material with very good electric conductivity, which is classified as “barrier metal”. Using TiN can solve the diffusion problem of Ni and Cr. Second, magnetron sputtering is used to replace electron beam evaporation to fabricate the coaxial cylinder gate electrode. The electron beam evaporator deposition can achieve good step coverage but not good conformal coverage. As a result, the side of the gate is much thinner than the top when cover the CNT emitters. Besides, CNT is likely to be bent by the thicker deposition layer on the top. Sputter has much better conformal coverage and is able to cover the field emitter more uniformly. Third, PMMA resist is used as the supporting layer for CMP process. In the original design, PECVD SiO_2 or SiN_x is deposited as the supporting layer. After the CMP process, the conformal coverage of the SiO_2 or SiN_x would still cover the metal electrode, making it difficult to bond the gate electrode to the

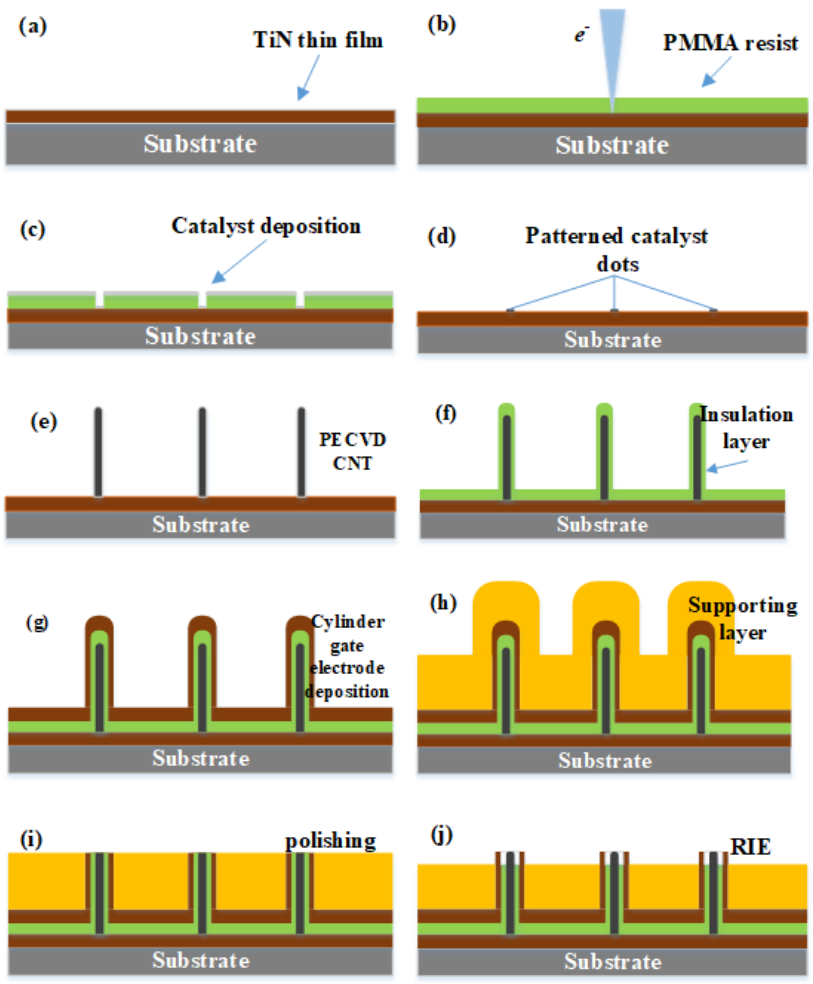

Figure 2.5: Fabrication process of the CNT FEA with coaxial cylinder gate cathode: (a) TiN deposition; (b) catalyst array patterning; (c) catalyst thin film deposition; (d) lift-off of PMMA resist layer; (e) CNT field emitters synthesized by PECVD; (f) insulation layer deposition; (g) cylinder gate electrode deposition; (h) supporting layer coating; (i) exposing the CNT field emitters by CMP; (i) insulation layer removal by RIE.

circuit board. Since a CNT field emitter is about 5 μm in length, micro-scale thick supporting layer deposition is costly. PMMA electron beam resist can be easily spin-coated. After being baked for 20 minutes at 180 °C, the PMMA resist is fully cured and can be used as the supporting

layer for the CMP process. After the CMP process, the PMMA supporting layer can be easily removed by acetone to expose the gate electrode. Therefore, using PMMA as supporting layer is cheaper and more convenient. Figure 2.6 shows the comparison between two CNT FEAs with coaxial cylinder gate electrode fabricated using PMMA and PECVD SiO_2 as supporting layer. It can be seen from figure 2.6 that the gate electrode is fully exposed when suing PMMA as supporting layer. However, the majority part of the metal is covered by SiO_2 when using SiO_2 as supporting layer.

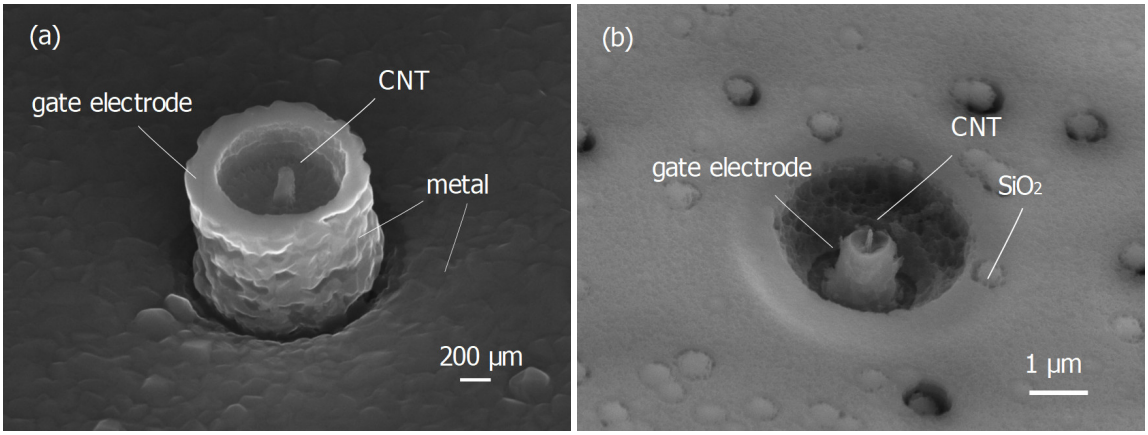

Figure 2.6: Comparison between two CNT FEAs with coaxial cylinder gate electrode fabricated using (a) PMMA and (b) PECVD SiO_2 as supporting layer.

One of the limitations for vertically aligned CNT FEA is the irreversible damage of dominating CNT emitters at high FE current leading to unstable and non-uniform FE performance. In free-standing CNT FEAs, variations in CNT size and morphology result in the variation in the local electric field enhancement among CNT tips [10, 11]. Consequently, a small variation of the emitter size would still lead to a large variation of the emission current contribution from each emitter to the overall emission current, which could cause non-uniform FE and cathode failure. Larger FE current can cause irreversible damage to the dominating CNT field emitters in an FEA and thus unstable and non-uniform FE of the overall FE current. However, the non-uniform FE from CNT FEA and the behaviour and mechanism of vertically aligned CNT field emitter failure induced by FE is still insufficiently studied due to the difficulty of observing and quantifying FE

performance of each emitter in CNT FEAs. Thus, a better understanding of the FE uniformity of CNT FEAs and CNT emitter failure mechanism is of great significance to optimize CNT FE devices for practical applications. CNT field emitter failure in an FEA is often simply attributed to uprooting or burnout of CNT emitters [12–14]. Most investigation reported previously are the failure of SWNTs and MWNTs such as peeling or splitting of the outer shells of MWNTs and removal of cap of SWNTs and MWNTs [11,58,83–85]. These studies are performed using several techniques such as FEM based on fluorescent effect, *in situ* SEM, *in situ* TEM to study structure change after certain FE conditions [11,58,83,86,87]. In contrast to this structure change induced by FE, abrupt failure of the emitter is difficult to capture and observe. Thus, further characterization of the abrupt nanotube destruction and understanding of the mechanism are limited. As such, CNT FEA-based cathodes have not been widely applied in practical applications.

To address these issues, much effort has been devoted to overcoming the non-uniform FE performance and emitter failure of CNT FEA. The presence of ballast resistors in series with field emitters to individually ballast FE from each CNT emitters is a potential solution [12]. In our previous studies, we designed and fabricated ballasted CNT FEA by using large resistor in series with CNT FEA to achieve uniform FE current of CNT FEAs [12,12]. metal-oxide-semiconductor field-effect transistor (MOSFET) as a current limiter is another alternative to protect CNT field emitters from being damaged by large FE current [14,88]. Besides, by exploiting the advantages of carrier velocity saturation in silicon, well designed silicon current limiter in series with field emitters can limit FE current from individual emitter at a desired current level. This approach has been applied to individually ballast silicon FEA but seldom used by CNT FEA due to fabrication complexity [35–38]. Therefore, developing stable, reliable CNT FEA with uniform FE performance and long life-span is a consistent pursuit.

CNT field emitter cathode for X-ray generation

Both CNT thin film field emitter cathode and CNT FEA cathode have been applied as the electron source for X-ray generation. The applications include X-ray radiography, CT, stationary tomosynthesis, miniature X-ray source, and non-destructive testing (NDT). Table 2.1 summarizes several existing CNT field emitter cathodes for X-ray generation.

Table 2.1: A summary of several existing CNT field emitter cathodes for X-ray generation.

Researchers	Emitter type	Synthesis	FE Performance	Applications
H. Sugie et al (2001) [89]	CNTs on a cobalt-coated tungsten wire	No information	1.5 mA	X-ray radiography
O. Zhou et al (2009) [62]	CNT thin film	EPD of pre-produced CNTs	4 $A \cdot cm^{-2}$	Micro-CT, stationary tomosynthesis
P. Sarrazin et al (2004) [90]	MWNT forest	thermal CVD	1 $A \cdot cm^{-2}$	Miniature X-ray tube
J. H. Ryu et al (2013) [91]	CNT array with multiple CNTs on each site	PECVD	1 $mA \cdot cm^{-2}$	CT
H. Y. Choi et al (2010) [92]	MWNT forest	thermal CVD	1.27 $mA \cdot cm^{-2}$	NDT

2.3 CNT FE based X-ray source

FE enabled X-ray generation can be traced back to as early as 1956, when Dyke and Dolan used FE electrons generated from linearly arrayed tungsten pins to strike a copper target to generate X-ray [93]. Then, in 1975, FE X-ray tube was investigated by Charbonnier [94]. The advantages of FE X-ray tubes have been demonstrated in clinical studies by Hallenbeck [95]. In the early days, metal tips were used as field emitters. Unfortunately, the electron emission from these emitters are affected by chemical interact with residual gaseous molecules, resulting in instability of emitted currents in non-UHV ambiences. Therefore, few attempt to use field emitters in non-UHV was of practical significance. FE X-ray tubes using other types of field emitters such as

silicon emitters, diamond emitters were also studied [39, 40, 96]. CNT field emitters, however, can overcome many problems associated with metal emitter tips because they are mechanically and chemically stronger and can withstand higher temperatures.

The idea of applying CNT FE technology to replace thermionic emission counterparts in X-ray sources emerged around 2000. Several patents described the potential of using nanotube transmission cathode for X-ray generation, X-ray generation device using a nanotube FE cathode having an emitted electron current density of at least 4 $A \cdot cm^{-2}$, and large area addressable multi-beam X-ray system using CNT FE source [97–99]. Another early research on CNT as electron source in an X-ray tube was conducted by Okuyama et al in 2001 [89]. The X-ray tube was a chamber with a copper target and dense CNTs (6×10^7 mm^{-2} in site density) in it. They chose a large scale integrated circuit as the first sample to test the FE X-ray tube. The X-ray image recorded with a CNT emitter was as sharp as to disclose every gold wire (30 mm across) for electrical conduction. The exposure time was 14 minutes, because of a low electron current of 1.5 mA. Repeating experiments showed that lifetime of their CNT emitters is 60-80 minutes in 2×10^{-7} Torr. For soft samples plants, they lower the electron energy to 10 keV closed to soft X-ray region to obtain an X-ray image of a leaf.

As an early attempt of developing CNT FE enabled X-ray tube, Okuyamas work provided a comprehensive study on FE X-ray tube configuration, vacuum, CNT emitter lifetime, and both hard and soft samples. In 2002, Otto Zhous group demonstrated a CNT-based X-ray tube which can generate sufficient X-ray flux with a total emission current as high as 30 mA for diagnostic imaging applications [100]. This device structure is still similar to traditional thermionic emission X-ray tube. The cathode is a SWNT thin film deposited on a metal substrate. A relatively low voltage is applied between the gate and the cathode to extract electrons from the cathode. The field emitted electrons are accelerated by a high voltage applied between the anode and the gate. In 2004, Sarrazin et al investigated the potential of CNT field emitters for improving the efficiency and durability of miniature X-ray tubes [90]. MWNT film cathodes were fabricated using a thermal CVD, with diameters varying from 2 mm to 75 μm, achieving current densities of over 1 $A \cdot cm^{-2}$. Research on developing and improving X-ray tube and/or miniature X-ray tube based on CNT FE flourish up till now. For example, Sun fabricated CNT-based field emission X-ray cathode with ballast resistor [12]; Jeong et al fabricated a digital miniature X-ray

tube (6 mm in diameter and 32 mm in length) with a high-density triode CNT field emitter for special X-ray applications [101]. Miniaturized X-ray devices can be created to insert into the body by endoscopy to deliver precise X-ray doses directly at a target area without damaging the surrounding healthy tissues.

As a significant breakthrough in the field of radiology, CT technology enables the reconstruction of three-dimensional (3D) image of an object by collecting a series of two-dimensional (2D) images taken around a single axis of rotation. This technology is now widely used for diagnostic medical imaging and security inspection. Conventional CT system uses a single-beam X-ray source based on thermionic emission that moves across the entire angular range to collect the different projection images. In CT scanning, short time responding or real-time monitoring, slow response and moving X-ray source would lead to limited image quality and accuracy and missing of important information of moving organs such as lung and heart when capturing images. The long response time of the thermionic electron source and motion of the X-ray source, unable to fully eliminate source-motion blur, would result in longer data acquisition time and exposure of a patient in X-ray radiation. Therefore, reduction of motion artifacts of CT scanner requires techniques other than fast scanning [102]. In contrast, because of the intrinsic instantaneous respond of CNT FE and fast switching of X-ray sources based on FE, stationary scanning of CT is achievable using X-ray source arrays instantaneous switching and generating a scanning X-ray beam electronically without any mechanical motion. Around 2005, research on X-ray tube based on based on CNT field emitters started to focus on stationary scanning X-ray source. Early efforts focused on multi-beam X-ray systems [99, 103], then moved to CNT FE based micro-CT [104–106]. Je Hwang Ryu et al from Kyung Hee University also demonstrated a CNT FE X-ray system for CT [91]. The former group used CNT cathodes fabricated by electrophoretic deposition of a composite film of pre-formed CNTs (produced by thermal CVD technique) and inorganic binders on a conducting substrate, followed by heat treatment [107]. The latter group used pattern CNT FEAs produced by PECVD technique [108]. Further researches develop into stationary digital tomosynthesis, a method for performing high-resolution limited-angle tomography. Figure 2.7 illustrates the working mechanism of conventional thermionic emission based tomosynthesis system and stationary tomosynthesis system based on CNT FE cathode.

In 2013, Otto Zhous group at the University of North Carolina demonstrated a stationary

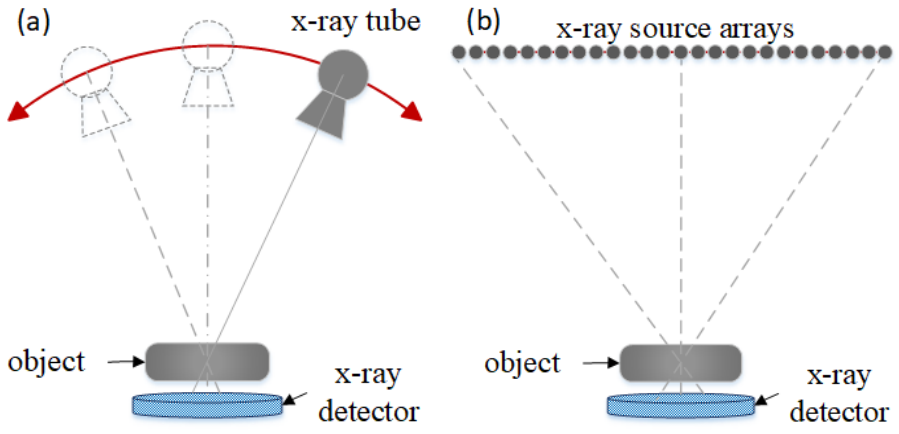

Figure 2.7: The working mechanism of (a) conventional thermionic emission based tomosynthesis system and (b) stationary tomosynthesis system based on CNT FE cathode.

chest tomosynthesis using a CNT FE based X-ray source array and a compact microbeam radiation therapy device using carbon nanotube cathodes to create a linear array of narrow focal line segments on a tungsten anode and a custom collimator assembly to select a slice of the resulting wedge-shaped radiation pattern [109]. In 2014, this group developed a stationary digital breast tomosynthesis (DBT) using CNT FE enabled X-ray tubes to replace the conventional rotatable X-ray source on an existing DBT system [107]. Figure 2.8 illustrates the prototype of the DBT system at the North Carolina Cancer Hospital.

Figure 2.9 shows an example of a reconstructed image of a breast lumpectomy specimen taken by the above-mentioed stationary DBT system [107].

Up till now, research on X-ray generation based on CNT FE continues and develops into various applications such as radiology, CT scanning, and radiotherapy. Currently, challenges for CNT FE based X-ray sources, from the engineering perspective, are to reduce the fabrication cost and achieve uniform, stable, and repeatable FE current. Recent effort in this field is establishing the facility and infrastructure for large quantity production of CNT X-ray sources at market acceptable price. In sum, application of CNT FE for X-ray generation and related fields remains further development but its applications are promising and worthwhile.

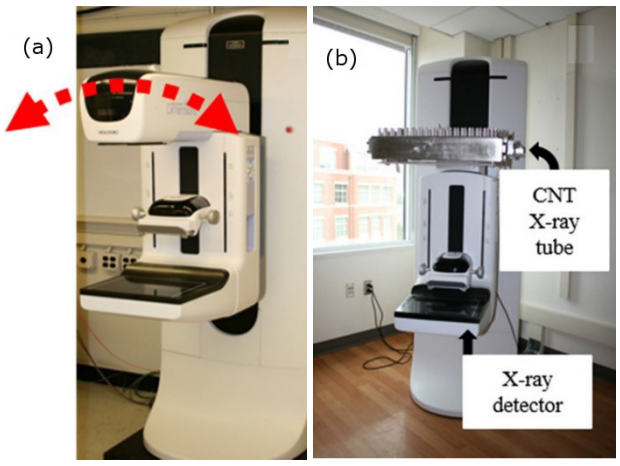

Figure 2.8: The DBT systems using CNT FE based X-ray sources to replace the conventional X-ray tubes: (a) Hologic Selenia Dimensions DBT system adapted to build the stationary DBT; (b) The stationary DBT X-ray tube mounted on the Selenia Dimensions gantry at the North Carolina Cancer Hospital. (Reprinted with permission from IOP publishing via Copyright Clearance Center)

2.4 X-ray fluence field modulation

CT is an advanced medical imaging modality, which produces 3D images for clinical applications, including diagnosis of cancer and guidance of treatment such as image guided radiation therapy (IGRT). By reconstructing a series of 2D images taken around a single axis of rotation, CT is able to eliminate the superimposition of images of structures outside the area of interest distinguish differences between tissues due to the inherent high-contrast resolution, and view 3D images of different medical task. Despite these advancements, a main disadvantage of CT is that it employs ionizing radiation in order to image a patient, which can potentially damage cell and increase cancer risk. The dramatically increased usage of CT over the last two decades worldwide rises a concern regarding the potential risks of radiation dose due to CT scans. Therefore, improving a better performance of CT but maintaining reasonable radiation exposure to limit unnecessary dose to patients is a development tendency of CT. The principle of maintaining radiation exposure“as low as reasonably achievable” is employed in order to limit unnecessary

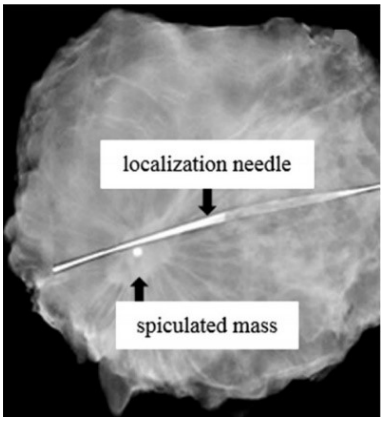

Figure 2.9: A reconstructed X-ray image of a breast lumpectomy specimen acquired with the stationary DBT prototype system. (Reprinted with permission from IOP publishing via Copyright Clearance Center)

dose and cancer risk to patients. One approach for enhanced dose management is to allow the spatial pattern of X-ray fluence field delivered to the patient to change dynamically as the X-ray tube rotates about the patient. The changes in incident fluence could be guided using a patient model and optimization method in order to deliver user-defined image quality criteria while minimizing dose. This type of CT is referred to as FFMCT. Figure 2.10 shows a schematic diagram of methodology for FFMCT

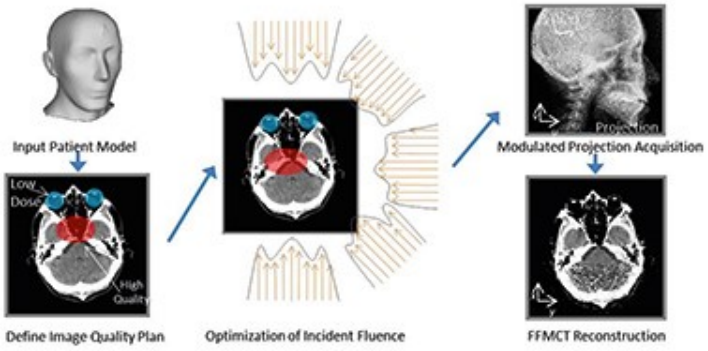

Figure 2.10: The schematic diagram of methodology for FFMCT.

Appropriate use of CT should consider the patients age, size, and the imaging task such as tracking an interventional instrument, surveillance imaging of lung nodules, or diagnosing a suspicious soft tissue lesion in the abdomen. These applications inherently involve balancing the trade-off between image quality and ionizing radiation delivered to the patient. More efficient management of X-ray exposure can aid in alleviating the radiation risks to the patient. As the X-ray beam rotates about the patient, lateral views of the patient inherently attenuate more of the X-ray beam than posterior-anterior views where the path length through the body is shorter. Thus, lower intensity of the X-ray beam is need where the patient thickness is smaller and therefore less attenuating. Application of X-ray fluence field modulation specific to patient anatomy in imaging use moving slits, dynamically varying apertures, and patient specific filters for varying the incident fluence field and exposure time. A typical case is that a bowtie filter is placed in front of the beam to attempt more uniform exposure levels at the detector, by decreasing exposure to thinner regions of the patient [110, 111]. Figure 2.11 illustrates a bowtie filter placed in front of an X-ray beam to allow uniform exposure levels at the detector [112]. Additional collimation of the beam, such as a multi-leaf collimator, has also been used for further reduction of dose to the patient by maintaining higher exposure within a central region of interest [113, 114].

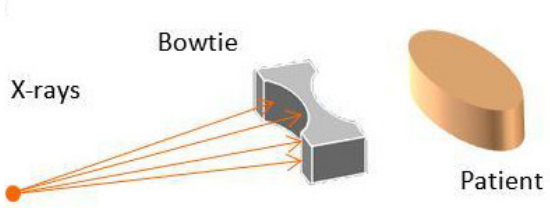

Figure 2.11: Illustration of a bowtie filter decreasing the exposure to thinner region at both lateral ends.

These approaches indicate a new trend of CT development, which is to deliver more patient and task-specific fluence plans with reduction of patient radiation dose. Flexible X-ray fluence is desired to delivery complex changes in attenuation across the field of view from varying projection angles. The idea behind the traditional X-ray fluence field modulation is to use an extra tool to either shape a filter to selectively attenuate a cone X-ray beam or dynamically vary an aperture to adjust exposure time. However, filters and/or collimator that are fixed in the field of

view throughout the CT scan are greatly limited in their ability to compensate for the complex heterogeneity of attenuation presented by real patient anatomy across the incident X-ray field. Besides, filters and collimator are made from high atomic number materials such as tungsten, which make these tool heavy and inflexible. Contrary to the fixed filtration patterns in conventional use, if an X-ray source that allows spatially varying, user-prescribed X-rays but "as low as reasonably achievable" radiation exposure to limit unnecessary dose and cancer risk to patients without sacrificing image quality with limited dose, a heavy and inflexible filter/collimator can be eliminated. Such X-rays can benefit many cases when high image quality near the suspicious lesion is only desired such as locating the tip of a surgical instrument with respect to an anatomical landmark and a repeat diagnostic CT scan to explore a suspicious anomaly. As state above, advantages of FE from CNTs used as electrons source in X-ray system such as fast response, addressable FE sources, and small size have been proved by many studied. X-ray image dose adjustments, fluence field modulation, and shape variation can be achieved by the fast response and addressable CNT FE source. Therefore, there has been an increasing research interest on developing a multi-pixel X-ray source based on CNT FEA cathode to achieve flexible X-ray fluence field modulation by controlling FE performance of the CNT FEA cathode.

2.5 Chapter summary

This chapter presents a comprehensive background review on electron emission theory, CNT field emitter, CNT FE based X-ray sources, and X-ray fluence field modulation based on CNT FE technology. The advantages of FE over conventionally applied thermionic emission is obvious: low working temperature, fast response, and high electron emission efficiency. Increasing interest on CNTs FE applications has been aroused since the FE property was first reported in 1995. Because of the high aspect ratio, good mechanical and chemical properties, and small size, CNT is regarded as an ideal type of material for FE. There are two types of CNT FE cathodes: CNT thin film cathode and free-standing vertically aligned CNT FEA cathode. Both type of CNT FE cathodes have been applied for various of applications such as X-ray radiography, micro-CT, stationary tomosynthesis, miniature X-ray source, and NDT. Free-standing vertically

aligned CNT FEA cathodes are expected to eliminate screen effect and allow more uniform FE current because of their relatively more uniform geometry and well-controlled pattern than CNT film cathodes. With the fast response, addressable FE sources, and small size, X-ray image dose adjustments, fluence field modulation, and shape variation can be achieved by CNT FE base X-ray source to replace the heavy and inflexible filter/collimator in conventional FFMCT.

There is still some challenges remaining in developing stable and reliable CNT FEAs for practical applications. Currently, FE uniformity of CNT FEAs have not been well studied due to the difficulty of observing and quantifying FE performance of each emitter in CNT FEAs. The behaviour and mechanism of vertically aligned CNT field emitter failure induced by FE is also insufficiently studied. Simple and effective approaches to overcome CNT field emitter failure are needed.

Chapter 3

PMMA thin film based FEM

A better understanding of the FE uniformity of CNT FEAs and CNT emitter failure mechanism is of great significance to optimize CNT FE devices for practical applications. Conventionally, phosphor screen is used to help observe FE uniformity of CNT FEAs [115–117]. However, this approach is insensitive to low energy electrons and provides insufficient information of FE performance of each emitter in CNT FEAs. Besides, fine structure is not visible on a phosphor screen because of the lack of homogeneity of the screen [118], which inhibits the observation of small differences in light intensity. For CNT emitters with higher current, the strong illumination would override lower current ones on the phosphor screen, which disturbs the observation of the FE performance of each emitter. Profiling instrument such as cathode emission profiler is reported to characterize FE distribution over the CNT cathode [119,120]. This technique is based on an anode-hole scanning method to obtain emission profile. However, such an instrument is costly. Other techniques such as *in situ* SEM and *in situ* TEM are reported previously, which can study structural change of CNT under FE conditions but is unable to show the uniformity and real-time performance of CNT FEAs [58, 83, 87].

To address these issues, we propose a simple and reliable FEM method using PMMA thin film to observe and quantify the FE performance of each emitter in a CNT FEA. PMMA is an electron sensitive material commonly used as positive EBL resist. As an EBL resist, PMMA thin film is a positive tone resist under low dose electron exposure. The exposed parts can be removed

by methyl isobutyl ketone (MIBK): IPA solution) showing user-defined patterns. In our previous study, we successfully observed the FEM pattern of crystal facets of Zinc oxide (ZnO) using PMMA thin film, which contains the details of the centre structure and the clear "petal" shape boundaries. Such fine details of the FEM patterns are not achievable by the conventional FEM approach using a phosphor screen [121]. Apart from imaging the surface morphology of a single CNT, it can also be applied for investigating FE characteristics of free-standing CNT FEAs if properly designed. In a CNT FEA, various FE current from emitters lead to different degree of electron exposure on PMMA thin film. Utilizing these features, we are able to observe the FE current from each CNT emitter as different morphology of FEM patterns on the PMMA thin film. In this way, the overall FE uniformity of the CNT FEA and FE current contribution from each emitter can be visualized and quantified. Any CNT emitter can be located corresponding to its own FEM pattern. In contrast to the conventional FEM using a conducting fluorescent screen anode [122], PMMA thin film is highly sensitive to low energy electron beam such as low turn on voltage FE from free-standing CNT FEA in this case. In addition, the illumination of fluorescent screen shows the overall FE uniformity of a CNT FEA at a certain moment during a FE process, which varies as time goes. While the FEM pattern on the PMMA thin film show the FE performance of integrated dose, which is more accurate. Real-time FE performance from free-standing CNT FEAs can be observed and recorded by using a microscopic camera for further analysis.

3.1 Experiment design

3.1.1 FEM experiment set-ups

The FE experiment is simple but using a piece of Indium tin oxide (ITO) coated glass covered by a PMMA 950K A3 thin film layer (120 nm) as anode. The FE experiment set-up consists of an anode, a free-standing CNT FEA as the cathode, and a Kapton polyimide film as spacer in-between the anode and the cathode. A pico-ammeter is used to apply a voltage bias for FE and measure the corresponding FE current from the free-standing CNT FEAs. The set-up is sealed in a vacuum chamber with a base pressure of 2×10^{-8} Torr. A video camera with a microscopic

lens and a light source is fixed outside the vacuum chamber focusing on the PMMA thin film surface to magnify and record its change during the FE process. Figure 3.1 shows the schematic of the experiment set-up. After a FE test, the PMMA thin film on the anode surface is developed in MIBK: IPA developer (MIBK: IPA= 1:3) to reveal the FEM patterns left by the FE exposure from the CNT FEA. Optical microscopy images of the PMMA thin film after development are taken to visualize the FE performance from each emitter. Video records of the real-time FE is processed for further analysis.

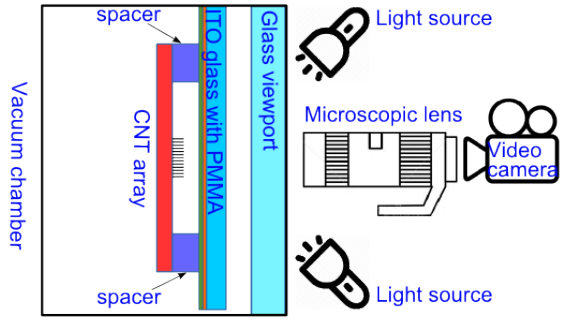

Figure 3.1: The schematic of the FEM experiment set-up.

3.1.2 Free-standing vertically aligned CNT FEAs design and synthesis

The primary goal of this method is to characterize FE uniformity of CNT FEAs that is used for practical applications. In our prior study, we characterized a CNT FEA, which is designed as an electron source for X-ray generation. The CNT FEA contains 8260 CNTs in a regular octagon area with a diagonal of 1 mm and an inter-emitter distance of 10 μm using the proposed method [29]. The overall uniformity of the CNT FEA is successfully visualized. The FE current dominating emission sites are revealed using acetone wash, since high electron dose left negative tone pattern of PMMA thin film. However, due to the large number of CNT field emitters and small inter-emitter distance, it is hard to locate an emitter from so many emitters. Besides, since the FEM patterns on the PMMA thin film is about 100 to 150 μm in diameter, FEM patterns

of neighbour emitters are overlapped. In order to demonstrate the proposed method, properly design CNT FEAs should be fabricated in consideration of two aspects: inter-emitter distance must be large enough to avoid FEM patterns overlap, the number of CNT emitter in an FEA should be large enough to show the generality but small enough for the ease of later analysis. Therefore, two different densities of free-standing CNT FEAs are designed and fabricated for the FE uniformity study: an 11×11 free-standing CNT FEA with an inter-emitter distance of 100 μm in a square area of 1 mm^2 and a 20×20 free-standing CNT FEA with an inter-emitter distance of 50 μm within a square area of 1 mm^2. The inter-emitter distances of the investigated free-standing CNT FEAs are large enough to guarantee that FE from each CNT emitter in the free-standing CNT FEAs is independent [68, 71].

The free-standing CNT FEAs of the different densities are synthesized by PECVD within an area of 1 mm^2 on highly doped silicon substrates. First, a TiN layer (70 nm) is deposited on the highly doped silicon substrate as diffusion barrier to avoid catalyst (Ni) diffusing into the silicon substrate during CNT synthesis. Then EBL is used to pattern the Ni dot FEAs of desired densities with a diameter of 100 nm and a thickness of 30 nm for one CNT field emitter grown on each site. Next, the substrate is put into PECVD system to be heated to 700 °C and then exposed to acetylene (C_2H_2, 50 sccm) and ammonia (NH_3, 200 sccm) gases in direct current (DC) plasma at a pressure of 5.5 mbar for 10 minutes to synthesize free-standing CNT FEAs on the patterned catalyst dots. CNTs synthesized by PECVD using Ni as catalyst is typically tip-growth, where Ni particles remain on the top of the CNT throughout the synthesis. The electrostatic force creates a uniform tensile stress on the Ni particles to grow CNTs vertically aligned [28]. Ideally, this recipe will synthesize CNT emitters that have a base diameter about 100 nm and a height of about 5 μm [7]. However, due to some randomness during the fabrication such as variation of diffusion barrier quality and catalyst conditions, the size of the synthesized CNT emitters varies.

In both cases, the CNT field emitters and corresponding FEM patterns are numbered, starting from the very lower left corner of the CNT FEAs. Since the PMMA thin film faces to the CNT FEA, the number on the FEM pattern starts from the lower right corner. Thus, we can locate any CNT emitter within the CNT FEA that corresponds to its FEM pattern. SEM study can be performed on the interested CNT field emitters. Therefore, the relationship between CNT morphology and corresponding FE performance can be built.

3.2 FE uniformity characterization

3.2.1 FE uniformity of an 11×11 free-standing CNT FEA

Figure 3.2 shows the FE performance of the 11×11 free-standing CNT FEA cathode with an inter-emitter distance of 100 μm in a square of 1 mm^2, the insert is the F-N plot. An overall FE current of 4.2 μA is achieved under an applied voltage of 500 V. The anode-cathode gap is 50 μm. The FE test is conducted using a sweep voltage from 0 to 500 V with a step voltage of 5 V and a step interval of 0.5 s for 50 times.

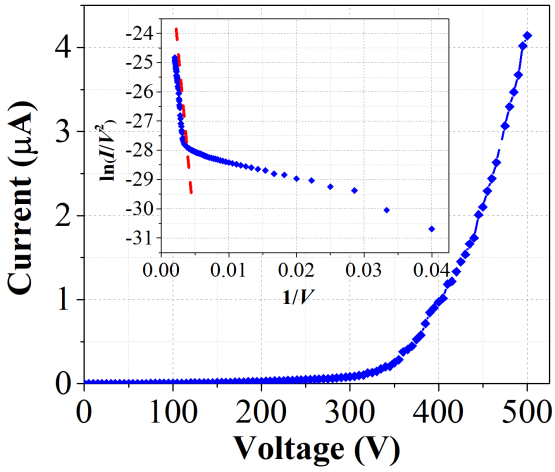

Figure 3.2: FE performance of the 11×11 free-standing CNT FEA and the F-N plot (the insert).

Some of the FEM pattern on the PMMA thin film is visible before being developed. However, the development process improves the contrast of the FE exposed sites on the PMMA thin film. Figure 3.3 shows the optical microscope images of FEM patterns left by the FE of each emitter of the 11×11 free-standing CNT FEA on the PMMA thin film after development. The overall FE uniformity can be visualized. Different FEM pattern sizes reflect different levels of FE current contribution from different CNT emitters. The larger the FE current from each emitter, the more exposure to the PMMA film, and thus the larger and stronger the corresponding circular FEM

mark on the PMMA film. We classify the FE current contribution of each emitter into five levels based on the morphology of the FEM pattern: negligible (nothing), light (only a dot), medium (a dot with circumferential "shade"), strong (a dot with a "flower-like" circle and circumferential "shade"), and very strong (very large circle with "burnt" central). In this way, the overall FE performance of each emitter of the 11×11 free-standing CNT FEA is recorded and the FE current contribution from each emitter is visualized.

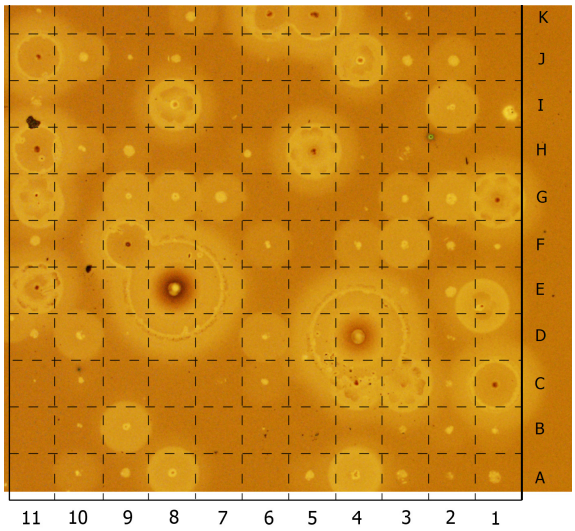

Figure 3.3: The optical microscope image of FEM patterns left by FE of the 11×11 free-standing CNT FEA on the PMMA thin film. Each square unit has a side length of 100 μm.

Figure 3.4 shows the number of CNT emitters of each FE current contribution level. In this case, 77 CNT field emitters participate in the FE, where two emitters make a very strong FE contribution to the overall FE current from this CNT FEA. Since 44 CNT field emitters did not participate in the FE under 500 V, higher current density of the CNT FEA can be expected if they are activated under higher voltage. However, the two CNT emitters that make a very strong FE contribution is more likely to be damaged under higher voltage.

Figure 3.5 shows the SEM images of typical CNT emitters from site F-5, E-3, F-6, C-1, and E-8, which make negligible, light, medium, strong, and very strong FE current contribution, respectively. The image is taken at a tilted angle of 45°. According to the SEM images, the

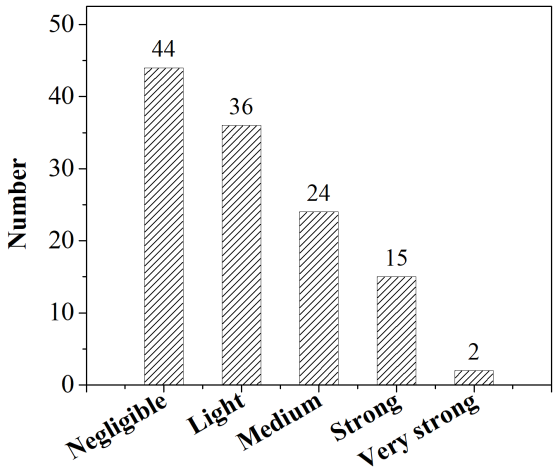

Figure 3.4: FE contribution levels and statistics of the 11×11 free-standing CNT FEA.

height of these CNT emitters are 1.8 μm, 1.9 μm, 2.4 μm, 2.3 μm, and 3.1 μm. The diameter of the emitter tips are 65-70 nm, 50-55 nm, 40-45 nm, 30-35 nm, and 30-35 nm. As is known to all, under the same applied voltage, higher and thinner emitters is tend to have higher FE current. The proposed method is capable of reflecting the different FE current contributions of emitters in a CNT FEA due to the deviation of the emitter height and tip diameter, as well as some other factors.

3.2.2 FE uniformity of a 20×20 free-standing CNT FEA

Figure 3.6 shows the FE characteristics and the F-N plot of the 20×20 free-standing CNT FEA with an inter-emitter distance of 50 μm in a square of 1 mm^2. The sweep voltage repeats 24 times in this case. An overall FE current of 13.7 μA is achieved under an applied voltage of 500 V. The anode-cathode gap is 50 μm.

Figure 3.7 shows the optical microscope image of the FEM patterns of the 20×20 free-standing CNT FEA. Under the same definition, we are able to directly visualize the different current contribution of each emitter to the overall FE current according to the different FEM

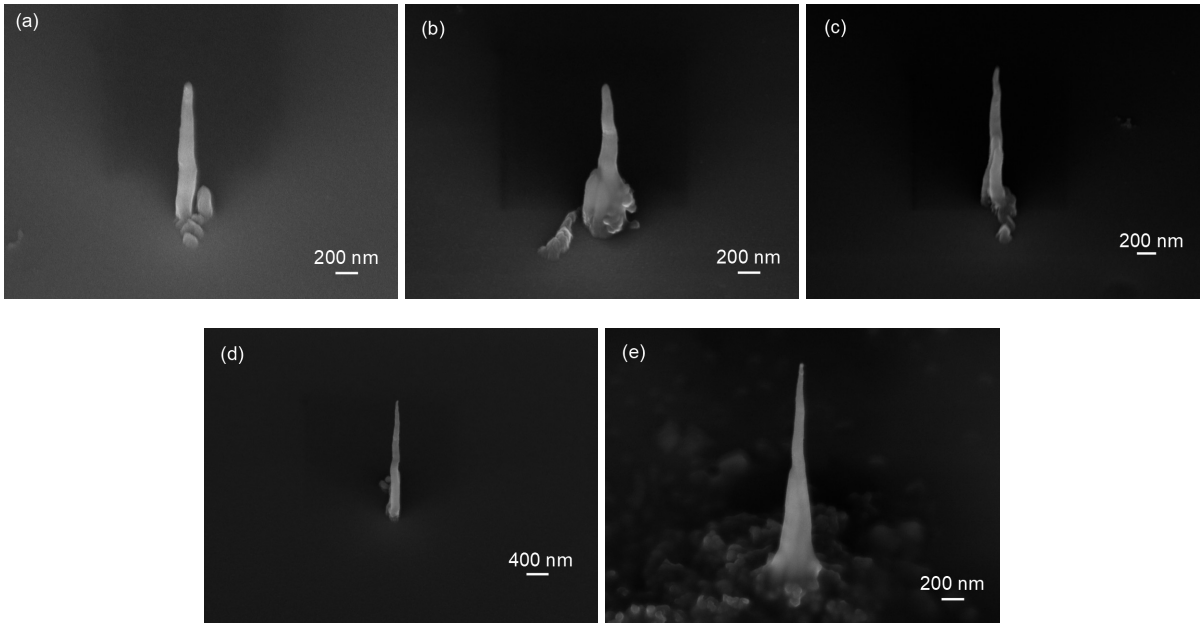

Figure 3.5: SEM images of typical CNT emitters from site (a) F-5, (b) E-3, (c) F-6, (d) C-1, and (e) E-8, which make negligible, light, medium, strong, and very strong FE current contribution, respectively. The image is taken at a tilted angle of 45°.

pattern on the PMMA thin film.

Figure 3.8 shows the detailed statistics. Similar to the previous case, seven of the total CNT field emitters make a "very strong" contribution, while 218 of the CNT field emitter are not activated under 500 V, which is more than half. Similarly, in the activated CNTs, the percentage of FE current levels from "very strong" to "negligible" shows a pyramid distribution from top to bottom.

Figure 3.9 shows the SEM images of CNT emitters from site A-1, B-9, J-1, and E-8, respectively. The image is taken at a tilted angle of 45°. According to the SEM images, the height of these CNT emitters are 6.7 μm, 7.2 μm, 7.5 μm, and 6.3 μm. The diameter of the CNT emitter tips are 15-20 nm, 30-35 nm, 30-35 nm, and 15-20 nm, respectively. In this case, CNT emitters with height larger than 7 μm show stronger exposures on the PMMA thin film.

Although same catalyst size and thickness is used for the 11×11 free-standing CNT FEA and

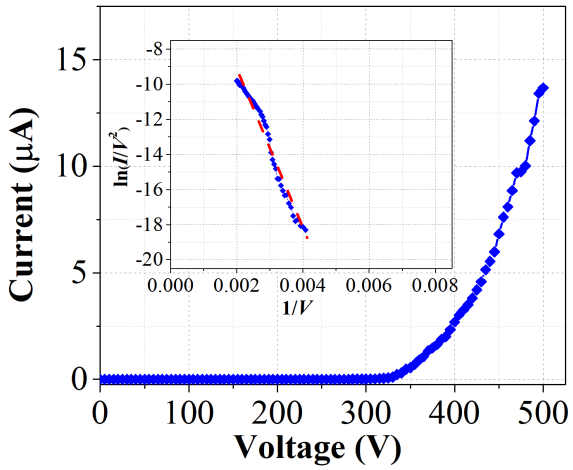

Figure 3.6: FE performance of the 20×20 free-standing CNT FEA and the F-N plot (the insert).

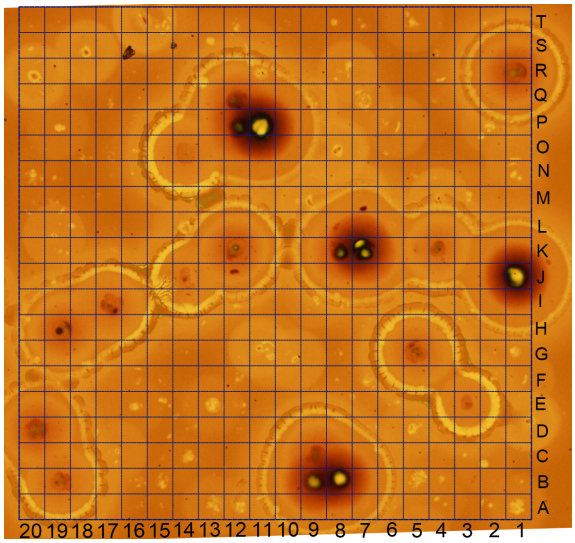

Figure 3.7: The optical microscope image of the FEM patterns of the 20×20 free-standing CNT FEA on the PMMA thin film. Each square unit has a side length of 50 μm.

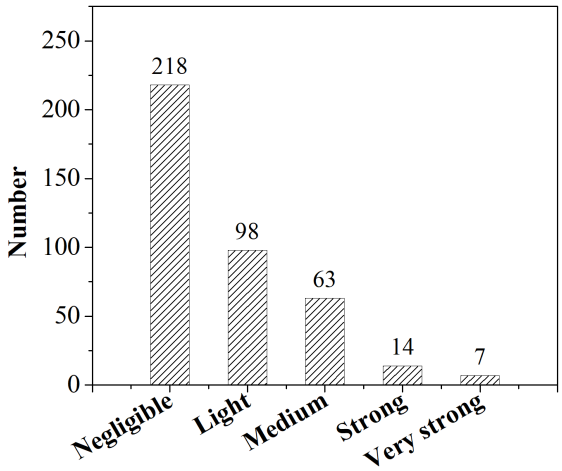

Figure 3.8: FE contribution levels and statistics of the 20×20 free-standing CNT FEA.

the 20×20 free-standing CNT FEA, the CNT emitters in the former FEA is shorter and thicker than those in the latter FEA, It looks that 30 nm thick Ni dots is not enough for the former but too much for the later. One possibility causing the difference is the different quality of the diffusion barrier in-between the silicon substrate and the catalyst dots for CNT emitter synthesis. The diffusion barrier here used is TiN deposited by reactive sputter. Since TiN forms with an extended range of composition (TiN_x with $0.6 < x < 1.5$) and significant vacancy concentration, the mechanic properties of TiN varies with different x formed during the reactive sputter [123]. A better diffusion barrier quality is able to help form larger contact angle of catalyst droplets during CNT synthesis. Thus, CNT synthesized on a better diffusion barrier tend to grow taller and thinner, but multiple CNTs on thicker catalyst. Another possibility is the difference in the total left Ni amount deposited on samples. The CNT may grow from the re-deposited Ni during PECVD process. As can be seen from Figure 3.9, there are detectable Ni particles on top of the CNTs, even on the top of the branches, so CNT emitters in the 20×20 CNT FEA grow taller than those in the 11×11 CNT FEA. Detailed reasons that affect CNT morphology need further exploration. Nevertheless, the proposed method is capable of exhibiting the overall FE uniformity of CNT FEA and the variation of FE current contribution of CNT emitter, which can

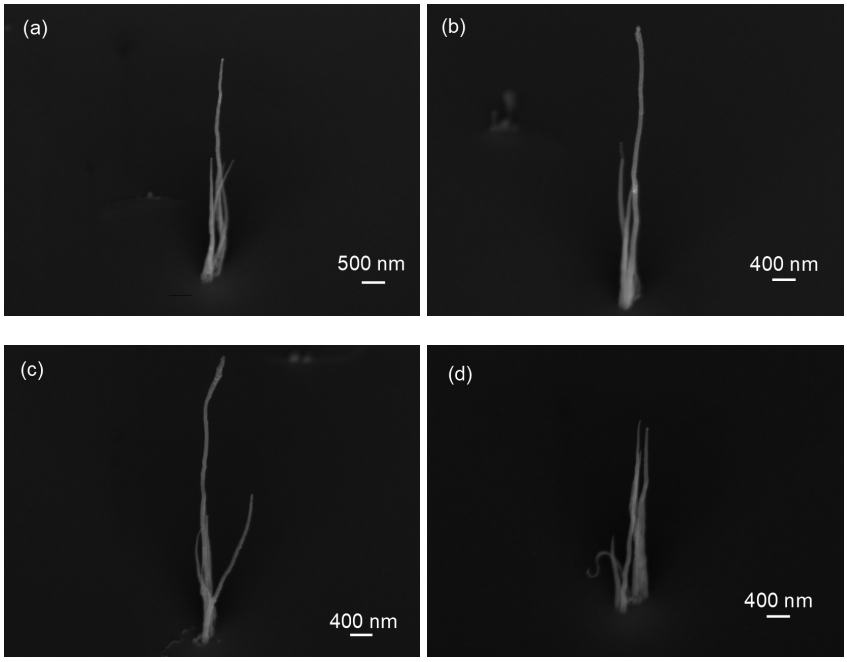

Figure 3.9: SEM images of CNT emitters from site (a) A-1, (b) B-9, (c) J-1, and (d) E-8, respectively. The image is taken at a tilted angle of 45°.

facilitate the optimization of CNT FEAs.

3.3 FEM study of CNT emitters

Since the anode-cathode gap is only 50 μm, the FEM magnification is not comparable as conventional FEM using phosphor screen with a millimetre scale tip-anode distance [124, 125]. However, this shortage can be overcome by enlarge the anode-cathode gap and using a high magnification microscope. Figure 3.10(a) shows a typical FEM pattern of the CNT at site I-8 of the 11×11 free-standing CNT FEA, a flower-like FEM pattern with six "petals". The six lightly exposed areas have clear outlines and surround the centre major exposure area. According to this FEM pattern, we believe that the six lightly exposed regions indicate electrons emitted from a hexagon edge of the CNT tip. Figure 3.10(b) show the scanning helium ion microscopy (HIM)

image of the corresponding CNT field emitter taken at a tilted angle of 45°. Compared with SEM, HIM has a superior depth of field, which is able to show both CNT tip and base clearly.

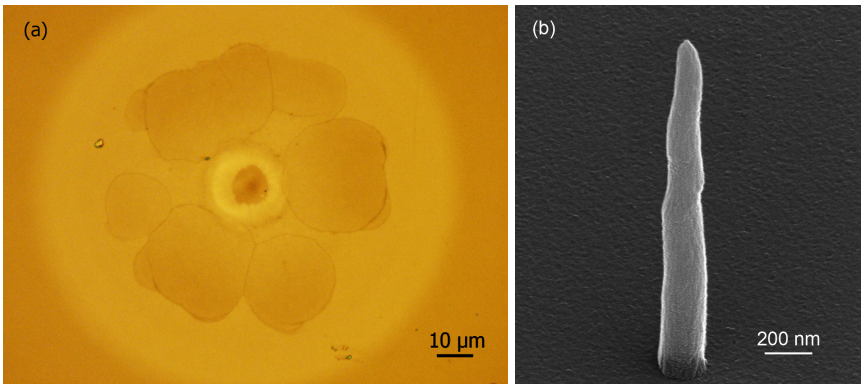

Figure 3.10: The FEM pattern and the corresponding CNT at site I-8 of the 11×11 free-standing CNT FEA. (a) Optical microscope image of the FEM pattern showing six lightly exposed regions have clear outlines and surround the centre major exposure area. (b) The HIM image of the CNT field emitter at site I-8 taken at an tilted angle of 45°.

From the Figure 3.10(b), the CNT has a height of about 2.1 μm and a base diameter of about 150 nm. There is a protruding point at the tip of the CNT emitter with a diameter of about 30 nm, which has the most significant field enhancement geometry. We believe the centre exposed area in the FEM pattern reflects the major electron emission from the protruding point at the very end of the tip. From the tip to the trunk of the CNT emitter, there is a clear bend angle at the tip-trunk junction, at which the diameter is about 80 nm. The bend angle is considered as another field enhancement geometry on the CNT emitter. We believe the six surrounding lightly exposed areas reflects the minor electron emission from the bend angle at the tip-trunk junction. The relationship between the PECVD CNT tip morphology and electron tunnelling needs further study. Nonetheless, the proposed approach is able to produce real space magnified images of a CNT tip showing its morphology under a proper FE exposure. Compared with FEM of CNTs using a phosphor screen, our PMMA thin film based FEM approach has a higher resolution. Fine outlines of different expose region within the FEM pattern is recognizable.

In the 20×20 free-standing CNT FEA, some FEM patterns show more than one exposed

dots in the centre, which are supposed to be one since one site should have one CNT emitter. For example, at site O-8, there are two exposed dots found in the centre of the FEM pattern (Figure 3.11(a)). We are doubting that two CNT emitters are grown at that site according to the FEM pattern. At site G-11, there are some unexpected imprints appearing next to the central exposed dot (Figure 3.11(b)). To figure it out, we locate these CNT emitters and check the CNT morphologies after the FE test using SEM.

Figure 3.11(c) and (d) show the SEM images of the CNT emitters at site O-8 and site G-11 after the FE test, respectively. It can be seen that multiple CNTs are synthesised at each site. At site O-8, two thin and tall CNTs are in the middle and two thick CNTs are on the side. According to the FEM pattern at site O-8, the two central dark dots reflect the FE from the middle two thin CNTs and two light dots on the side reflect the two thick CNTs as shown in the SEM image. At site G-11, multiple CNTs twine as a CNT bundle. From the FEM pattern, two dark spots on the top are formed by the upper CNT tips and the two dark spots with some unexpected imprints at the bottom are formed by the multiple CNT tips on the other side. We also check the other CNTs in the FEAs with similar FEM patterns and found that at multiple CNTs are grown at the corresponding sites. Multiple CNTs grown at one emission site usually occurs when there is formation of multiple catalyst droplets at one site during ammonia plasma pre-etching and heating up to 600-700 °C. Catalyst droplets formation for CNT growth is dependent on several parameters including the choice of buffer layer, the substrate, and the type and thickness of the catalyst used [75]. However, PMMA thin film FEM approach is proven that the relationship between CNT morphology and corresponding FE performance can be built. This approach will greatly facilitate the study of CNT FE mechanism and factors that result in FE non-uniformity and emitter failure.

3.4 CNT field emitter failure characterization

Using PMMA thin film based FEM approach, we are able to observe the FE uniformity and the FE current contribution from each CNT emitter to the overall FE current of a CNT FEA. However, the FEM patterns cannot record the time evolution CNT performance during a FE

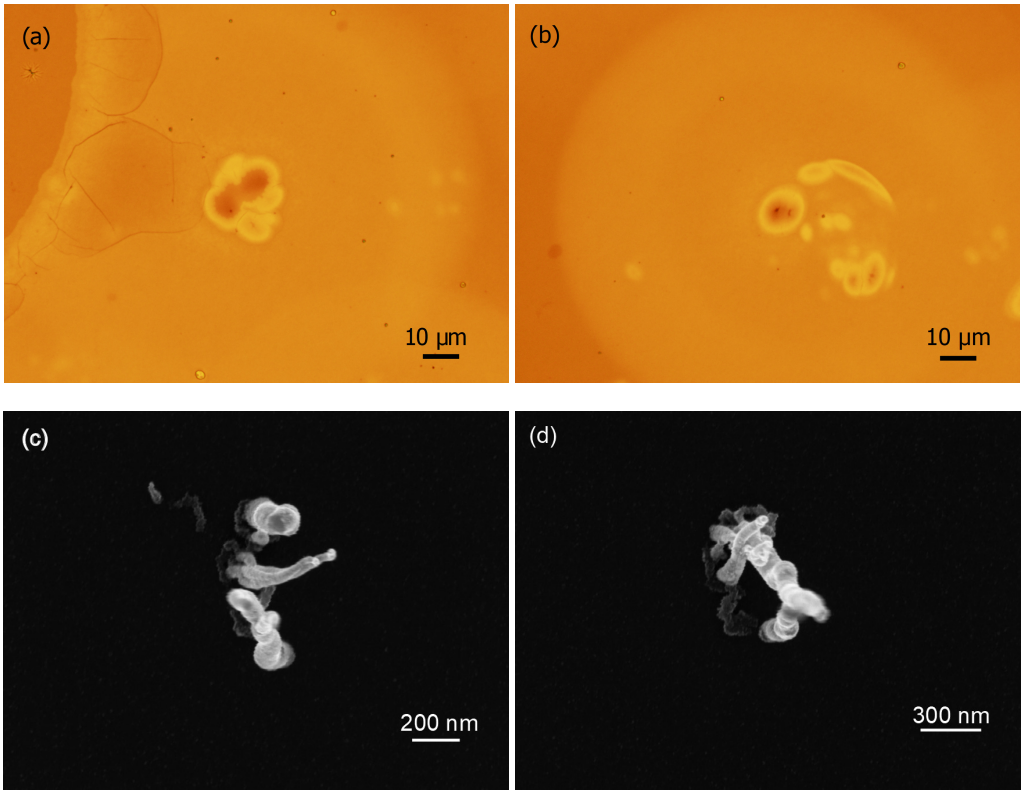

Figure 3.11: Optical microscope images of FEM patterns at (a) site O-8 and (b) site G-11; Top view SEM images of CNT field emitters at (c) site O-8, and (d) site G-11. Central exposed dots of the FEM patterns clearly reflect the corresponding CNT field emitters' morphology.

process. Especially, when a CNT emitter is working at a high current level, which can potentially cause the CNT emitter failure, only FEM patterns on the PMMA thin film cannot indicate at what time the CNT emitter breaks down and how it looks like at that moment. In the above studies, we found that there are clear patterns of electron exposure on a PMMA thin film before development. Besides, PMMA thin film is optical transparent. Benefiting from these features, we are able to use a video camera and a microscope lens to observe and record real-time FE performance from free-standing CNT FEAs for further analysis.

To demonstrate CNT emitter failure study using the propose method, FE performance from

another 11×11 free-standing CNT FEA is studied based on the PMMA thin film FEM approach with a video camera to monitor and record its real-time FE performance. Here, a thinner cathode-anode spacer (25 μm) is used to make the CNT FEA working at a high current level under a constant voltage of 450 V for 19 minutes. Figure 3.12 shows the FE current of the CNT FEAs under a constant voltage of 450 V. An average FE current of 32.7 μA is achieved, which is almost ten times of current as achieved by the 11×11 free-standing CNT FEA in the previous section. In this free-standing CNT FEA, dominating CNT field emitters are very likely to be damaged at such high current level.

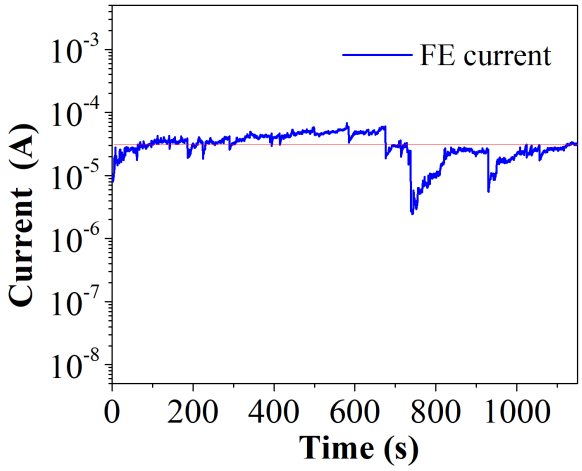

Figure 3.12: The FE current of the 11×11 free-standing CNT FEA under a constant voltage of 450 V.

It can be seen from the Figure 3.12 that the overall FE current shows a tendency to increase though current drops occur sometimes. The current level fluctuates drastically during the mid-stage of the experiment but recovers and basically maintains around 30 μA in the later stage. Moderate Joule heating can cause a rise in the overall FE current on the account of temperature dependence of FE [126, 127]. In this study, we believe the tendency of current increase at the early stage and the tendency of current recovery after current drops are due to temperature rise of CNT emitters induced by Joule heating.

Figure 3.13 show the FEM patterns of the 11×11 free-standing CNT FEA on the PMMA thin film after the FE test. We mirror the image such that the FEM patterns in this figure is the same view as the video. The number of the pattern starts from the lower left corner to match the CNT FEA.

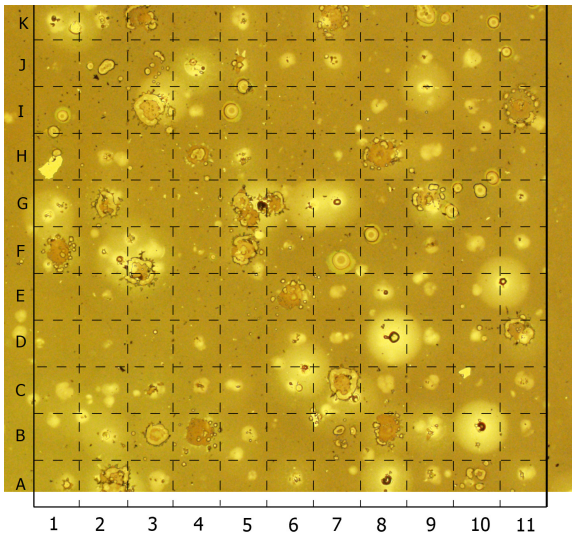

Figure 3.13: The optical microscope image of the FEM patterns of the 11×11 free-standing CNT FEA on the PMMA thin film.

In Figure 3.13, apart from the FEM patterns which is defined above, there are many "firework-like" pattern. Such patterns formed after a light emission of CNT field emitters had been spotted at the corresponding sites during the real-time FE process. Take site H-8 as an example. Figure 3.14 illustrates real-time FE performance of CNT field emitter at the site H-8 in chronological sequence, captured from the video record.

During the FE process, we spotted the site H-8 from almost nothing (Figure 3.14(a)) to light emission (Figure 3.14(b)), and finally to "firework-like" pattern. (Figure 3.14(c)). The "firework-like" pattern after the light emission is caused by an explosion, based on the direct visual observation. In the meantime, we found a current drop on the FE current, which is one of the reasons that lead to fluctuation of the overall FE current and unreliability of FE devices. We suspect a CNT field emitter "burn-out" happened. To verify our suspect, we located CNT field emitter at

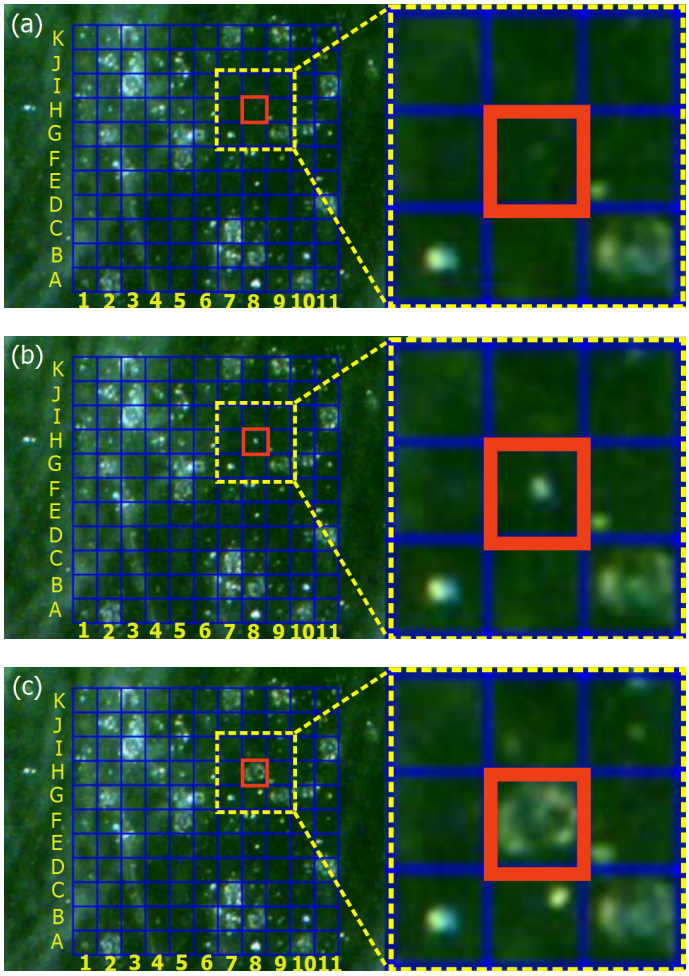

Figure 3.14: Video screen-shots showing the real-time FE performance at the site H-8 in chronological sequence: (a) a weak exposed dot, (b) a light emission, (c) an explosion after the light emission leaving a "firework-like" pattern.

site H-8 using SEM, shown in Figure 15 (a). At site H-8, where a CNT field emitter supposed to be, there is no CNT emitters but a burnt substrate. On the contrary, at site B-10, FEM pattern indicates a FE current contribution from the corresponding CNT field emitter. There is an intact CNT field emitter found in SEM after the FE test at site B-10. We believe the CNT field emitter failure is due to high FE current from the CNT causing Joule heating of the CNT. The

Table 3.1: FE statistics of the 11×11 free-standing CNT FEA at high FE current level.

	FE levels		
	Negligible FE	Normal FE	Burnt-out
Number	15	78	28
Percentage	12%	65%	23%

high temperature burns the CNT and the emission site. Joule heating is a common phenomenon in FE [84, 127, 128]. The FE current increases the temperature of the CNT emitter significantly causing light emission. Besides, the heat also contribute a part of electron emission [126]. We believe the overall FE current of this FEA shows a trend of increase is due to the Joule heating, shown in Figure 3.12.

Similar results can be found at other sites such as site E-6 and site D-8. At site E-6, a light emission is found followed by an explosion during the FE and a "firework-like" pattern left on the PMMA thin film, and a "burnt-out" CNT found in SEM images after the FE test. Whereas, at site D-8, a current contribution from the CNT emitter is visualized on the PMMA thin film and an intact CNT emitter is found in SEM after the FE test. In this CNT FEA, as many as 28 CNTs are burnt-out according to the FEM pattern on the PMMA thin film. The CNT emitters failure can be visualized and recorded by a video camera with a microscopic lens during the FE. More importantly, light emission followed by explosion of CNTs during a high current level is spotted by the proposed method, which is impossible to be detected by using a phosphor screen due to illumination of the anode occurring. Table 3.1 summarizes the number and percentage of different FE level from each emitter in this 11×11 free-standing CNT FEA. In this case, 106 emitters are activated where 28 emitters are burnt-out. The negligible, normal, and burnt-out FE current contribution show an approximate normal distribution.

In addition, video record shows that CNT emitters in a CNT FEA are neither activated nor failed at the same time. For example, the CNT emitter at site A-2 emits light and explodes at

a very early stage, while the CNT emitter at site B-4 is the last one in the video that shows light emission and explosion. Moreover, from Figure 3.14(a) and (b), there are six CNT emitter "burnt-out" during the period in chronological order. These phenomenon is due to the deviation of the current from different CNT emitters causing the variation of the time that heat finally damages corresponding CNT emitter. This find is able to explain that, in CNT FEAs, different time of CNT field emitter failure can also cause the fluctuation of the overall FE current and unreliability of the FE device. Therefore, the proposed method will facilities the improvement of CNT FE device stability and reliability in practical applications.

In sum, utilizing the high sensitivity and high resolution capability of PMMA thin film to the electrons, the proposed method is successfully applied to visualize the FE uniformity of free-standing vertically aligned CNT FEAs, build the relationship between the CNT emitter morphology and its FEM pattern, and detect CNT emitter failure in CNT FEAs. The FE performance of each CNT emitter in a CNT FEA is related to the CNT size, morphology, composition, which can be revealed by the size and shape of the FEM pattern on the PMMA thin film exposed by the electron emission. The overall FE uniformity of CNT FEAs with any density can be visually observed by the distribution of the centre exposed areas of the FEM. Emitter failure due to Joule heating and explosion of the emitters can be distinguished by the "firework-like" FEM pattern in comparison with normal FE.

3.5 Chapter summary

The proposed FEM method based on PMMA thin film is novel and effective to study the FE uniformity and CNT emitter failure of free-standing CNT FEAs. The method is demonstrated by studying the FE uniformity of 11×11 and 20×20 free-standing CNT FEA under a low control voltage. The FE current contributions from each emitter and the overall FE uniformity are recorded and visualized on the PMMA thin film. The distinguishable size and shape of the FEM patterns on the PMMA thin film indicate five levels of the FE current contribution from each emitter. By locating the CNT emitters and the corresponding FEM patterns, the proposed approach allows us learn the details of the CNT emitter morphology from the FEM pattern. Mul-

tiple CNT emitters at an emission site can also be reflected by the FEM pattern on the PMMA thin film. Besides, observation and record of real-time FE performance and CNT emitter failure process are successfully achieved in an 11×11 free-standing CNT FEA using microscopic camera. The "firework-like" FEM patterns distinguish CNT emitter failure, exhibiting a light emission followed by an explosion that cannot be observed by conventional phosphor screen. The results show that CNT emitters in a CNT FEA do not break down at the same time, which is one of the cause of the fluctuation of the overall FE current and the unreliability of the FE device. The emission sites of the damaged CNT emitter are melted by Joule heating at high FE current after a violent light emission. In sum, the proposed FEM method is capable of resolving the major challenge of building the relationship between FE performance and CNT morphology, which significantly facilitates the study of FE non-uniformity and emitter failure mechanism by overcoming the difficulty of observing and evaluating the FE of each emitter in CNT FEAs. This method can also be applied to study FE characteristics of Spindt-type FEA, silicon FEA, and other type of FEA to help develop stability and reliability of FE devices in practical applications.

Chapter 4

CNT field emitter failure behaviour and mechanism

One of the limitations for CNT FE is the irreversible damage of dominating CNT emitters at high FE current leading to unstable and non-uniform FE performance. However, the behaviour and mechanism of vertically aligned CNT field emitter failure induced by FE is still insufficiently studied, which is often simply attributed to uprooting or burnout of CNT emitters [12–14]. Most investigation reported previously are the failure of SWNTs and MWNTs such as peeling or splitting of the outer shells of MWNTs and removal of cap of SWNTs and MWNTs [11, 58, 83–85]. These studies are performed using techniques such as FEM based on fluorescent effect, *in situ* SEM, *in situ* TEM to study structure change after certain FE conditions [11, 58, 83, 86, 87]. In contrast to this structure change induced by FE, abrupt failure of the emitter is difficult to capture and observe. Thus, further characterization of the abrupt CNT destruction and understanding of the mechanism are limited.

These issues can be resolved by the FEM method based on PMMA thin film with a microscopic camera [129]. The high sensitivity to low energy electrons of PMMA thin film is able to record the FE performance of each CNT emitter from a CNT FEA. The transparency of PMMA thin film allows direct observation of the process and history of CNT emitter failure induced by FE. Using this method, we are able to observe CNT emitter failure process, which exhibits a light

emission followed by an explosion [129]. Explosions found in various types of charged clusters exploding into smaller fragments are called Coulomb explosion [130–135]. Apart from some Coulomb explosions induced by chemical reaction [135], X-ray [136], and electron beam irradiation [133], most Coulomb explosions reported are induced by laser pulse excitation [130–132]. However, the mechanism behind this phenomenon of CNT field emitter demands further characterization and understanding.

4.1 CNT field emitter failure experiment

The designed free-standing vertically aligned CNT FEA has 11×11 CNT field emitters with an inter-emitter distance of 100 μm in a square area of 1 mm^2. The CNT emitters has an average height of 5.12 μm and a standard deviation of 0.55 μm, corresponding to 10.7% of the average. This data is in good agreement with that reported in the previous study (6.3%) [7].

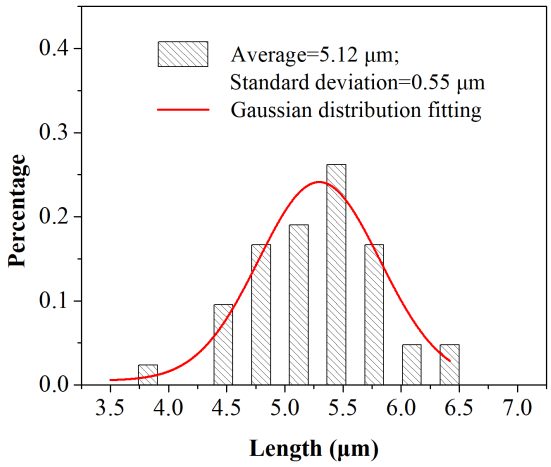

Figure 4.1: Distribution in CNT emitter heights and Gaussian distribution fitting. The CNT emitters have an average height of 5.12 μm and a standard deviation of 0.55 μm, which is 10.7% of the average.

In the experiment, a PMMA 950K A3 thin film layer is spin coated on a piece of ITO coated

glass at a spinning speed of 2000 rpm for 45 s to have a thickness of about 210 nm. The transparent ITO glass as the anode allows direct observation of light emission and Coulomb explosion by a video camera with a microscopic lens and a light source. The gap between the anode and the CNT FEA is 25 μm. A pico-ammeter is used to apply a voltage bias for FE and measure the corresponding FE current from the CNT FEA. The FE experiment is performed at a base pressure of 2×10^8 Torr. In the experiment, the video camera focuses on the PMMA thin film surface. FE current is recorded every 0.5 s by the pico-ammeter. A bias voltage is applied from 300 V and increased by 50 V to find anything that is recorded by the video camera. Video camera recorded 8 explosions at a voltage of 400 V. Then the voltage is increased to 450 V to observer more explosions. Optical microscopic imaging is used to characterize the FEM patterns and explosion impacts on the PMMA thin film. SEM, energy-dispersive X-ray spectroscopy (EDS), and atomic force microscopy (AFM) are used to characterize the CNT emitters and explosions.

4.2 CNT emitter failure behaviour

4.2.1 Direct observation of the CNT emitter failure behaviour

The direct observation by the microscopic video camera shows that CNT emitter explosion occurs independently in the CNT FEA. Video recording of the light emission and Coulomb explosion are available from the videos. Similar as Chapter 3, to address any CNT emitter in the array, we number the CNT emitters. The row is numbered alphabetically from bottom to top and the column is numbered numerically from left to right. Figure 4.2 shows video recording of the entire process of the light emission and the Coulomb explosion at site A-2 in chronological sequence. First, a small FE exposed spot on the PMMA thin film is seen (Figure 4.2(a)). Then, a bright light emission occurs (Figure 4.2(b)). Finally, an explosion occurs in the next 27 seconds creating a“firework-like” pattern on the PMMA thin film surface (Figure 4.2(c))

Similar phenomena are observed from other FE sites. The difference is that the light emission duration and intensity varies from emitter to emitter. Figure 4.3 presents the entire process of a light emission followed by an explosion from the CNT emitter at site F-5 in chronological

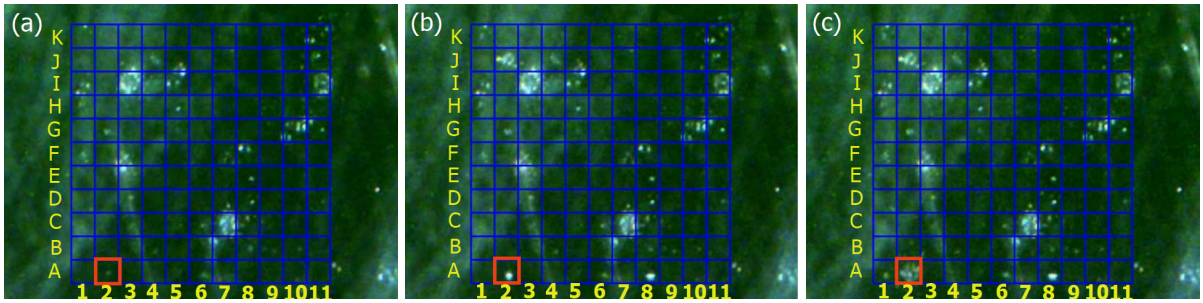

Figure 4.2: The entire process of the light emission and the Coulomb explosion at the site A-2: (a) a FE spot generated, (b) a light emission, and then (c) an explosion.

sequence captured from video recording. A light emission from the CNT emitter at site F-5 occurs (Figure 4.3(b)) and then fades away. A dot is left on the PMMA thin film due to FE exposure (Figure 4.3(c)). After 217 seconds, the light emission re-occurs (Figure 4.3(d)). In the next 5 seconds, an explosion is observed (Figure 4.3(e)).

Figure 4.4 shows the entire process of the light emission and Coulomb explosion at site G-9. The light emission from the CNT emitter increases from nothing (Figure 4.4(a)) to a maximum intensity (Figure 4.4(b) and (c)). Then an explosion of the CNT emitter occurs within the next 2 seconds (Figure 4.4(d)).

4.2.2 Characterization of the CNT emitter failure behaviour

SEM is used to locate the CNT emitters at site A-2 (Figure 4.5(a)), F-5 (Figure 4.5(b)), and G-9 (Figure 4.5(c)). However, in the place of the emitters, melted substrate and explosion debris are found at the each corresponding site. The melted area in the explosion site has a diameter of 10-20 μm. The thin TiN layer and silicon substrate are damaged showing a history of substrate melt. Silicon is exposed according to EDS analysis in the next paragraph. The explosion debris points outward in the radial direction from the explosion centre. The debris, considering the experiment set-up and EDS analysis, is believed to be PMMA. The PMMA thin film is blasted away from the anode surface by the CNT emitter explosion. Figure 4.5(d) shows the magnified SEM image of the melted area in the explosion site at site A-2. Figure 4.5(e) shows four neighbouring FE

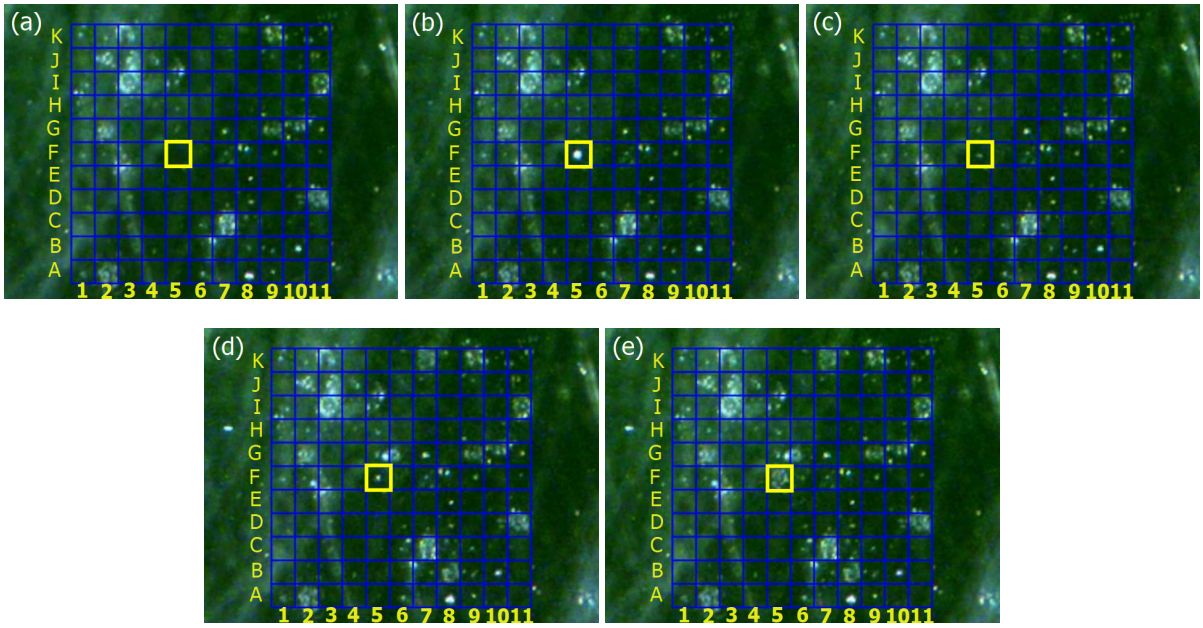

Figure 4.3: The entire process of a light emission followed by an explosion at the site F-5: (a) nothing, (b) a bright light emission, (c) a FE exposed dot generated, (d) re-occurrence of the light emission, and then (e) a CNT emitter explosion.

sites after the experiment: B-6, B-7, C-6, and C-7 from the lower left to the upper right. CNT emitters at site B-7 and C-7 exploded during the emitter failure test while CNT emitters at site B-6 and B-7 remain intact. Figure 4.5(f) shows the site A-10, A-11, B-10, and B-11 from the lower left to the upper right. An explosion crater is found at site A-10 and three CNT emitters are at the other three sites. According to Figure 4.5(e) and (f), the explosion range on the substrate is about 100-120 μm in diameter, which does not affect its neighbouring emitters.

EDS is used to verify that both Joule heating and explosion occur during the CNT emitter failure. The substrate is silicon with a thin layer of TiN of 70 nm on top. CNT is synthesized on TiN layer. Thus Si, Ti, N, and C are the four elements detected. Figure 4.6(a) shows the SEM image of a typical explosion site I-3. The EDS analysis is conducted on the explosion centre, explosion debris, and intact TiN surface of the site, corresponding to spectrum 1, 2, and 3 (Figure 4.6(b)), respectively.

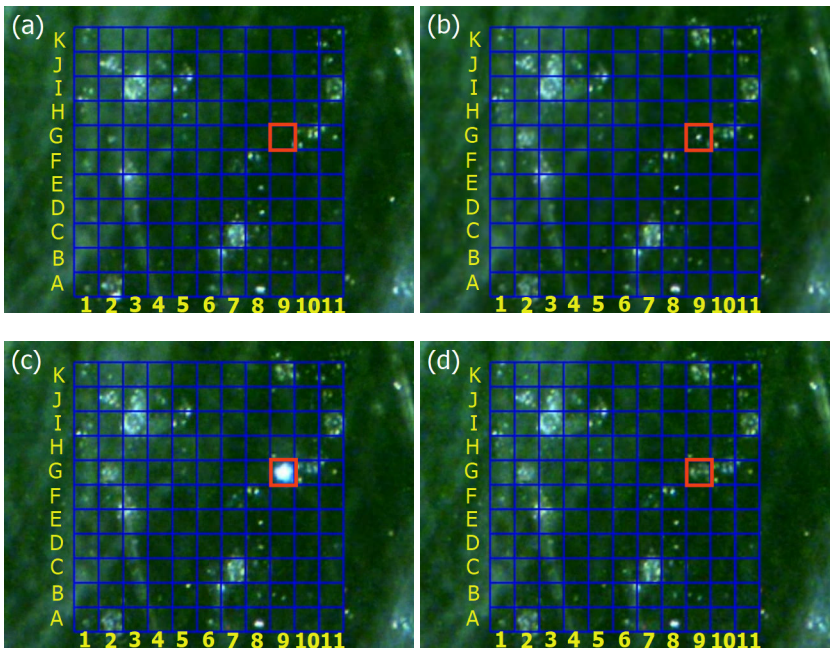

Figure 4.4: The entire process of the light emission and the Coulomb explosion at the site G-9: (a) nothing, (b) a light emission, (c) a maximum light emission, (d) an explosion.

The TiN layer deposited by reactive sputter has an extended range of composition (TiN_x with $0.6 < x < 1.5$) [123]. The atomic percentage ratio of N to Ti of the intact TiN surface is about 1.17, which is calculated from spectrum 3 (Table 4.1). However, compared with the other two spectra, spectrum 1 has the most atomic percentage of Si but the least atomic percentage of N, which means that in the explosion centre TiN layer is damaged and silicon substrate exposes. Spectrum 2 has the most atomic percentage of C. Considering such an amount of explosion remains on the substrate and PMMA chemical formula that is $(C_5O_2H_8)_n$, we believe these explosion remains contain not only CNT fragments but also PMMA from the anode surface. The atomic percentage ratio of Ti and N to Si in spectrum 2 and spectrum 3 are almost the same. This result indicates that the substrate under the explosion debris is intact. Therefore, EDS results verify that Joule heating of CNT emitters melts the contact area and exposes the substrate around the contact area.

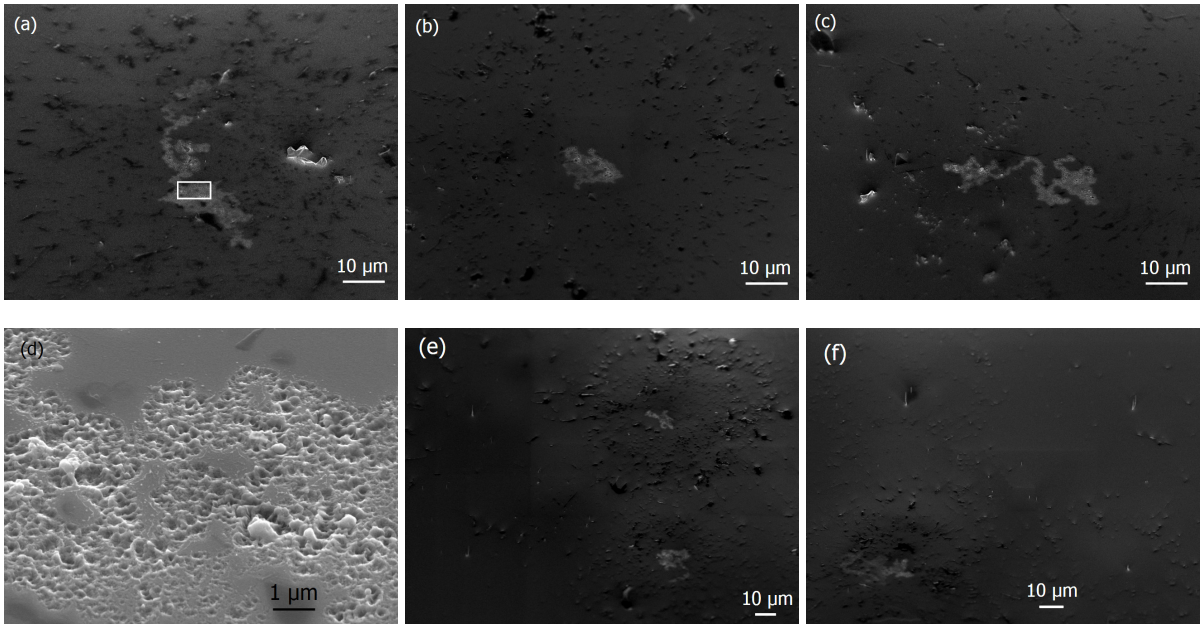

Figure 4.5: SEM images of CNT emitter explosion impact on the substrate at different sites: (a) site A-2, (b) site F-5, and (c) site G-9 after the experiment. No CNT emitter but a melted area in the centre and debris is found at each site. (d) Melted substrate at site A-2. (e) Sites B-6, B-7, C-6, and C-7 from the lower left to the upper right; (f) sites A-10, A-11, B-10, and B-11 from the lower left to the upper right. Explosion debris and craters are found at site B-7, C-7, and A-10. While intact CNT emitters are at site B-6, C-6, A-11, B-10, and B-11. The explosion range on the substrate is about 100-120 μm in diameter and the melted area has a diameter of 10-20 μm. The SEM images are taken at a tilted angle of 45°.

Figure 4.7 shows the optical microscopy images of the explosion impact patterns on the PMMA thin film from site A-2, F-5, and G-9. It can be seen from Figure 4.7 that CNT explosions damage the PMMA thin film at the corresponding sites. Each damaged area has an annular pattern, whether continuous or disconnected, with a diameter of 60-70 μm. PMMA pieces everted on the edge of the annular patterns can be clearly identified. Around the damaged centre, there is a circumferential light area at each site indicating the history of FE exposure. Figure 4.7(a) labels the FE exposure area around the explosion impact. The upper left corner of the ex-

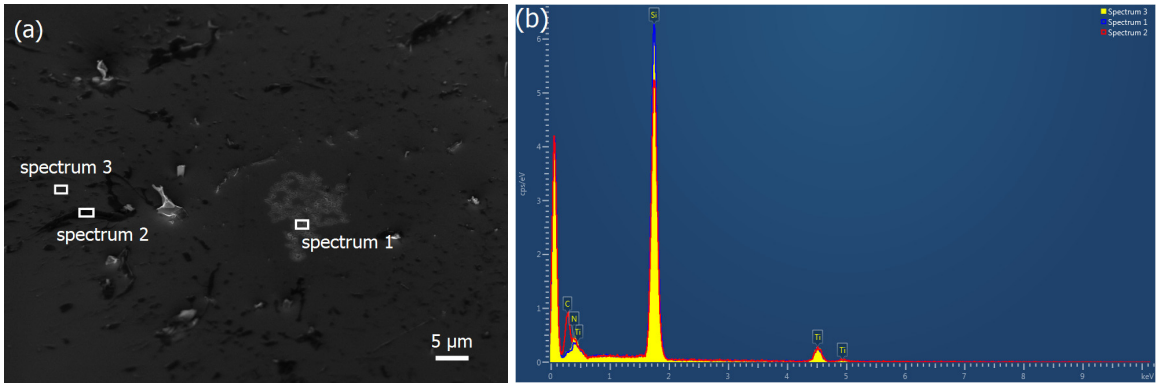

Figure 4.6: EDS analysis of a typical CNT emitter explosion at site I-3: (a) the explosion centre, the explosion debris, and the intact TiN surface. The SEM image is taken at a tilted angle of 45°. (b) Comparison among spectrum 1, spectrum 2, and spectrum 3. Spectrum 1 has the highest peak of Si but lowest peak of N. Spectrum 2 has the highest peak of C but lowest peak of Si.

plosion area on the PMMA thin film at site F-5, which is highlighted in Figure 4.7(b), is further studied by AFM. Figure 4.7(c) highlights the annular pattern of the explosion impact at site G-9. Figure 4.7(d) shows the AFM scanned area which is a 30 μm square containing a quarter of the annular pattern, PMMA pieces on the edge of the annular pattern and PMMA outside the annular pattern. The vertical distance between the intact PMMA thin film surface and the annular pattern marked by two red triangles is about 240 nm. This distance is consistent with the thickness of the PMMA thin fim spin coated on the ITO glass. This result indicates that the annular patterns are impact craters created by the disintegrated CNT emitters. The PMMA pieces are shattered by the explosion impact. According to the annular craters that have a diameter of 60-70 μm, we believe that the repulsive force disintegrates the tubular cone shell of CNTs.

Another FE test is performed using a 10×10 CNT FEA under the same conditions except for no PMMA thin film on the ITO coated glass. This experiment confirms that it is the CNT emitters rather than PMMA thin film or other particles that explode. The difference is that there is no PMMA thin film on the indium tin oxide coated glass and the anode-cathode gap is 50 μm. Explosions at five CNT emission sites are directly observed using the microscopic camera during a scanning voltage FE test from 300 V to 800 V with 5 V step. Among the five exploded

Table 4.1: EDS analysis of atomic percentage of each element from the three spectra.

Element	Line type	Atomic percentage from spectrum 1	Atomic percentage from spectrum 2	Atomic percentage from spectrum 3
C	K series	22.51	53.65	20.12
N	K series	7.84	10.09	15.64
O	K series	3.65	3.64	2.88
Si	K series	57.32	24.96	48.08
Ti	K series	8.67	8.66	13.28

sites, site D-5 is found exploded when the scanning voltage is from 200 V to 700 V of the previous run. Figure 4.8(a) shows the video screen-shot after five explosions. Take site D-8 as an example. Figure 4.8(b) and (c) show the video screen-shot of the site D-8 before and after the explosion occurs, respectively. Figure 4.8(d) shows the optical microscopic image of the anode surface. Except for some particles, no other debris are found on the anode surface. Melted area and explosion craters are also found at the site D-8 on the substrate by SEM (Figure 4.8(e)), indicating a history of high temperature and explosion. Since there is no PMMA thin film on the anode surface, no explosion debris is found around the melted area and explosion craters. The clean substrate surface in return proves that the explosion debris in the 11×11 CNT FEA are sputtered PMMA. Besides, the explosion events themselves are not as visually impressive as those with PMMA thin film on the anode surface. This experiment confirms that it is the CNT emitters rather than PMMA thin film that explode. The damaged PMMA thin film and explosion debris around the explosion sites are caused by the CNT explosion.

In this CNT FEA, as many as 28 CNT emitters exploded according to the video recording and the explosion patterns on the PMMA thin film on the anode surface. Figure 4.9(a) shows the optical microscope image of the FEM patterns and the explosion patterns. A current drop

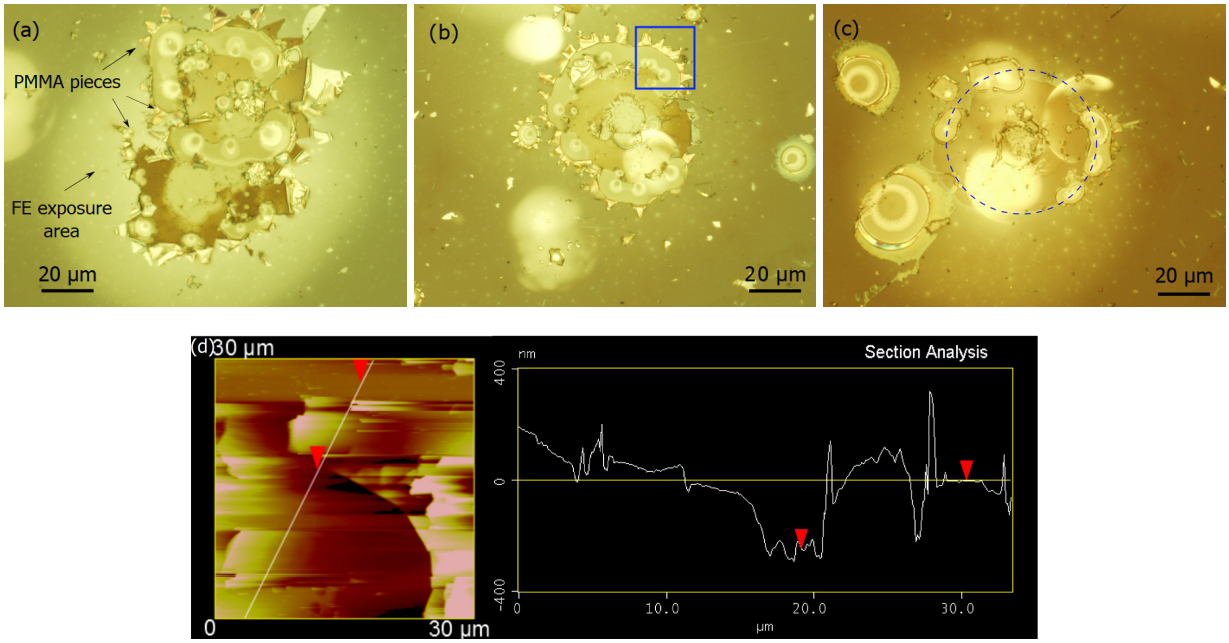

Figure 4.7: Optical microscope images of the explosion patterns on the PMMA thin film: (a) site A-2, (b) site F-5, and (c) site G-9. Each explosion damaged area has an annular pattern with a diameter of 60-70 μm. PMMA pieces can be clearly identified on the edge of the annular pattern. Around the damaged centre, there is a circumferential light area at each site indicating the history of FE exposure. (d) AFM analysis of explosion impact on the PMMA thin film at sit F-5, which shows that the annular is about 240 nm lower than the intact PMMA thin film surface.

right after the explosions is recorded. By considering the 28 exploded CNT emitters, the current drops of the first eight CNT emitters is missing due to the previous tentative experiment to find a proper voltage to cause the emitter failure. The current drops of the other 20 CNT emitters are illustrated in Figure 4.9(b).

The current drop ranges from a minimum 1.95 μA to a maximum 41.82 μA. The average current drop of the 20 disintegrated CNT emitters is 11.82 μA. The majority of current drops is around the average. Since CNT emitters at site B-8 and G-6 explode at almost the same moment, only one current drop of 7.59 μA is found. The same situation is found for the CNT emitters at site G-5 and J-5, which have a current drop of 15.60 μA. We believe these current drops

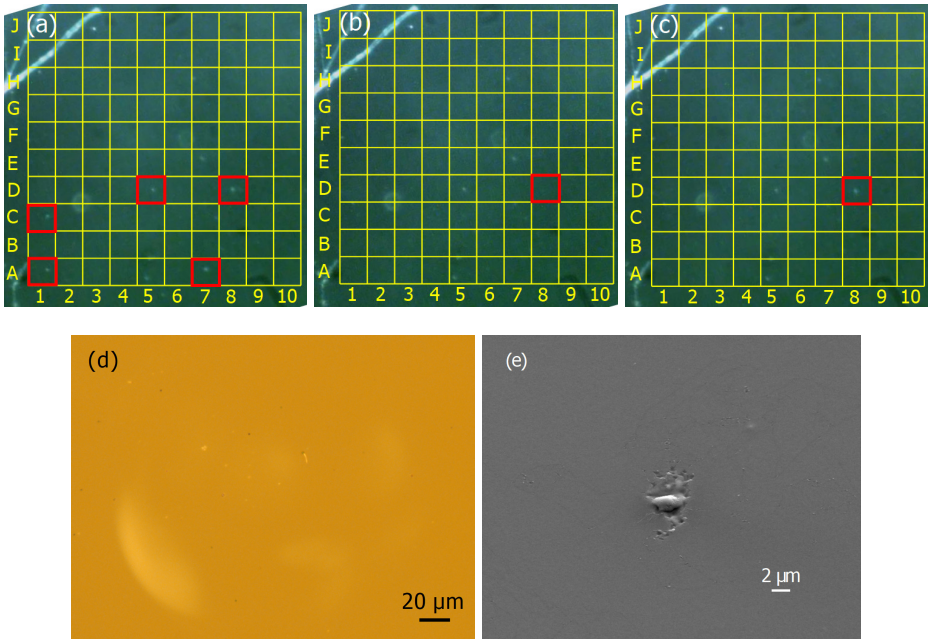

Figure 4.8: Experimental validation of CNT emitter explosion: (a) video screen-shot after five explosions, (b) video screen-shot before an explosion at site D-8, and (c) video screen-shot of the explosion at site D-8. Due to no PMMA on the anode surface, the explosion is not as visually impressive as that with PMMA thin film on the anode surface. (d) Optical microscopic image of the anode surface at site D-8. (e) SEM image of the damaged substrate at the explosion site D-8. Melted area can be clearly identified. There is no debris found on the substrate surface around the explosion site.

are the critical currents that cause the light emission and explosion of the corresponding CNT emitters. Due to the individual difference of CNT emitters in the array, the critical current that CNT emitters can withstand varies. An average emission current of 11.82 μA that causes CNT emitter failure agrees well with the maximum emission current of 10-20 μA from individual CNT that was investigated previously [137]. Figure 4.9(c) and (d) show the overall FE current drop right after the explosion of CNT emitter at the site F-5 and the site G-9, respectively. The overall FE current slightly increased before the explosion at the site F-5 occurs and then decreases by 16.76 μA right after the explosion. The explosion at the site G-9 occurs at an early stage of the

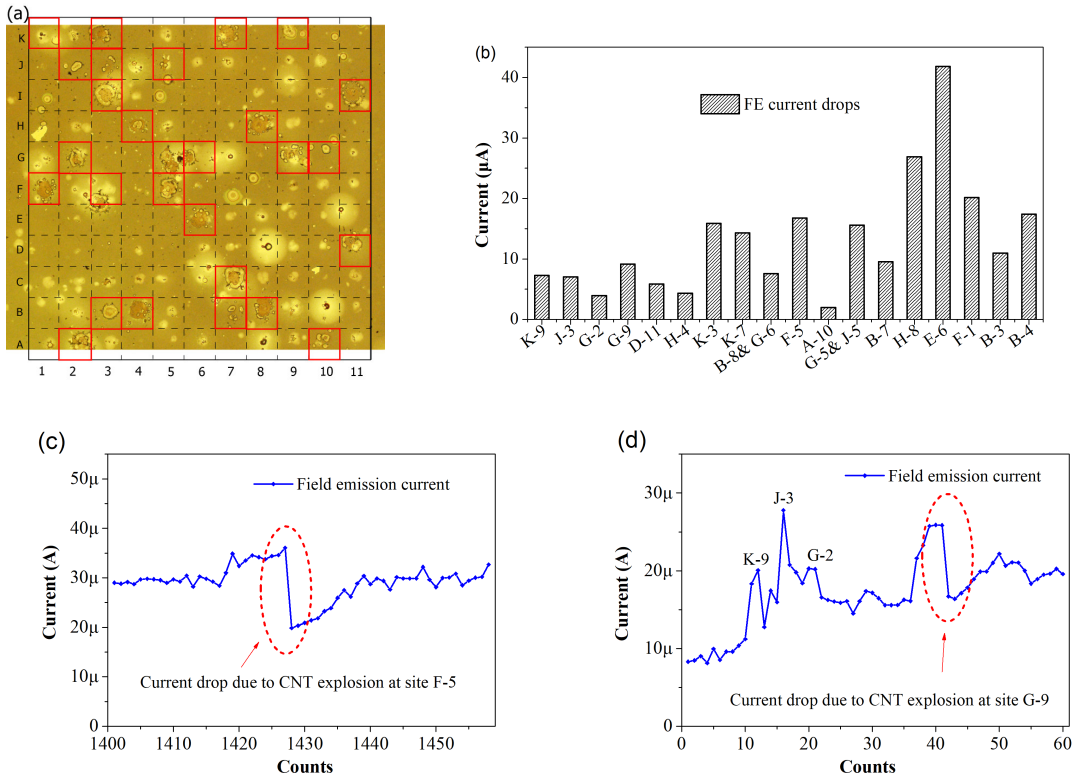

Figure 4.9: (a) The optical microscope image of the FEM patterns and 28 explosion patterns of the 11×11 CNT FEA on the PMMA thin film during the FE failure test. The FEM patterns left by the CNT emitter explosion are highlighted. The other FEM patterns are left by the FE electron exposure. (b) FE current drops right after explosions of CNT emitters of 20 sites. (c) An overall FE current drop of 16.76 μA is recorded right after the CNT emitter explosion at the site F-5. (d) An overall FE current drop of 9.14 μA is recorded right after the CNT emitter explosion at the site G-9. The impact of explosions of three other sites on the overall FE emission current is also shown.

FE test. The overall FE current shows a tendency of increase due to warm-up of the FEA. The FE current increased drastically before the explosion occurs at the site G-9 and then decreases by 9.14 μA after the explosion. We believe that the abrupt current increase and drop cause the CNT emitter at the site G-9 failure. Since the FEA is working at a constant voltage continuously,

after the explosions the overall FE current tends to increase as the Joule heat accumulates.

4.3 CNT field emitter failure mechanism

4.3.1 Coulomb explosion of CNT emitters induced by FE

Based on the above study, we attribute the disintegration of CNT emitters and the blasting of PMMA to Coulomb explosion [138]. It is defied classically by Rayleigh instability limit, above which an excessively charged cluster becomes unstable and explodes into smaller fragments [139, 140]. In this case, we model the CNT emitter as a cylinder with a height of 5 μm and a diameter of 100 nm. The quantity of charges that a CNT emitter can hold is given by the Rayleigh limit [139, 140].

$$Q_R{}^2 = 6\pi^2\varepsilon_0\gamma l^2 r \tag{4.1}$$

In the Equation 4.1, $\varepsilon_0 = 8.85\times10^{-12}\ \mathrm{F\cdot m^{-1}}$ is the vacuum permittivity; $\gamma = 40.3\ \mathrm{mN\cdot m^{-1}}$ is the surface tension coefficient of CNT [141]; $r = 50$ nm is the radius of the CNT; $l = 5\ \mu$m is the height of the CNT. Thus, the charges to overcome the Rayleigh limit are calculated to be 5.14×10^{-15} C. The charge on a CNT emitters during FE can be calculated from the relationship between the current and the charge.

$$I = nAve \tag{4.2}$$

In the Equation 4.2, I is the current; n is number of charged particles per unit volume; A is the cross-sectional area of the CNT emitter; v is the drift velocity; e is the charge on each particle. The drift velocity is a function of electron mobility, μ, and electric field, E.

$$v = \mu E \tag{4.3}$$

Since CNT is composed of stacked curved graphene layers, CNT has the similar properties as graphite [8]. The electron mobility of multi-layer graphene, which is 3000 $\mathrm{cm^2\cdot V^{-1}\cdot s^{-1}}$, is chosen as the electron mobility of CNT [142]. Using Equation 4.3, the total charges on the CNT is 3.13×10^{-15} C. The linear charge density of is $6.25\times10^{-10}\ \mathrm{C\cdot m^{-1}}$, corresponding to

$4.04e$ nm^{-1}, which is comparable with that overcomes the van der Waals force among SWNT bundles [143]. The charge on the CNT emitter is just the same order of magnitude as that of the Rayleigh limit. However, considering the size of annular crater on the PMMA thin film and the size of sputtered PMMA on the substrate, Coulomb energy not only overcomes the surface energy of CNT but also provides kinetic energy for the CNT fragments. Heating and chemical reaction is able to aid the Coulomb explosion [144, 145]. In this case, only Joule heating helps break the carbon chains at a lower electric field at the CNT surface. Besides, we also find that Joule heating alone cannot disintegrate CNT emitters. At site A-1, site J-7, and site B-10, there is only light emission observed at each site during the test. However, no damage is found in the SEM images of each CNT emitter at the three sites. Therefore, it is the Coulomb force of excessive charging with the aid of Joule heating that disintegrates the CNT. Figure 4.10 presents the SEM images of the CNT emitters at the three sites after the FE test together with the video recording of light emission at each site.

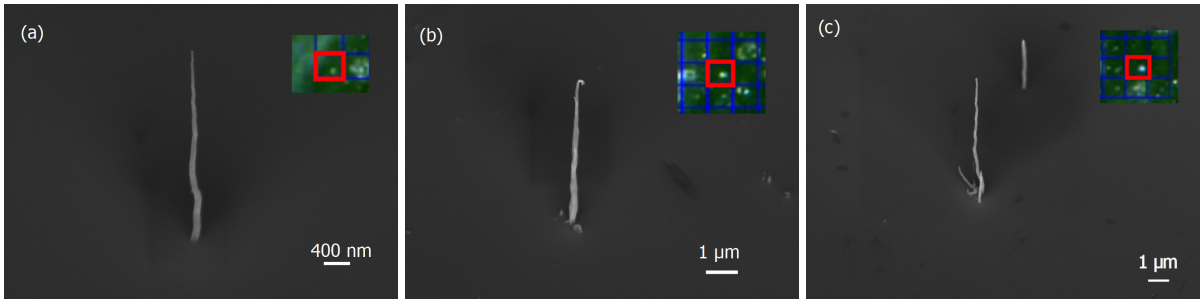

Figure 4.10: SEM images of CNT emitters at (a) site A-1, (b) site J-7, and (c) site B-10 after the experiment. Only light emission is observed at each site during the FE test. However no damage of each CNT emitter is found after the FE test. The insert of each SEM image is the video recording of the light emission at each corresponding site. The SEM images are taken at a tilted angle of 45°.

Similar structure damage has been reported that electrical charging cause the outer layer of repelling from MWNT emitters [11, 58]. After the CNT disintegrated, the fragments accelerated by the bias voltage touch the PMMA thin film surface. In the meantime, since the CNT has a tubular cone structure, the charged fragments retain an annular pattern of the CNT shell while

expanding and flying towards the anode. The stacked curved graphite layers that form tubular cone structure of CNT emitters is verified by TEM images reported previously and by our mechanically damage CNTs on the marker with a typical CNT lying beside, which is shown in Figure 4.11. When the charged fragments reach the PMMA thin film surface, an almost immediate release of electrons, from charged CNT fragments through the PMMA thin film to the anode, occurs and results in sputtering PMMA all around and an annular crater with PMMA pieces on the PMMA thin film surface due to the almost immediate electrons migration from CNT fragments to the PMMA thin film. This step is similar to the Coulomb explosion phenomenon of a piece of alkali metal drops into water [135]. Considering the size of annular crater on the PMMA thin film and the size of a CNT emitter, such an impact is astonishing. The entire process is like firing a shotgun combined with pellets exploding on the target.

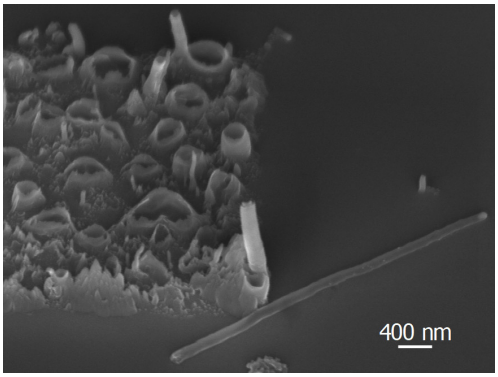

Figure 4.11: Mechanically damaged CNTs on the marker with a typical CNT lying beside, showing a tubular cone structure of the CNT.

4.3.2 Joule heating of CNT emitters induced by FE

Joule heating is often reported in FE studies as a potential degradation of CNT emitters operating at large current [11, 84, 128]. Moderate Joule heating can cause a rise in the overall FE current on the account of temperature dependence of FE [126, 127]. However, too much Joule heating causing the rise of FE current would cause more heat generated. The phenomenon of FE-induced light emission is previously observed when CNT emitter temperature is above 1500 K or a FE

current of 20 μA, which increases in intensity as temperature rises [146, 147]. Considering the melted substrate and the light intensity variation observed at the corresponding CNT emitter failure sites, the light emission is an incandescence effect due to Joule heating, indicating that CNT emitters are working at a very high temperature. Therefore, the effect of temperature due to Joule heating during FE should be taken into account. Thermal equilibrium of Joule heating on CNT emitter can be obtained by heat dissipation. The maximum temperature of the CNT emitter due to Joule heating is determined by several parameters such as emission current, resistance, and size. Finite element analysis method is used to simulate this process. The transient study of CNT Joule heating induced by FE is performed by COMSOL Multiphysics software. The PECVD synthesized CNT has a thermal conductivity of around 80 $W \cdot m^{-1} \cdot K^{-1}$ [147]. The specific heat is reported to be 713 $J \cdot kg^{-1} \cdot K^{-1}$ and the mass density is around 1300 $kg \cdot m^{-3}$. The resistance of PECVD CNT is reported to be 10^{-6} to 10^{-5} $\Omega \cdot m$ [138, 148]. The model here studied is a hollow cone structure with a base diameter of 100 nm, tip diameter of 35 nm, cone wall thickness of 20 nm, and a length of 5 μm. Heat loss in the simulation is caused by thermal radiation. Since the fabrication randomness that would cause the deviation of emitter size, two different CNT base diameters are compared. Figure 4.12 presents finite element analysis of the effect of Joule heating on maximum temperature of CNT emitters during FE under different conditions.

Figure 4.12(a) shows that temperature of a CNT emitter at higher FE current reaches maximum temperature faster at the same conditions. However, it takes very short time (1 ms) for FE current to reach thermal equilibrium even at a FE current of 1 μA. Therefore, Joule heating of CNT emitters during FE at a certain critical current is almost an instantaneous process. Figure 4.12(b) shows the maximum temperature of a CNT emitter can reach with different FE current levels. A thicker emitter is able to withstand higher critical FE current compared with a thinner one. While the CNT emitter height influences the critical FE current negatively compared with the effect of the CNT diameter. Figure 4.12(c) illustrates the electrical conductivity of CNT emitters on the temperature of CNT at a constant current of 10 μA. A CNT field emitter of higher electrical conductivity reaches lower temperature. Besides, the results show that a FE current of 5 μA is able to heat a CNT emitter to over 1500 K. Thus, the average current drop of 11.82 μA can heat a CNT emitter to over 2500 K. Considering the melting point of Si and TiN which is

1687 K and 3203 K, respectively, a temperature over 2000 K is able to melt the silicon beneath the contact area, which would lose the support of CNT emitters. In practical situations, defects in CNT reduce the melting temperature of atoms around the defects [149].

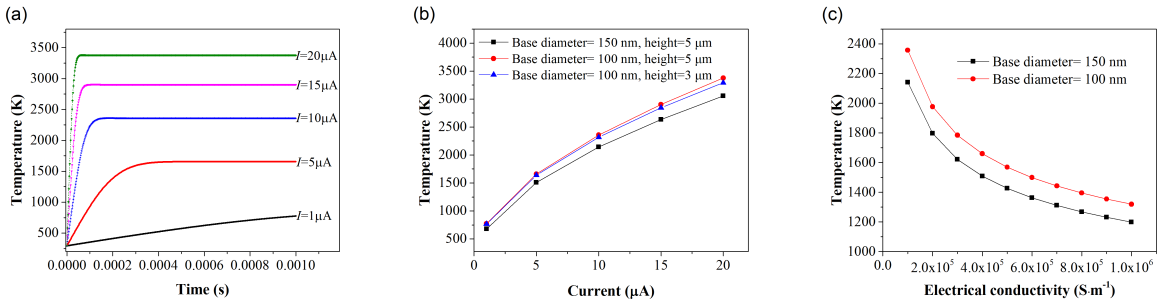

Figure 4.12: Finite element analysis of the effect of Joule heating on maximum temperature of CNT emitters during FE. (a) CNT emitter temperature varies with time at different FE current. (b) Maximum temperature of CNT emitters of different base diameters and height varies with different FE current levels. (c) Temperature varies with electrical conductivity at 10 μA FE current.

Theoretical analyses of electron emission over a wide range of temperatures and fields have been studied previously [19, 150]. Such thermal enhanced FE is defined as Schottky emission. Since this type of electron emission is a combined effect of electric field and heat, mathematical description of Schottky emission contains both effect of the electric field (E in volts per centimetre) and the temperature (T in Kelvin) [150]. For $E \leq 160T^{1.33}$, the electron emission is classified as "Schottky emission". For $E \leq 1100T^{1.33}$, the electron emission is classified as "extended Schottky emission". In our case, the bias voltage applied on the CNT FEA is 450 V. The distance between the anode and the cathode is 25 μm. Considering the our CNT field emitters have an average aspect ratio of 100, an enhanced electric field of 1.8×10^7 V $\cdot$ cm^{-1} is applied at the CNT emitter tip. Therefore, under such an electric field, extended Schottky emission is achieved at a temperature of 1447 K. Higher temperature causes the thermal induced electron emission becoming prominent and converts FE into Schottky emission regime. Therefore, the increasing electron emission current increases the CNT emitter temperature and generates more heat. Consequently, the high temperature weakens the CNT carbon bonds. As a result, the

excessive charging on CNT emitters ultimately disintegrates the CNT emitters.

4.3.3 CNT emitter failure mechanism induced by FE

Based on above study, the entire process of CNT emitter failure behaviour can be represented in detail. At high FE current, Joule heating heats the CNT emitter to a high temperature. The high temperature increase the thermal induced electron emission and cause more electron emitted. In the meantime, light emission occurs and substrate begins to melt. With the aid of high temperature, excessive charging overcomes the van der Waals forces among graphite basal planes and CNT carbon bonds. Since the CNT has a tubular cone structure (Figure 4.11), the shell is broken apart by the charging on the CNT into charged fragments at high temperature. The charged fragments retain an annular pattern of the CNT shell while expanding and flying towards the anode. When the charged fragments reach the PMMA thin film surface, an almost immediate release of electrons, from charged CNT fragments through the PMMA thin film to the anode, occurs and results in another Coulomb explosion. The explosion blast away and sputter the PMMA debris and leaves an annular crater with PMMA pieces on the PMMA thin film surface.

Due to the individual difference of CNT emitters in the array, the critical current that disintegrates CNT emitters varies. Finite element study shows that a thicker emitter is able to withstand higher critical FE current compared with a thinner one. While the CNT emitter height influences the critical FE current negatively compared with the effect of the CNT diameter. A CNT emitter of higher electrical conductivity reaches lower temperature. In practical situations, defects in CNT reduce the melting temperature of atoms around the defects. Therefore, thinner and taller CNT emitters with lower electrical conductivity and more defects are more likely to explode during FE. In order to illustrate the mechanism of the Coulomb explosion of CNT induced by FE and the difference between normal FE and Coulomb explosion, we take four neighbouring CNT FE sites in the lower right corner of the 11×11 CNT FEA as an example. The four neighbouring sites are A-10, A-11, B-10, and B-11. The explosion sites on the substrate of these four sites is already shown in Figure 4.5(f). Figure 4.13 shows the illustration of the CNT Coulomb explosion process and a normal FE process from CNT emitters. These four sites contain all the FE status during the CNT emitter failure test. From the video recording and the FEM patterns

(Figure 4.13(c)) on the PMMA thin film surface, Coulomb explosion occurs at site A-10, a strong FE with light emission occurs at site B-10, and weak FE occurs at site A-11 and B-11. Explosion craters at site A-10 are clearly shown on the PMMA thin film. FE performance of the other three sites are distinguishable from the FEM patterns on the PMMA thin film.

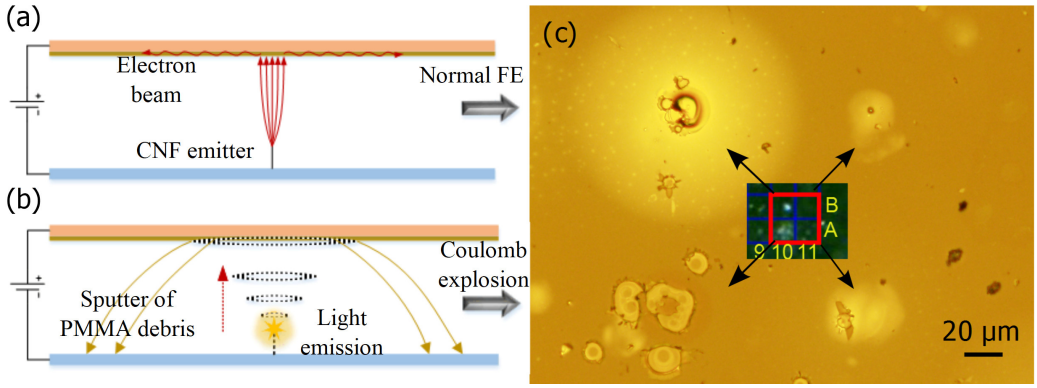

Figure 4.13: Illustration of the CNT Coulomb explosion process and a normal FE process from a CNT emitter: (a) a normal FE process, (b) a Coulomb explosion process of a CNT, (c) FEM patterns at site A-10, site A-11, site B-10, and site B-11 with a video recording of the corresponding sites inserted. The inserted video screen-shot shows an explosion at site A-10 and a light emission at site B-10, which is also clearly reflected on the PMMA thin film. FEM patterns also indicate lighter FE performance from the site A-11 and B-11.

4.4 Chapter summary

In the chapter, starting with the direct observation of the unique behaviour by a microscopic video camera, the process of a light emission and Coulomb explosion induced by FE is represented. Then the Coulomb explosion of CNT induced by FE is systematically characterized by the direct observation of the phenomenon using a microscopic camera, optical imaging and AFM study of the permanently damaged patterns of the PMMA thin film, and SEM imaging and EDS analysis of the explosion sites. The light emission, an incandescence effect due to Joule heating, is further investigated by finite element analysis and theoretical calculation. The light

emission followed by the Coulomb explosion that causes CNT emitter failure is due to a combined effect of Joule heating and massive charging at high FE current. The FE current levels that disintegrate the CNT emitters range from 1.96 μA to 41.82 μA with an average of 11.82 μA. Joule heating is able to heat a CNT emitter to over 2500 K within a very short period, melt the contact area, and weaken the carbon bond and van der Waals force of graphite basal planes in the CNT. With the aid of Joule heating, extended Schottky emission is achieved at a temperature of 1447 K and excessive charging disintegrates the CNT emitters into charge fragments. Then an instantaneous release of electrons from CNT fragments through the PMMA thin film leading to the annular crater and the sputter of PMMA all around in a range of about 100 mm. The explosion generates an annular crater on the PMMA thin film of about 60-70 μm indicating a strong Coulomb energy that causes the Rayleigh instability. Besides, finite element study shows that during FE thinner and taller CNT emitters with lower electrical conductivity and more defects is likely to explode than others. This study successfully explains the mechanisms behind the absence of CNT emitters after FE, which is often simply attributed to uprooting or burning out of the emitter. The detailed study of Coulomb explosion of CNT induced by FE allows an insight of destruction of other nano-wires during electrical transport and a systematic design of FE devices for long-lasting operation in practical applications. In addition, although Coulomb explosion destroys CNT emitters, considering such astonishing destruction, potential application of blasting and bombardment using CNT FE at micro-/nano-scale can be expected.

Chapter 5

Individually ballasted CNT FEAs using silicon current limiter

Realizing stable and reliable CNT FEAs for practical applications continues to be a challenge. As a type of nano-material, CNT field emitters tend to have dissimilar size and morphology. It is understood that even a small variations in the tip radii or emitter heights of the FEA will result in the variation in the local electric field enhancement among the tips and consequently a large variation of FE current from each emitters. Consequently, such unequal FE current contribution from emitters within a CNT FEA at a given control voltage leads to dominating CNT emitters that exceed their maximum current and are irreversibly degraded [11, 12, 151]. CNT field emitters' unequal current contribution to the overall CNT FEAs and Coulomb explosions of CNT under high FE current have been observed and reported in previous studies [129, 151]. As such, CNT FEA-based cathodes have not been widely applied in practical applications. These challenges are limiting the development of potential applications such as multi-beam X-ray sources, and FFMCT.

To address these issues, much effort has been devoted to overcoming the non-uniformity of FE current contribution from each emitter due to the geometry variation of FE devices. The presence of ballast resistors in series with field emitters to individually ballast FE from each CNT emitters is a potential solution. The resistors create a voltage drop so the voltage across the domi-

nating CNT field emitters is reduced. Hence, the FE current is restricted to the average level [12]. In our previous studies, we designed and fabricated ballasted CNT FEA by using large resistor in series with CNT field emitters to achieve uniform FE current of the CNT FEA [10,12]. However, we find that this approach reduces non-uniform FE current contribution at the expense of lower overall FE current and generates large power dissipation. The voltage drop is much larger across the resistor than on the CNT field emitter. As a result, the corresponding electric field to extract electrons from CNT emitters is greatly lowered. An ideal method is to limit the FE current from each emitter under a safe current level without losing the FE efficiency. For example, MOSFET has been used as a current limiter [14, 88]. however, this approach is complex and expensive to achieve. Besides, MOSFET occupies a large area if used for ballasting individual CNT field emitter. By exploiting the advantages of carrier velocity saturation in silicon, well designed silicon current limiter in series with field emitters can limit FE current from individual emitter at a desired current level. In addition, the fabrication process and implementation of this approach is more straightforward. This approach is able to resolve two main disadvantages of using large resistors in series with the emitters: (i) large power dissipation, (ii) uniform FE current contribution at the expense of lowering overall FE current level. Individually ballasted FEA using carrier velocity saturation of well-doped silicon current limiter has been applied on silicon FEAs and CNT clusters [35–38]. If vertically aligned CNT field emitter can also be individually ballasted by this effective approach, CNT FEAs will be able to achieve uniform and long-lasting operation without compromising high FE efficiency and current level. However, there has been little work on individually ballasted CNT FEA using this approach. One main reason for the lack of previous work is the fabrication complexity. For silicon FEA, fabrication of silicon field emitters individually in series with silicon current limiters can be realized by patterning and etching a silicon substrate directly. In order to achieve CNT field emitters individually in series with silicon current limiters, the fabrication process should include nano-patterning of CNT FEA, alignment of CNT field emitter sites with silicon current limiter sites, and synthesis of CNT field emitters on top of the silicon current limiters. Therefore, innovative design and fabrication of individual CNT field emitters ballasted by silicon current limiters are required to provide stable and reliable operation of CNT FEAs.

5.1 Device design and fabrication

In our previous studies, we used ballast resistors in series with CNT FEA to achieve uniform overall FE [10, 12]. By employing a ballast resistor in series with each CNT field emitter, the control voltage is shared by the ballast resistor resistance and transimpedance of FE. The relationship between FE current, I, and control voltage, V, can be approximated by a modified F-N equation [12, 23–25, 152]:

$$I = r^2 \frac{B\left(\beta\left(V - IR\right)/G\right)^2}{\varphi} \exp\left(-\frac{C\varphi^{3/2}}{\beta\left(V - IR\right)/G}\right) \tag{5.1}$$

where B and C are constants, φ is the work function of CNTs, and E is the electric field strength. Due to the extreme small radii, r, of CNT tips, the electric field is enhanced at the CNT tips by the field enhancement factor, β. R is the resistance of the ballast resistor, G is the anode-cathode gap, I is the FE current, and V is the control voltage.

When there is no ballast resistor applied, a 20% variation of field enhancement factor leads to a large variation of emission current of about 1,003% [12]. When ballast resistors are placed in series with CNT field emitters, the ballast resistors can lower the FE current of those higher field enhancement factor emitters by sharing the voltage bias. Therefore, the voltage to extract electrons from the CNT emitters is decreased. As a result, the overall FE current is lowered. A 150 MΩ resistor, for example, is able to decrease the FE current level of CNT field emitter with a large field enhancement factor to lower than 1 μA. However, the large resistance leads to a huge voltage drop and large power consumption. Consequently, uniform FE current is achieved by sacrificing FE performance of field emitters with higher current emission. These effects limit the overall FE current of the CNT FEA to a low current level. Figure 5.1 shows that when a larger resistor is used, it becomes much more difficult to achieve a higher FE current by increasing the control voltage since higher voltage applied leads to higher voltage drop on the ballast resistor. The FE process itself does not benefit from the increased voltage. Theoretically, for a CNT field emitter with a gate-emitter gap of 500 nm (no ballast resistor), 50 V gate voltage is needed to achieve an electric field of 100 $\mathrm{V}\cdot\mu\mathrm{m}^{-1}$ to generate a FE current of 4 μA. However, if there is a 200 M resistor applied, an electric field of about 2,000 $\mathrm{V}\cdot\mu\mathrm{m}^{-1}$ is needed to generate a

FE current of 4 μA. Furthermore, the voltage is required for a resistor of 1 GΩ is too large to be practically achieved. Therefore, the sensitivity of FE is greatly reduced. The uniformity is achieved by sacrificing the FE current level.

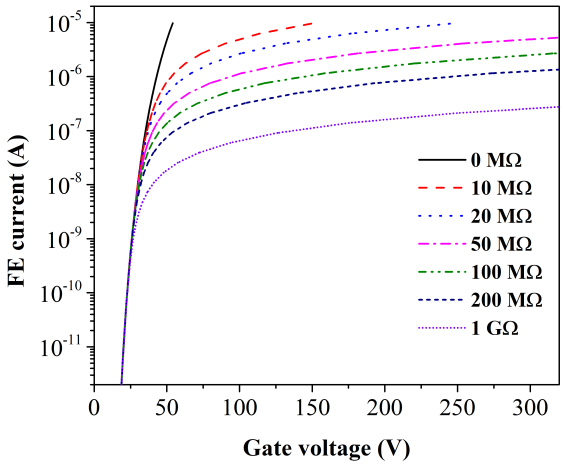

Figure 5.1: FE current in relation with gate voltage of different ballast resistors.

Silicon current limiter exhibits dynamic resistance to limit FE current below the maximum current that a single CNT emitter can withstand, and hence protects emitter integrity and functionality. To achieve FE current limitation without reducing the FE efficiency and current level, a silicon current limiter is used. The conductivity of doped silicon is determined by carrier concentration n, electron charge e, and carrier mobility μ, where mobility is the slope of the drift velocity (v_d) versus electric field. Under low applied voltage, the current is proportional to the voltage. As the voltage increases, the electric field inside the current limiter reaches a high electric field (for example 30 $\mathrm{kV \cdot cm^{-1}}$). In the meantime, the drift velocity increases and saturates at the thermal velocity (10^7 $\mathrm{cm \cdot s^{-1}}$) to give rise to saturation current. The current can be described as:

$$I = n\mu \frac{V}{L} Ae = nv_d Ae \tag{5.2}$$

where L and A are the length and cross section area of the doped silicon, respectively. From Equation 5.2, by defining the geometric size and doping density of the doped silicon, a desired

saturation current can be set to limit the FE current from each CNT emitter and thus avoid over current in CNT emitters.

The saturation currents of silicon current limiter were simulated using COMSOL Multiphysics 5.1 based on finite element methods. A 10 μm length n-type doped silicon with a cross section area of 1 μm^2 and various doping concentration is designed. Figure 5.2 shows the current-voltage characteristics. In the simulation, the voltage used ranges from 0 to 100 V. As the voltage increases, current through the model saturates. The saturation current and the doping density have an approximate linear relationship. Desired maximum current can be achieved by varying the doping level of the n-type silicon current limiter. In addition, according to Equation 5.2, for the same doping density, varying cross section area of the doped silicon resist can also result in a variation of the saturation current. Therefore, the overall FE current can be limited at a desired current level.

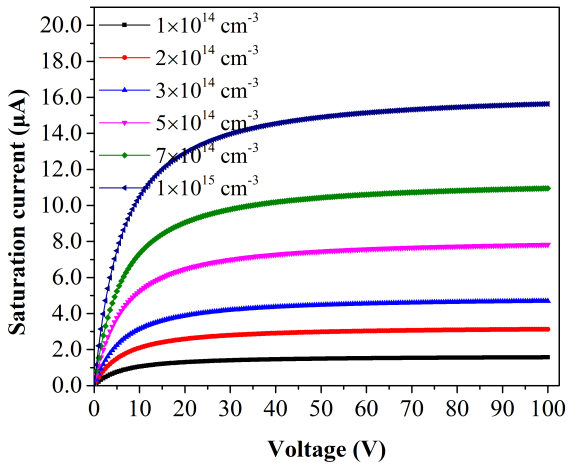

Figure 5.2: The current-voltage curve of a 10 μm length n-type doped silicon with various doping concentrations and a cross section area of 1 μm^2.

In the previous study, a CNT field emitter can be permanently damaged by a current ranging from 1.95 μA to over 40 μA [13]. According to the simulation results, current saturation through a 10 μm length n-type doped silicon with a doping concentration of 1×10^{14} cm^{-3} and a cross

section area of 1 μm^2 is 1.56 μA, Therefore, we use n-doped silicon current limiters with a doping concentration of 1×10^{14} cm^{-3}, a cross section area of 1 μm^2, and a length of 10 μm.

Figure 5.3 illustrates the fabrication process of silicon current limiters in series with CNT emitter. First, a 50 nm TiN layer is deposited on a clean silicon substrate. Then catalyst dot array (Ni) is patterned using EBL using PMMA 950K A3 as resist (Figure 5.3(a)). Each catalyst dot has a diameter of 100 nm. After the development, the catalyst dots are deposited by an electron beam evaporator to have a thickness of 30 nm (Figure 5.3(b)). Then, 6% hydrogen silsesquioxane (HSQ) resist is spin-coated as the secondary pattern of the cross section area of the silicon current limiter array (Figure 5.3(c)). HSQ is a type of negative resist serving as the etching mask in the next steps to build silicon current limiter pillar arrays. The cross section area of the silicon current limiters is a regular octagonal pad with a radius of 1 μm. The patterned HSQ resist is developed in 25% tetramethylammonium hydroxide (TMAH) solution. Next, RIE is used to etch the TiN thin film to fabricate connection pad arrays (Figure 5.3(d)). This step is followed by a deep reactive ion etching (DRIE) process to etch 10 μm silicon pillar structure down the substrate (Figure 5.3(e)). The etching mask, exposed HSQ, is removed by buffered oxide etch. After the silicon current limiters are built, individually vertically aligned CNT field emitters are synthesized on top of the silicon current limiters by PECVD (Figure 5.3(f)). The CNT field emitters are synthesized the same as described in the previous chapters.

Figure 5.4 shows the SEM image of several key fabrication steps of the CNT FEA with silicon current limiter. The silicon substrate for the fabrication are n-type prime wafers with a thickness of 480 μm. The wafers have a doping concentration of 1×10^{14} cm^{-3}. The measured sheet resistance is 738 $\Omega \cdot sq^{-1}$ at room temperature, corresponding to a resistivity of 35.42 $\Omega \cdot cm$ and a doping concentration of 1.25×10^{14} cm^{-3}. Figure 5.4(a) illustrates the octagonal pad array of the HSQ resist on the TiN layer after the secondary EBL pattern and developed by 25% TMAH. Ni dots can be clearly seen in the center of the octagon pads. Figure 5.4(b) shows the one octagonal pad of the HSQ resist from the array. The Ni catalyst dot is covered by the HSQ resist. Figure 5.4(c) shows the octagonal pad after the TiN etching. The diameter of the octagonal pad is 1 μm. Figure 5.4(d) shows the top of the silicon current limiter pillar after the DRIE process (HSQ removed). The DRIE of silicon current limiters is achieved by Bosch process for 16 cycles. Each etching cycle etches about 630 nm in depth. Then, CNT field emitters are synthesized on

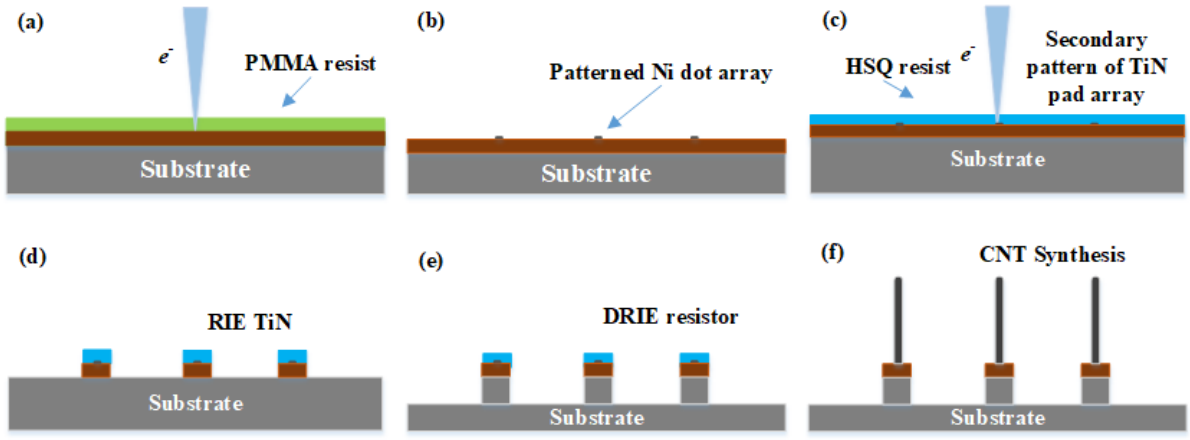

Figure 5.3: Fabrication process of silicon current limiters individually in series with CNT field emitters. (a) Ni catalyst dots pattern using EBL and PMMA 950K A3 resist. (b) Electron beam evaporation and lift-off of patterned Ni dots. (c) Secondary pattern of silicon current limiter using EBL and 6% HSQ resist. (d) RIE of TiN layer. (e) DRIE of silicon current limiter. (f) PECVD synthesis of CNT field emitters on-top of the silicon current limiters.

top of the silicon pillars by PECVD. Figure 5.4(e) show a CNT FEA with 10×10 CNT field emitters and inter-emitter distance of 100 μm. Figure 5.4(f) shows a CNT FEA with 8,260 CNT field emitters within a regular octagonal area of 1 mm^2 and an inter-emitter distance of 10 μm. The average height of the CNT field emitter is about 6 μm and the height of the silicon current limiter is about 10 μm. Figure 5.4(g) shows a typical CNT field emitter synthesized on-top of a silicon current limiter.

5.2 Device characterization and discussions

The FE experiment set-up consists of an anode, a CNT FEA as the cathode, and a 50 μm thick Teflon film as a spacer in-between the anode and the cathode. A pico-ammeter is used to apply a voltage bias for FE and measure the corresponding FE current from the free-standing CNT FEAs. The experiment is performed in a vacuum chamber with a base pressure of 2×10^{-8} Torr.

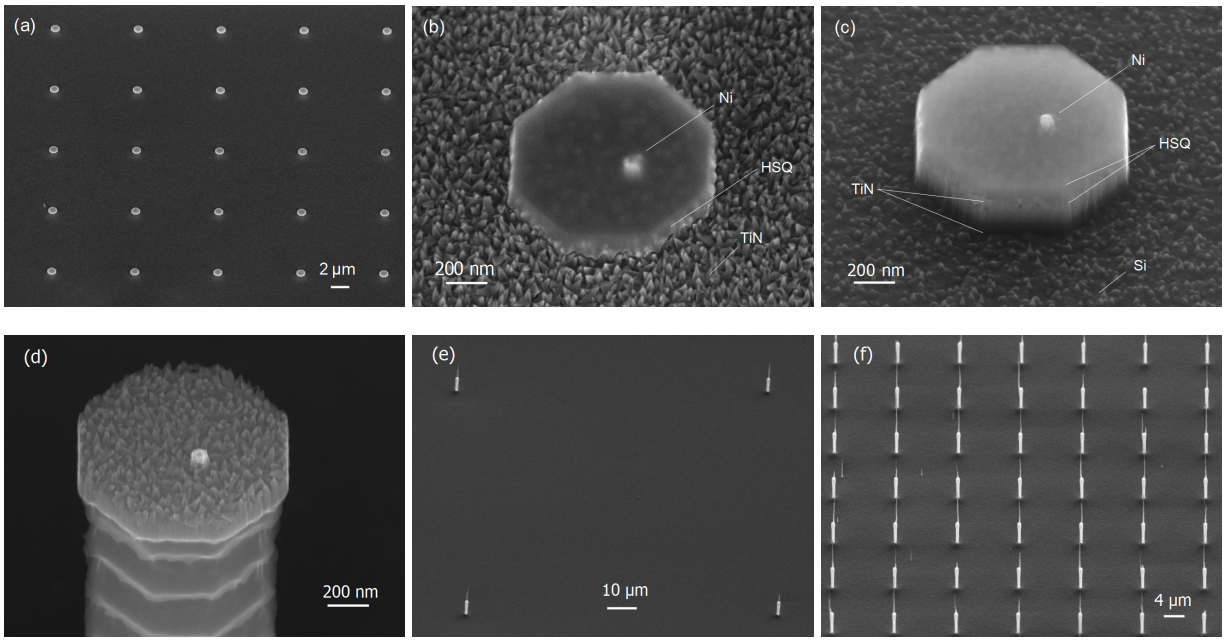

Figure 5.4: SEM images of several key fabrication steps of the CNT field emitters in series with silicon current limiters. (a) The octagonal pad array of the HSQ resist on the TiN layer after the secondary EBL pattern. (b) An octagonal pad of the HSQ resist from the array. (c) The octagonal pad after the TiN etching. (d) The silicon current limiter pillars after the DRIE (HSQ removed). CNT field emitters synthesized on top of the silicon current limiters by PECVD: (e) A CNT FEA containing 10×10 CNT field emitters and inter-emitter distance of 100 μm; (f) A CNT FEA with 8,260 CNT field emitters within a regular octagonal area of 1 mm^2 and inter-emitter distance of 10 μm. The SEM images are taken at a tilted angle of 45°.

Sample 1 studied is the CNT FEA containing 10×10 CNT emitters (Figure 5.4(e)). In the experiment, the voltage sweeps from 500 V to 800 V. A FE current of 8.13 μA is achieved at a voltage of 800 V, which corresponds to 81.3 nA per emitter. Figure 5.5(a) shows the FE current-voltage curves of the CNT FEA with individually ballast silicon current limiter. Figure 5.5(b) shows the corresponding F-N plot, in which normal FE and ballasted FE regions are highlighted.

An ideal FE without ballast should have an F-N plot of a straight line [23–25]. In Figure 5.5(b), the F-N plot consists of two linear segments. The F-N plots from 500 V to about 600 V

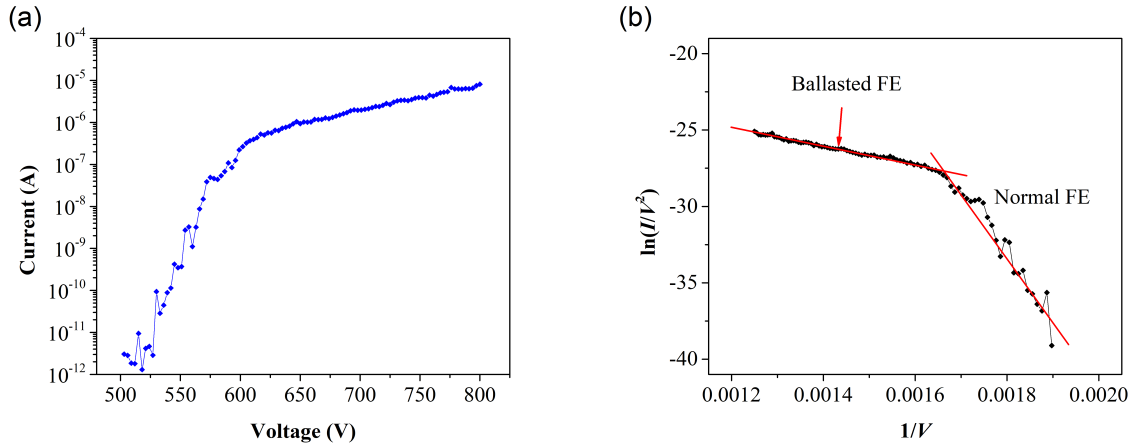

Figure 5.5: FE performance of the 10×10 CNT FEA with individual ballast. (a) Current-voltage characteristics of the CNT FEA with ballast. A FE current of 8.13 μA is achieved at a voltage of 800 V. (b) F-N plot of the FE, in which different FE regions are highlighted.

is a straight line with a negative slope. As the voltage increases above 600 V, the slope of the F-N plots clearly increases, becoming less negative due to the ballast effect of silicon current limiters. The F-N plot indicates that from 500 V to about 600 V FE current from most CNT emitters is below the saturation current of the silicon current limiter. As the voltage increases, current regulation takes effect and some CNT emitters begin to work at the saturation current level causing the F-N plot slope increase.

In practical situations, CNT FEAs should have more CNT field emitters to achieve sufficient current for various applications. Sample 2 is such a CNT FEA (Figure 5.4(f)). It has 8,260 CNT field emitters in a regular octagonal area of 1 mm^2 and an emitter-to-emitter distance of 10 μm. The control voltage sweeps from 500 V to 1,000 V with a step voltage of 5 V. Figure 5.6(a) shows the FE current-voltage curves of the CNT FEA with individually ballast silicon current limiters compared with theoretical prediction without ballast. An overall FE current of 1.03 mA is achieved at a voltage of 1,000 V, which corresponds to 119 nA per emitter. The theoretical prediction is derived from the F-N equation where 8,260 CNT field emitters are working together with the same conditions. Figure 5.6(b) shows the corresponding F-N plot, in which normal FE

and ballasted FE regions are highlighted.

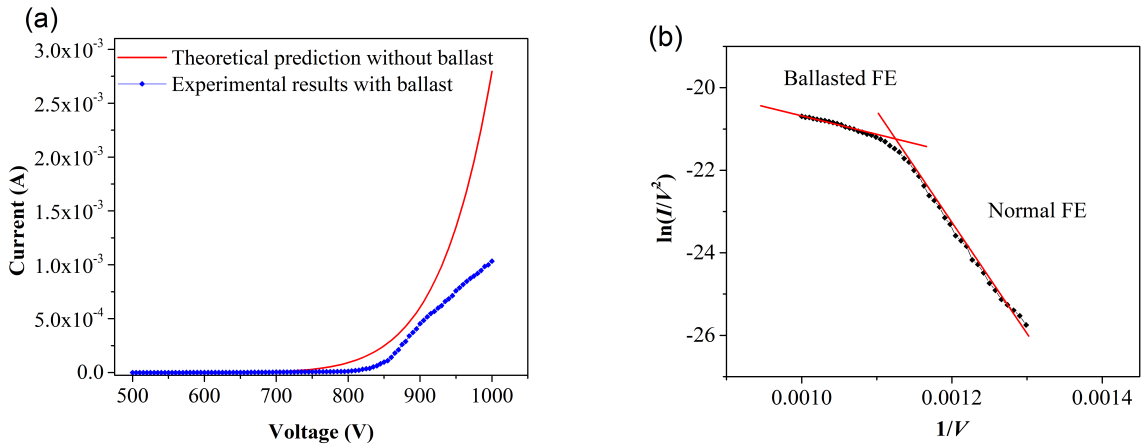

Figure 5.6: FE performance of the CNT FEA with 8,620 CNT emitters with individual ballast. (a) Current-voltage characteristics of the CNT FEA with ballast compared with theoretical prediction of FE without ballast. A FE current of 1.03 mA is achieved at a voltage of 1,000 V. (b) F-N plot of the FE, in which different FE regions are highlighted.

It can be seen from Figure 5.6(a) that the current-voltage curve clearly shows the effect of ballast resistor. It is well known that an ideal FE current-voltage curve should be an exponential-like curve as described by F-N equation. From about 850 V onwards, the current curve tends to become flat instead of increasing exponentially. We believe that as the voltage increases, the FE current of the dominating CNT field emitters reach the saturation current of the corresponding silicon current limiters. As more CNT field emitters are limited, the increase of the overall FE current of the CNT FEA tends to slow down. F-N plot with two linear segments is observed in Figure 5.6(b). The increased slope of the F-N plot indicates the effect of current regulation.

Ideally, FE current all the CNT field emitters will eventually reach the saturation current of the silicon current limiters. As a result, the overall FE current-voltage curve of the CNT FEA should become flatten as the applied voltage keeps increasing. Correspondingly, the slope of the corresponding F-N plot would become positive. In this scenario, only a clear ballast effect but no full saturation of the overall FE current is observed. There are two possible reasons.

One reason is that due to the variation of CNT emitter size and properties within the CNT FEA. Thus, FE performance from each CNT emitter varies. Even under high voltage condition, there exist many CNT field emitters that are still operating below the saturation current level of the silicon current limiters. As the voltage increases, the FE current reaches a plateau but is still increasing gradually. Such an increase is possibly contributed by the increased current from those CNT field emitters operating below the saturation current level. The other possible reason is that Joule heating during the FE operation increases the temperature of the CNT field emitters and the silicon current limiters. The increase in temperature will cause an increase of carrier concentration and thermal velocity. As a result, an increase in temperature results in an increase in saturation current of the silicon current limiter. Simulation results, shown in Figure 5.7, reveals the relationship of the silicon current limiter saturation current and temperature. It can be seen from Figure 5.7 that the saturation current remains nearly unchanged below 500 K. However, when the temperature is higher than 500 K, the saturation current increases significantly. For CNT FEA that is working for a long duration, Joule heating might cause the temperature of the silicon current limiters to go over 500 K. Consequently, the saturation current would be higher than that at room temperature. In this scenario, there could exist CNT field emitters generating FE current lower than the saturation current at an elevated temperature.

The FE performance of each CNT emitter in the CNT FEA is also recorded and visualized using the PMMA thin film based FEM method [129]. Since PMMA is an electron sensitive material, by spin-coating a thin layer (120 nm) of PMMA onto the anode surface, it can visualize the FE current contribution levels from each CNT field emitter based on the morphology of the FEM patterns on the PMMA thin film. For the same period of FE, larger exposed area of the FEM patterns indicates higher FE current from the corresponding FE sites. Besides, it can also record the history of CNT field emitter failure. The detailed description of the PMMA thin film based FEM method to visualize FE performance and emitter failure of CNT FEA can be found in our previous study [129]. Figure 5.8(a) shows the optical microscopic image of the CNT FEA after the FE test. The CNT FEA has 8,260 CNT field emitters in a regular octagonal area of 1 mm^2 and an emitter-to-emitter distance of 10 μm. Despite of the presence of some particles and a fabrication flaw, no CNT field emitter damage can be seen. Figure 5.8(b) shows the optical microscopic image of the FEM patterns of the CNT FEA within the regular octagon

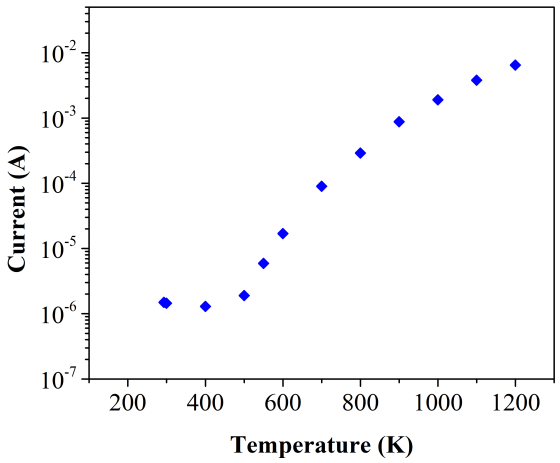

Figure 5.7: The relationship of the saturation current of the silicon current limiter and the temperature.

on the PMMA thin film reflecting the FE performance of each CNT emitters. Low FE current contributions can be seen in Figure 5.8(c).

Figure 5.8(b) shows about 30 FE patterns with large exposed circular area, which even overshadow neighbouring FE sites. These FEM patterns indicate large FE current contributions from corresponding CNT field emitter sites. Medium FE current contributions can also be seen from those bright exposed dots. Besides, FEM patterns of the low FE current contributions, which are not overshadowed by other larger FEM patterns, are also distinguishable in Figure 5.8(c). The PMMA thin film based FEM method reveals that some CNT field emitters are working at a high FE current level while others have very low FE current. Since there is no indication of CNT field emitter failure according to the FEM patterns on the PMMA thin film, it can be concluded that the silicon current limiters effectively protect the CNT field emitters from being damaged and regulate the FE current of the CNT FEA. This result confirms that current regulation is effective in limiting those CNTs with high FE current. It should be noted that there are still many CNT field emitters operating below the saturation current of the silicon current limiters.

The regulation ability of the silicon current limiter allows the CNT FEA to demonstrate good

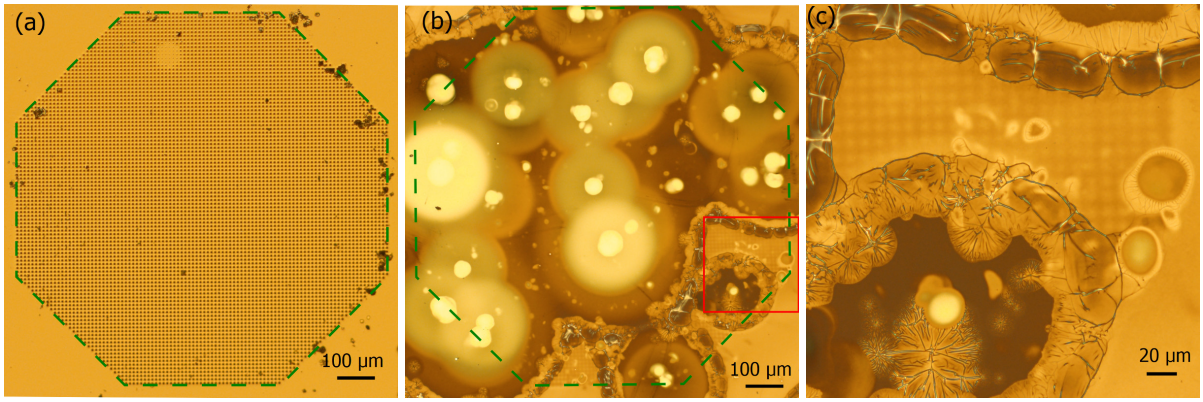

Figure 5.8: The optical microscopic images of the CNT FEA after the FE test and its FE performance visualized by PMMA thin film based FEM method. (a) The optical microscopic image of the CNT FEA after the FE test. Despite of some particles and a fabrication flaw, no CNT field emitter damage can be seen. (b) The optical microscopic image of the FEM patterns of the CNT FEA within the regular octagon on the PMMA thin film reflecting the FE performance of each CNT emitters. Larger exposed area of the FEM pattern indicates higher FE current from the corresponding FE site. (c) The higher magnification optical microscopic image of the FEM pattern of some low FE current contributions highlighted in (b).

repeatability under lower voltage. A comparison is made between a CNT FEA individually in series with the proposed silicon current limiter and a CNT FEA without ballast. Both CNT FEAs have 8,260 CNT field emitters within a regular octagonal area of 1 mm^2 and an emitter-to-emitter distance of 10 μm. A sweep voltage from 0 to 500 V is applied to both the ballasted CNT FEA and the CNT FEA without ballast for six rounds. The step voltage is 5 V. The pico-ammeter records the FE current every step. Figure 5.9(a) and (b) shows the current-voltage curve of the ballasted CNT FEA and the CNT FEA without ballast, respectively. The inserts of the both figures are the F-N plot. There is a slight ballast effect can be seen from the F-N plot of the ballasted CNT FEA.

It can be seen from Figure 5.9 that the repeatability of the FE current-voltage curve of the ballasted CNT FEA is much improved when compared with that of unballasted CNT FEA. The inserts of both Figure 9 (a) and (b) are the F-N plots of each current-voltage curve. An abrupt

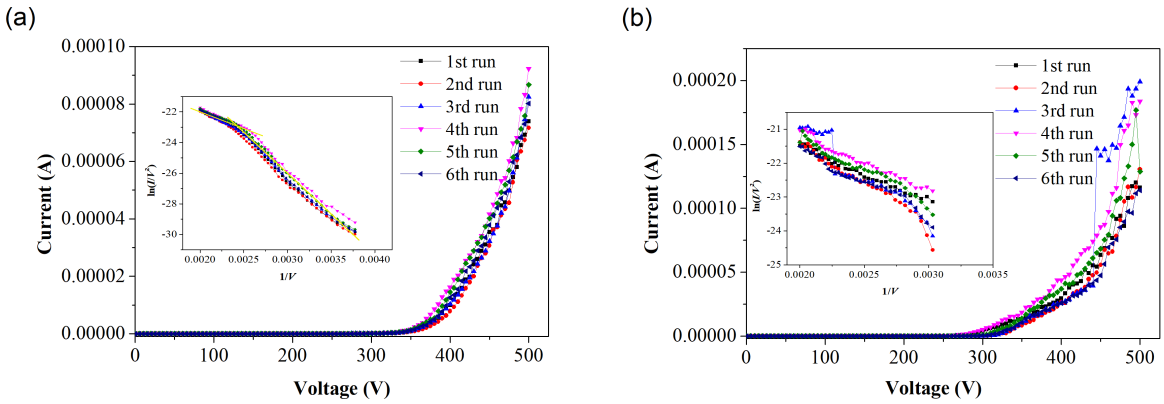

Figure 5.9: FE current repeatability. (a) The current-voltage curve of the CNT FEA individually in series with the silicon current limiters for 6 rounds. (b) The current-voltage curve of the CNT FEA without ballast for 6 rounds. The both inserts are the F-N plot

rise of the FE current from the third round (the blue curve in Figure 5.9(b)) and an abrupt drop of the FE current from the fifth round (the green curve in Figure 5.9(b)) can be clearly seen from the unballasted CNT during the voltage sweep. Based on our previous study on CNT field emitter failure, an abrupt FE current drop may be attributed to an irreversible damage of a CNT field emitter that loses its ability to contribute to the overall FE current [151]. On the other hand, the protective effect of the current limiters eliminates the potentially damaging abrupt current increase of a CNT field emitter. Besides, the better repeatability of the CNT FEA with the silicon current limiter can be clearly seen from the F-N plot inserted. The six F-N plots of the ballasted CNT FEA more densely packed together. Some F-N plots even overlap. The six F-N plots also show a slight trend to become flat, indicating the current regulation effect. While the six F-N plots of the CNT FEA without ballast are loosely distributed.

Figure 5.10 shows the long-term stability test of the CNT FEA with and without current limiter. Figure 5.10(a) shows the FE current varying with time of the ballasted CNT FEA. The FE current is measured under a voltage of 700 V for 1,800 s. The average FE current during this period is 1.16 mA with a maximum FE current of 1.42 mA and a minimum of 0.91 mA. The standard deviation is 0.13 mA, which is 11% of the average. Figure 5.10(b) shows the current-

time curve of the CNT FEA without ballast. The current is measured under 500 V for 600 s. The maximum and minimum FE current are 199.1 μA and 42.5 μA, respectively. The average FE current is 95.1 μA. The standard deviation is 40.0 μA, which is 42% of the average. Although there is a slight decrease of the FE current over time, the stability of the ballasted CNT FEA is greatly improved.

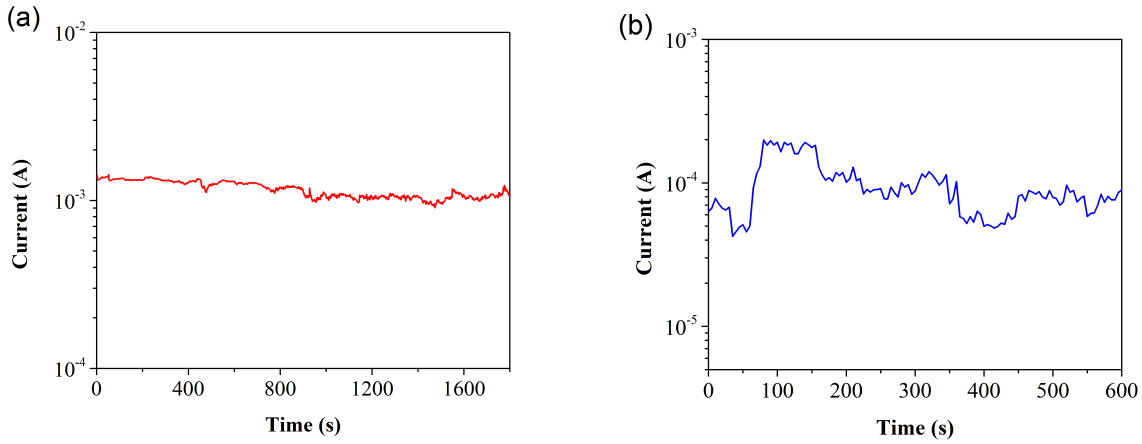

Figure 5.10: The long-term stability test of the CNT FEA with and without the silicon current limiter. (a) The current-time curve of the ballasted CNT FEA under 700 V for 1800 s. (b) The current-time curve of the CNT FEA without ballast under 500 V for 600 s

5.3 Chapter summary

In this study, a comprehensive design and fabrication of individually ballasted CNT FEAs using silicon current limiters is demonstrated. Prior to this study, this approach has been applied on silicon FEAs and CNT clusters employing silicon current limiter but is rarely achieved in individually vertical aligned CNT FEAs. We have successfully fabricated each CNT field emitter in series with a vertical n-type silicon current limiter using two-time nano-scale EBL together with other nano-scale fabrication processes. The designed n-type silicon current limiter has a doping concentration of 1×10^{14} cm^{-3}, a length of 10 μm and a cross section area of 1 μm^2. Due to

the velocity saturation of electrons in silicon, the designed silicon current limiter achieves a saturation current of 1.56 μA to avoid each CNT field emitter over-current and failure. A 10×10 CNT FEA and a CNT FEA with 8.260 CNT emitters in a regular octagonal area of 1 mm^2 and an inter-emitter distance of 10 μm and are fabricated and characterized. Both CNT FEAs show an obvious current limiting effect without losing their sensitivity and efficiency. By exploiting the protective effect of the saturation current, the proposed CNT FEA exhibits improved repeatability and stability. In addition, the temperature effect due to Joule heating on the saturation current is studied. The saturation current remains nearly unchanged below 500 K but increases significantly above 500 K. The systematic design and the successful development of individually ballasted CNT FEAs using silicon current limiter will enable stable and reliable operation of commercially viable CNT FEA as an electron source for applications such as miniature X-ray source and multi-beam X-ray source.

Chapter 6

Self-contained and self-focusing X-ray source based on CNT FEA

Due to its low operating temperature and low power consumption, FE cathode is also suitable for compact and portable X-ray sources, such as security scanning, and on-site NDT applications. Many compact X-ray sources based on CNT FE has been demonstrated [101, 153]. However, considering the non-uniform FE of CNT FE, emission current switching, and electron beam focusing, these X-ray systems rely on complex structure and supporting circuit to operate. Some CNT FE X-ray systems even adopt the tetrode and pentode structures to control and focus the electron beam [154, 155]. These systems are complex and costly. The system complexity, in turn, limits the reliability and the size of the CNT FE based compact X-ray system. Therefore, in contrast to the conventional thermionic emission X-ray sources with simple diode structure and focusing cup, compact X-ray sources based on CNT FE have not been widely applied. As a result, novel applications, which rely on the availability of CNT FE based compact X-ray sources, such as X-ray fluence field modulation, and multi-sources X-ray systems, have developed very slowly.

To resolve the above-mentioned problems of the CNT FE based compact X-ray systems, we have proposed and demonstrated a self-contained and self-focusing compact pulsed X-ray source based on a vertically aligned CNT FEA cathode and a resonant transformer. Based on our previ-

ous studies on CNT emitter failure mechanism [129, 151], FE performance characterization, and magnetic focusing mechanism, we have designed a comprehensive multi-physics model to study the self-focusing electron beam and pulsed mode in the proposed X-ray systems. The model incorporates electronic circuit of resonant transformer, coupling of electric field and magnetic field, and heat transfer. The proposed design has several breakthroughs. First, the integrated resonant transformer is compatible with CNT FEA that are working under a well-designed pulsed mode. Therefore, the accurate control of switching FE "ON" and "OFF" enables the CNT emitters and the target for long-lasting operation under high voltage and high current conditions. Second, high voltage generator is closely integrated with the X-ray components. Since there is no need for extra high voltage insulation components outside the vacuum chamber, the reliability is further improved and the size of the system is further decreased. Third, the electron beam is self-focused by the magnetic field generated by the transformer. As such, no extra focusing components and circuit are needed. Fourth, since the voltage-ampere characteristics of the CNT cathode follows an exponential growth, proper design of the anode-cathode distance guarantees that FE operates only under high voltage. As a result, low energy electrons emission is eliminated. In this chapter, we report design and demonstration of a simple and compact CNT-based FE X-ray system that provides improved X-ray quality and efficiency by accurately adjusting the threshold electric field strength and controlling the width of the high voltage pulse.

6.1 Device design

The system consists of (i) a high-frequency full bridge drive circuit; (ii) a stack of parallel connected pancake coil as the primary coil; (iii) a stack of series connected pancake coil as a secondary coil; (iv) a coupling circuit using a high voltage diode and capacitor to connect the CNT FE cathode and the anode to the transformer; (v) a vertically aligned CNT FEA that is connected to the negative voltage; and (vi) a tungsten rod as the target connected to the positive voltage. The entire system is highly compacted with no more than 8 cm in length. Only a 12 V DC power and a trigger signal are needed to operate pulsed X-ray generation. Figure 6.1 shows the system structure diagram. Figure 6.1(a) shows the schematic of the system operation. Figure 6.1(b)

shows the cross-section diagram of the proposed compact X-ray source. Figure 6.1(c) shows the picture of the compact X-ray source.

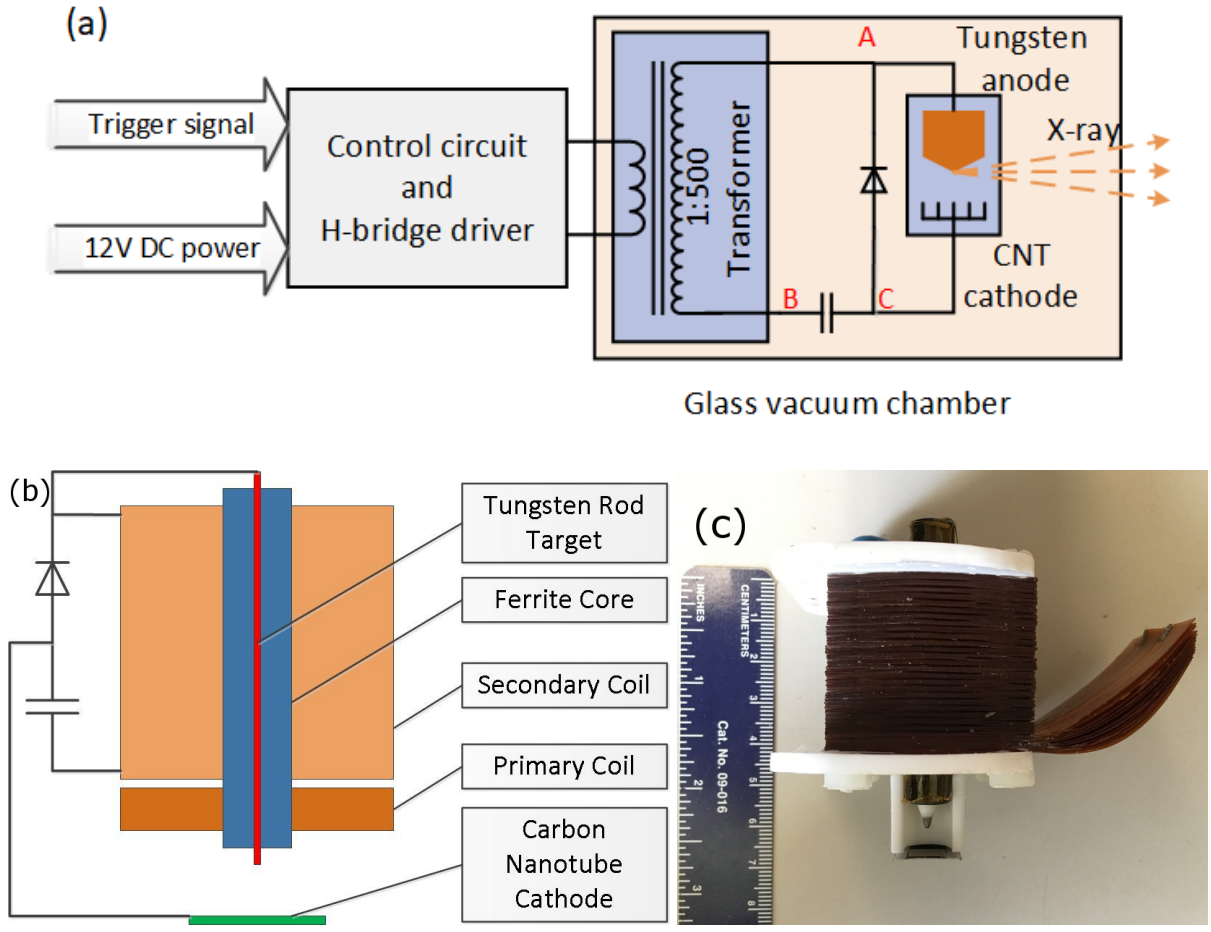

Figure 6.1: Diagram of the system structure: (a) system schematic, (b) cross-section diagram of the proposed compact X-ray source, and (c) the photo of the compact X-ray source.

The control circuit generates a square wave signal with a fundamental frequency equal to the resonant frequency of the transformer. The trigger signal defines the period of the square wave thus determines the width of the X-ray pulse. The H-bridge driver amplifies the square-wave and provides a high-current high-frequency square wave on the primary winding of the transformer. High-voltage is then generated on the secondary winding of the transformer. The turn ratio of

the transformer is 1:500. Generally, the voltage gain of a transformer equals the turn ratio. To increase the voltage gain, we make the transformer work at its peak of the resonant frequency. Therefore, the voltage gain is the product of the turn ratio and Q factor of the transformer. The output of the transformer is connected to the X-ray components with a coupling circuit consist of a capacitor and a diode. A high-voltage diode is reversely parallel connected to the X-ray components. In the negative half cycle of the square wave, when the electric potential of point A (V_a) (shown in Figure 6.1(a)) is lower than the potential of point B (V_b), the X-ray component is reversely biased. The capacitor is charged through the diode. In the positive half cycle, the voltage applied on the X-ray components equals the transformer output (V_{ab}) plus the potential difference of the capacitor (V_{bc}). The applied voltage keeps increasing. When the threshold voltage of the X-ray component is reached, FE starts to operate. Since the FE current increases exponentially with the increase of the applied voltage, the maximum FE current of the CNT could be much larger than the maximum output current of the transformer. However, when the CNT FE current reaches the maximum output current of the transformer, the voltage applied on the X-ray components (V_{ac}) will stop increasing. Consequently, over-current of the cathode is avoided. By adjusting the cathode-anode distance, the threshold field strength and the minimum electron energy can be determined. On the other hand, the adjustment of the maximum electron energy is a little trickier. The maximum power of the transformer, the capacitance of the capacitor, and the FE property of the CNT cathode need to be taken into account.

The CNT FEA cathode consists of vertically aligned CNT field emitters with an inter-emitter distance of 10 μm. The CNT FEA is fabricated using the same process as discussed in the previous chapters. Figure 6.2(a) and (b) shows SEM images of the CNT FEA and a single CNT field emitter from the array, respectively.

During an FE process, Joule heating converts FE to extended Schottky emission and lead to a further increase of the FE current [151, 156]. This positive feedback process will cause a thermal runaway and eventually lead to Coulomb explosion that destroys the CNT field emitters [151]. To avoid the CNT field emitter failure, a rectified high voltage pulse is applied onto the X-ray components directly to reduce the duty cycle of the FE and promote heat dissipation from CNT emitters. Using puled mode in CNT FE based X-ray sources is a significant difference from conventional thermionic based X-ray sources. In a conventional X-ray source, when the filament

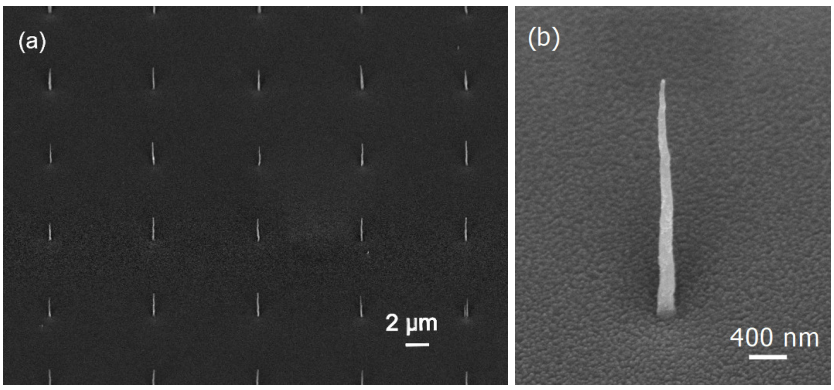

Figure 6.2: The SEM image of the vertically aligned CNT FEA as the cathode. (a) The CNT FEA. (b) A higher magnification SEM image of a single CNT field emitter.

is heated up, an electron cloud is generated around the filament. Electrons will be attracted to the anode even when a low voltage applied to the anode. As a result, many low energy photons and extra heat will be generated if a rectified high-voltage AC power is applied to the conventional X-ray source, and thereby reducing tube efficiency and lifespan. To overcome this issue, conventional X-ray generator uses big capacitors to get a constant high voltage. In this CNT FE based compact X-ray source, electrons are emitted only when the threshold field strength is reached. Therefore, there are few low energy electrons generated. This rectified high voltage pulse not only eliminates the low energy X-ray and avoid of CNT emitter failure, but also simplifies the circuit and significantly reduces the weight and cost of the X-ray system. Besides, the pulse mode allows rapid thermal dissipation on both the CNT FEA and the anode. Therefore, longer and more stable operation of the X-ray system can be expected.

The X-ray source is simulated with different methods. The high voltage circuit is simulated by the Simulation Program with Integrated Circuit Emphasis (SPICE) software. The magnetic field of the transformer and electric field of the X-ray components is modelled and simulated by COMSOL Multiphysics based on finite element method.

The high voltage circuit, including the H-bridge, transformer, coupling circuit, and the CNT FEA cathode, is simulated using a SPICE software. Since the characteristic of the CNT FE is similar to that of a diode, we use a four-segment piecewise linear model to simulate the CNT FE

based X-ray system. The voltage-ampere characteristics of the CNT FEA cathode is characterized by experiments. A PWL model can fit well with the voltage-ampere (I/V) curve. Figure 6.3(a) shows the simulated current curve and the experimental results. Both the voltage-ampere curves and the F-N plots have a good agreement with the experiment results. Figure 6.3(b) shows the simulation result of voltage and current across the X-ray components. In Figure 6.3(b), in the negative half cycles ($V_a < V_b$) of the first several cycles, the high-voltage capacitor is charged through the diode. The cathode and the anode are reversely biased. there is no FE within the negative half cycle. In the positive half cycles ($V_a > V_b$) of the first several cycles, since the voltage applied on the X-ray components (V_{ac}) does not reach its threshold voltage, no current pass through the capacitor and the voltage on the capacitor (V_{bc}) keeps unchanged. This charging process takes few microseconds (several cycles before T_a in Figure 6.3(b)). Then, a very small current is emitted from the CNT cathode in the positive half cycles (between T_a and T_b in Figure 6.3(b)). Since the emission current is lower than the output current of the transformer, the V_{ac} keeps increasing. The duration of this process is determined by the capacitance and the inner resistance of the transformer. The FE current does not show a clear increase until the time point T_b. Therefore, the power consumption and radiation dose generated at the low voltage is negligible. After T_b, the applied voltage reaches the threshold voltage of the CNT cathode. The tube current (CNT FE current) and the voltage becomes stable with small increase.

Sine electron focal spot size determines the resolution of an X-ray source, electron focusing should be considered. In this case, the electron trajectories is determined by both the electric field and the magnetic field. Thus, the X-ray components and the transformer is modelled using finite element method. First, the electric field and the magnetic fields strength distribution are simulated. Figure 6.4 shows the simulation of the electric field and magnetic field distribution. The CNT FEA is synthesized on a silicon substrate with a diameter of 6 mm. A round plate is used to represent the CNT FEA cathode in the simulation. The anode is modelled as a 2 mm diameter cylinder. The model consists of a cylindrical ferromagnetic core. The cylindrical anode warped by the ferromagnetic core is placed at the center of the primary and secondary coils. As the electron flying time is much shorter than the cycle of the square wave, the magnetic field and electric field is simulated in steady-state mode. Both circuit and magnetic field models are coupled to calculate the electric field and magnetic field distribution. The model is enclosed a

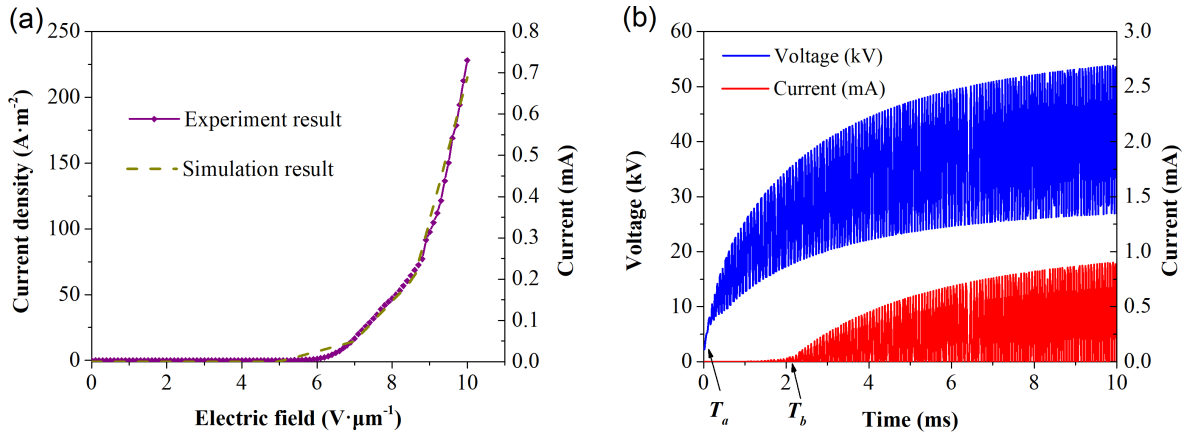

Figure 6.3: (a) Experimental and simulation FE current density versus the applied electric field of the CNT FEA. (b) the voltage response and corresponding FE current in the first 10 ms.

spherical space with an infinity boundary, such that the effects from the simulation boundary is minimized. Figure 6.4 shows the simulation results of the electric field and the magnetic field. In Figure 6.4(a), the color bar represents the voltage gradient. The red area is the X-ray anode connected to the high voltage, while the blue area is low voltage area of the cathode and transformer. In Figure 6.4(a), the electric field lines closed to the cathode (below the yellow arrow in the insert of Figure 6.4(a)) are divergent, which affects the electron beam focusing, thus reduce the X-ray image resolution. Figure 6.4(b) shows the magnetic field distribution. The primary winding has higher current than the secondary winding, so it was put close to the cathode to provide high magnetic field. The magnetic field lines are closed loops that go into the core from one end and exit from the other end. The magnetic flux density in the core are much higher than that of the other places in the magnetic field. The magnetic flux density convergence at both ends of the core.

Next, a charged particle tracking model is integrated to simulate the electron beam trajectory under the electromagnetic force. Figure 6.5 shows the simulation results. The cylindrical shape target is placed at the centre of the core, where the magnetic flux has the highest density. The cathode is placed 10 mm away from the core, where the magnetic flux density is much lower

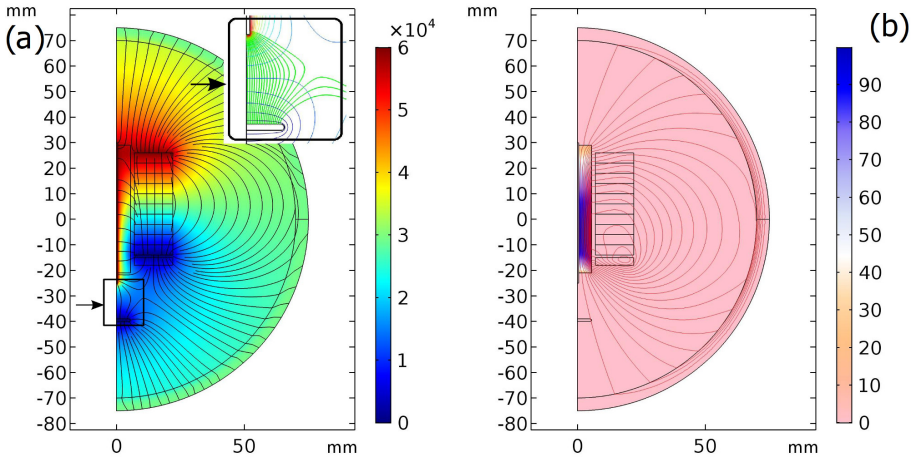

Figure 6.4: Simulation results of (a) the electric field distribution and (b) the magnetic field distribution. The insert of (a) shows the electric field lines close to the cathode are divergent, which is unable to focus the electron beam to the anode tip.

than that of the core. Then the trajectory of the electrons emitted from the CNT FEA cathode is computed. This model is solved in transient state to calculate the focal spot size. When electrons tunnelled through the potential barrier of a CNT field emitter, the full width at half maximum of the distribution of total kinetic energy is $0.693\varphi \approx 3.3$ eV [157], where $\varphi(= 5$ eV$)$ is the work function of CNT [158]. This kinetic energy corresponds to an initial electron velocity of 1.08×10^6 m $\cdot$ s^{-1} in all directions. The velocity is the initial speed with random directions in the electron trajectory model. Figure 6.5(a) and (b) show the electron trajectory without and with the magnetic field, respectively. In Figure 6.5(a), only the electric field is applied to extract electron from the cathode and accelerate the electrons to hit the target. The travelling time of the electron is about 0.5 ns. The beam is divergent follow the electric field line in the first 0.35 ns, because the electron velocity is relatively low. From 0.35 ns onwards, the electrons arrive into the area where the electric field line starts to concentrate (the insert of Figure 6.4(a)). The horizontal component of the electric force starts to focus the electrons. However, at this point, the vertical component of the electron velocity is much larger than the horizontal component. As a result, the electron beam cannot be focused to the target tip with only electric field. As is shown in Figure 6.5(b), when a magnetic field is applied, the electron trajectories are helical. The

centrelines of the helices are the magnetic force line. The gyro-radius is defined by $r = mv/qB$, where m is electron mass; v is electron velocity; q is electron charge; and B is the magnetic field strength. Since the magnetic flux density is much higher at the target tip, the gyro-radius of the helices decreases significantly. As a result, the electron beam is well focused at the target tip. Therefore, our system is able to achieve electron beam self-focusing utilizing the magnetic flux of the transformer at the core opening.

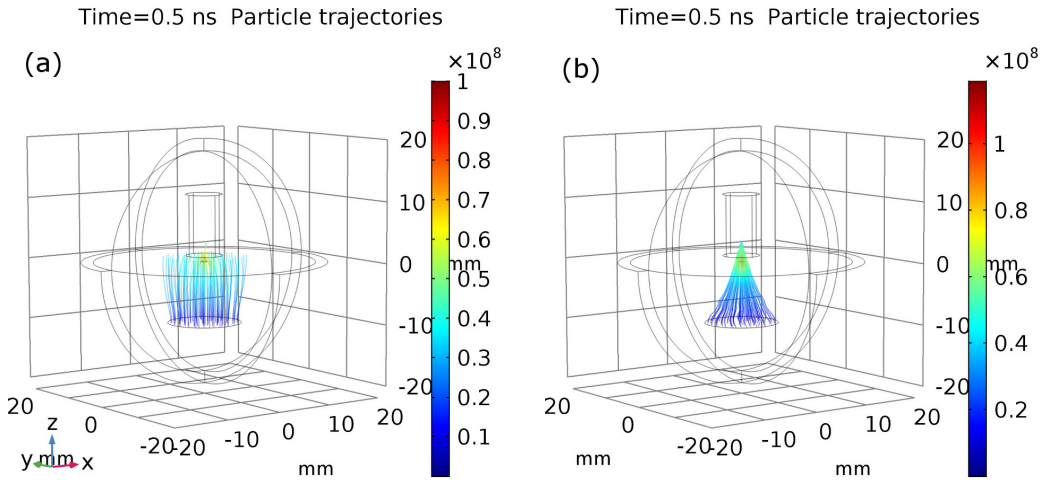

Figure 6.5: Simulation results of the electron trajectories without (a) and with (b) magnetic field.

6.2 Device demonstration and discussions

The X-ray source design involves many physical quantities, such as high voltage, electric field strength, FE current, electron trajectory, and all these quantities are tightly coupled. These coupling makes the performance characterization complex. To characterize the system, we measured the property of each component separately. Then, we integrate the system and test the overall performance of the entire system.

First, we figure out the resonance frequency of the high-voltage transformer. The transformer

is built according to the above-mentioned design. The external diameter of the coils is 1.5 inch (38.10 mm) and the inner diameter is 0.4 inch (10.16 mm). The primary coil has 5 turns and the secondary coil has 2,500 turns. A low voltage step is applied on the primary winding of the transformer. The spectrum of the output form the secondary winding is recorded with an oscilloscope. The input step signal is considered an excitation signal with infinity bandwidth. The highest peaks of the spectrum output signal indicated the resonance frequency of the transformer. The resonance frequency of the transformer is 72 kHz, and the 3 dB bandwidth is about 7 kHz. Then, a 12 V 72 kHz high-current square wave is applied on the transformer. The output high voltage is approximated by measuring the electric arc length in air between two needle electrodes [159]. The electric arc length generated by the resonant transformer is 6 cm. The 6 cm electric arc in air requires 50 kV to breakdown the air gap, therefore the maximum output voltage of the transformer is estimated to be 50 kV. This result has a good agreement with the simulation result shown in Figure 6.3(b). The voltage gain is $50\text{kV}/12\text{V} \approx 4167$, thus the corresponding Q factor of the transformer is 8.3.

Next, to characterize the FE property of the CNT FEA cathode, a pulsed voltage is applied to find out the maximum current of the CNT FEA cathode. To avoid the delay of the high-voltage circuit switching, the pulsed FE current is measured under a low voltage with a small cathode-anode gap. Figure 6.6 shows the FE current under an electric field of 16 $\text{V} \cdot \mu\text{m}^{-1}$ and a pulse width of 1.1 ms. An average FE current about 250 mA is achieved from the 8,700 CNT field emitters. It can be seen from the Figure 6.6 that there is a spike at the beginning of each pulse. We believe it is caused by the parasitic capacitance of the circuit and wires instead of the FE current. The average FE current from each CNT field emitter is about 30 μA. This value has a good agreement with the maximum FE current that a single CNT can withstand for tens of milliseconds [13]. The 250 mA pulsed FE current is much higher than the maximum output current of the transformer, therefore the transformer can avoid of the CNT burned by over-current.

The electric field to start FE from the CNT FEA is a function of the anode voltage and the cathode-anode gap. Since the anode voltage determines the X-ray energy and FE operation at the same time, a suitable cathode-anode gap needs to be found out to eliminate low energy X-rays. Simulation results shown in Figure 6.3(b) indicates that when the cathode starts to emit

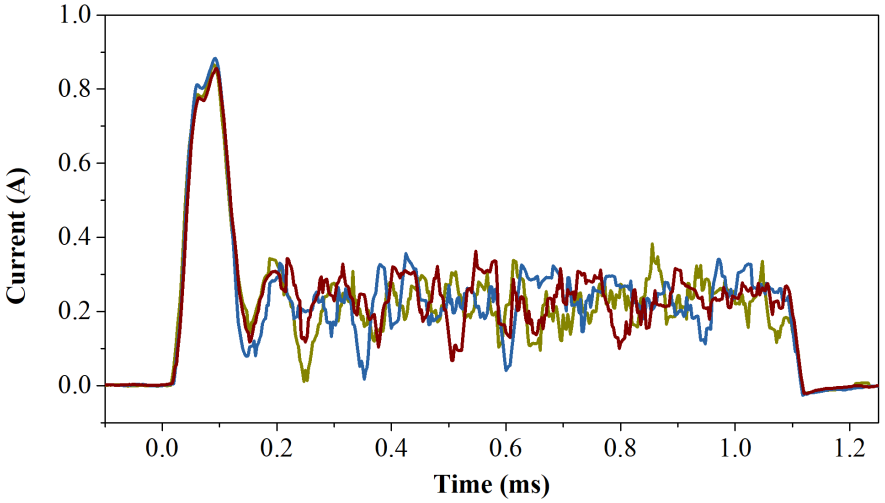

Figure 6.6: FE current of the CNT FEA under a 1.1 ms wide 16 $V \cdot m^{-1}$ electric field pulse. The effective FE current is about 250 mA.

electrons, the capacitor starts to discharge, as a result, the voltage will have a fluctuation range from 27 kV to 51 kV. We use a constant voltage of 35 kV constant high-voltage (2/3 of the 50 kV maximum transformer output voltage) to determine the cathode-anode gap. According to the voltage-ampere characteristics of the CNT FEA cathode shown in Figure 6.3(a), the FE starts to turn on at an electric field of 5 $V \cdot \mu m^{-1}$. Therefore, the cathode-anode gap is set to 7 mm, corresponding to a threshold voltage of 35 kV.

Finally, the transformer, the X-ray cathode, and the anode are integrated and put into a vacuum chamber at a base pressure of 2×10^{-8} Torr. The anode is a 2 mm diameter tungsten rod wrapped within an insulation film. The cathode is a vertically aligned CNT FEA synthesized on a silicon substrate. The CNT FEA is placed 7 mm away from the anode tip. All the components are made with vacuum friendly materials. Ceramic is the ideal materials for the X-ray tube. However, to simplify the fabrication process, polyimide and polytetrafluoroethylene are used as insulators. A high current square wave is generated by a micro-controller and an H-bridge circuit. The square wave lasts for 100 ms. A Geiger-Muller counter is used to measure the X-ray

radiation intensity. Figure 6.7 shows the X-ray intensity distribution. We measured 35 pulses and the radiation exposure of each pulse ranges from 40 to 100 $\mathrm{mR \cdot hr^{-1}}$.

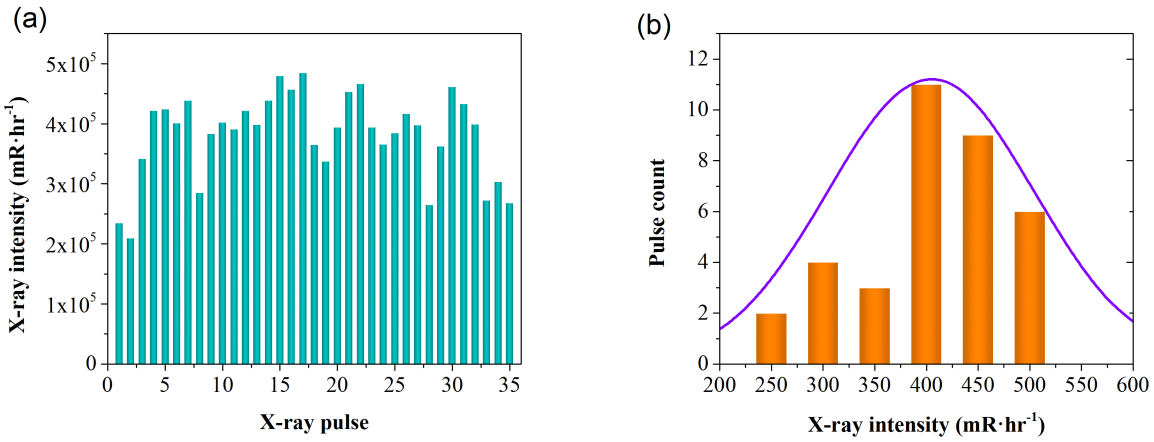

Figure 6.7: (a) The X-ray intensity of each pulse. (b) The intensity distribution and the normal distribution curve.

Figure 6.8(a) and (b) show the optical image and the X-ray image of an industrial relay, respectively. Figure 6.8(c) shows the high magnification X-ray image. All the details of the edge of via holes of the circuit board and the armature of the relay are clearly seen. Since the size of via holes and armature is a few tenths millimetre, the image resolution is good enough for sub-millimetre scale imaging.

In this design, the gap between the cathode and the anode determines the beam energy. Further studies of the voltage-current characteristics of the CNT FEA cathode under a pulsed high voltage of different anode-cathode distance is needed to determine the peak energy of the X-ray beam. This will help us design X-ray sources to meet the requirements of different applications. The experiments demonstrate the high voltage circuit based on the resonant transformer has the capability of driving an CNT FE based compact X-ray source. The geometry parameter and the materials of the windings can be further optimized to improve the transformer performances. By increasing the wire cross-section diameter, the resistance of the windings is decreased. The Q factor of the winding and the output voltage of the transformer will also be increased signif-

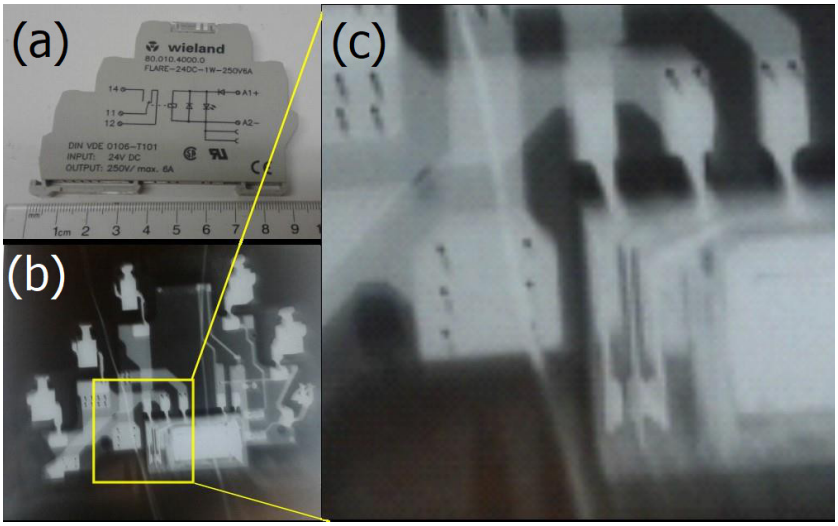

Figure 6.8: X-ray image of a relay. (a) The optical image of the relay. (b) The X-ray image of the relay taken by the proposed compact X-ray source. (c) The high magnification X-ray image of the relay. The object consists of a copper connector, a copper foil circuit board, and a solenoid.

icantly. As such, the X-ray source can be further decreased in size while increased in X-ray beam energy. Furthermore, with more components integrated into the vacuum chamber, vacuum pumping down is a challenge.

6.3 Chapter summary

In the paper, an integrated pulsed X-ray source based on a resonant transformer and a CNT FEA cathode is designed and demonstrated. By integrating a resonant transformer, the X-ray source can be powered by a 12 V DC power supply. The X-ray source is able to generate pulsed X-ray beam. The exposure dose test indicates that the X-ray beam has good repeatability and reliability. Meanwhile, self-focusing of the electron beam has successfully achieved by the magnetic field generated by the resonant transformer. Benefiting from the integrated high voltage and electron beam focusing mechanisms, high resolution X-ray images taken by the proposed X-ray source show a sub-millimetre scale resolution. The proposed integrated pulsed X-ray source has a highly

simplified structure which can not only increase reliability but also reduce the cost of the device significantly. The compact size and low cost makes it suitable for potential applications that need multiple X-ray sources.

Chapter 7

X-ray fluence field modulation based on CNT FEA

The idea behind the traditional X-ray fluence field modulation is to use an extra tool to either shape a filter to selectively attenuate a cone X-ray beam or dynamically vary an aperture to adjust exposure time. Contrary to the fixed filtration patterns in conventional use, FE from CNTs used as electrons source in X-ray system are able to achieve fast "ON" and "OFF" of any X-ray source and control of X-ray exposure timing. X-ray image dose adjustments, fluence field modulation, and shape variation can be achieved by the fast response and addressable CNT FEA. As a result, a heavy and inflexible filter or collimator can be eliminated. Since CNT FEA is small in size and can be patterned into two dimensional array, a flat panel multi-beam X-ray source based on CNT FEA is able to allow spatially varying, user-prescribed X-rays but "as low as reasonably achievable" radiation exposure to limit unnecessary dose and cancer risk to patients without sacrificing image quality with limited dose. Such X-rays can benefit many cases when high image quality near the suspicious lesion is only desired such as locating the tip of a surgical instrument with respect to an anatomical landmark and a repeat diagnostic CT scan to explore a suspicious anomaly.

7.1 System architecture and control method

A novel 2D multi-pixel X-ray source is proposed for FFMCT, shown in Figure 7.1. Ideally, parallel X-ray beams are generated from multiple X-ray pixels (Figure 7.1(a)). Each pixel can be individually controlled and addressed, making it possible for irregular field shaping and spatial modulation of the X-ray intensity as needed. The device operates by controlling the gate voltage of the each pixel of the CNT FEA cathode to allow beam shaping and fluence field modulation. The X-ray fluence field shape is formed by selectively turning on individually controllable X-ray pixel beams as opposed to using a cone beam that is mechanically collimated to a given shape. The X-ray beam intensity can be modulated by setting a corresponding gated voltage and a proper duty cycle of FE. The FE electron beams are focused with the focusing electrodes and accelerated to the anode along the high electric field to generate X-ray beams. In our design, X-rays generated in the reflection mode (anode angle is 0°) will be formed into parallel beams by properly designed collimation. Without the collimator, each cell can still work as a multi-pixel cone beam X-ray source, which can be potentially applied for IGRT.

In practical situations, however, even if there is a perfect pencil beam achievable, the gap between neighbouring pixels will lead to incomplete coverage of region of interest. Besides, X-ray beams generated are all cone-shaped beams. Albeit there is a well-designed collimator applied, neighbouring X-ray beam overlapping occurs. A practical flat panel multi-pixel X-ray source is desired to have the capability to irradiate all the without missing any portion, while image overlapped of the adjacent pixel does not affect the image quality. To resolve the above-mentioned challenges, a four-point rotation scanning method is designed. Figure 7.1(b) and (c) illustrates the diagram of the approach. We define the plane that adjacent beams intersect as a top plane and the plane that alternation beams intersect as the bottom plane. The space between the two planes can be fully covered by X-ray beams. Above the top plane, the object is not fully covered by X-ray beam; while below the bottom, the image overlap will lead to image blurry. The neighbouring pixels are activated alternatively. The pixels are divided into four groups and launched one by one. Each X-ray image needs four exposures. A reconstruction algorithm is needed to build up the image and some sort of depth information will be generated.

To generate X-ray beams from 2D source array, we choose to use reflection anode structure.

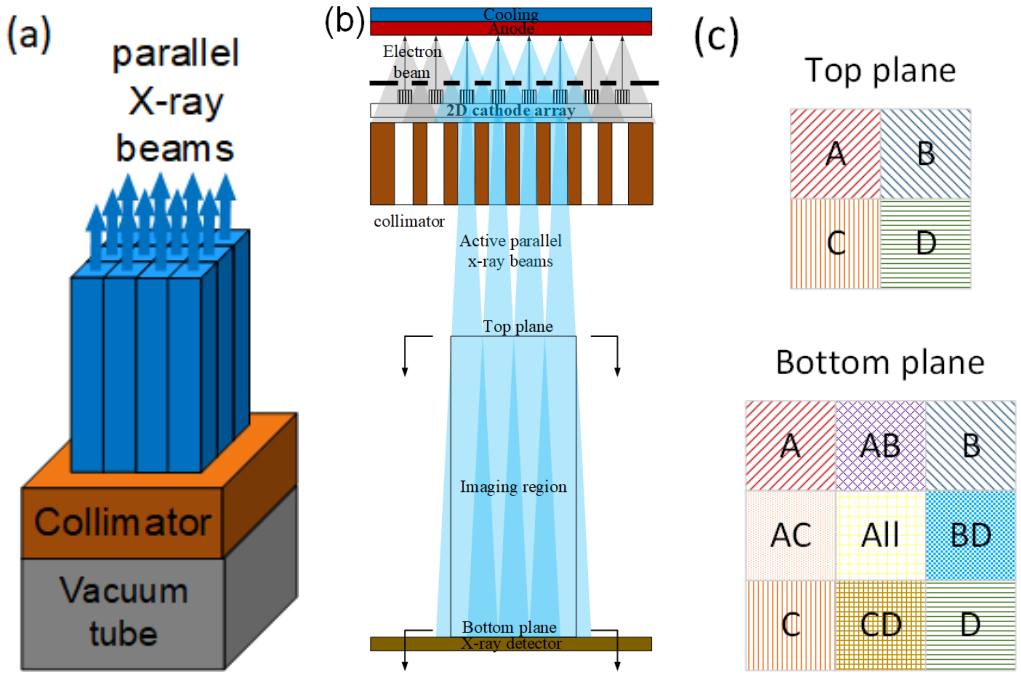

Figure 7.1: Diagram of the 2D multi-pixel X-ray source for FFMCT: (a) illustration of 2D multi-pixel X-ray source with parallel X-ray beams, (b) the schematic of a cross-sectional view of the multi-pixel X-ray source, and (c) the diagram of the scanning method.

In this mode, X-ray photons emit in the opposite direction to the incident electron beam. An alternative mode is to use a transmission anode, where X-ray photons are generated in the same direction as the incident electron beam. The anode has to be made very thin (tens of microns) to allow X-ray transmit through the anode material. Although transmission mode can avoid heel effect and has less cross-talk among multiple X-ray beam, it suffers from inadequate heat dissipation of the anode due to very thin target, resulting in short cathode life due to back-ion bombardment caused by the lower vacuum that ensued from the anode melting and out-gassing. Another problem for transmission mode is the limited anode voltage range. Different anode voltage will have different electron depth in the target. However, the thickness of the target is fixed for a specific anode voltage. Larger acceleration voltage will lead to electron beam penetration. While smaller acceleration voltage lead to shallow electron beam in the target,

resulting in attenuation of X-ray produced. Both situation will have lower X-ray generation efficiency. Our reflection mode can solve anode melting problem since thicker anode can resist higher heat load and avoid heel effect due to symmetrical X-ray emission.

To achieve accurate and efficient control of FE from CNT FEA, a gate electrode is required. Most existing CNT FE cathodes employ a separated gate electrode to control the FE since it is simple and convenient. However, separated gated electrodes lead to a large cathode-gate gap and thus a very high control voltage to extract electrons from CNT FE cathodes. For multi-pixel X-ray sources, high control voltage makes it harder to allow fast current adjusting of an individual pixel. Therefore, a low control voltage is desired to improve the sensitivity of multi-pixel X-ray sources. To achieve it, a well-controlled smaller emitter-gate gap is needed. Our group previously proposed a CNT FEA with coaxial cylinder gate cathode, which is able to have well controlled emitter-gate gap within hundreds of nanometres or several microns and very low gate voltage. The detailed fabrication process of the CNT FEA with coaxial cylinder gate cathode is presented in the section 2.2.2.

The FE performance of the CNT FEA with coaxial cylinder gate cathode has been well studied else where [10]. The average FE current is about 550 μA from 2121 CNT field emitters within an octagon area of 0.2 mm^2 under a gate voltage of 40 V, corresponding to 0.26 μA from a single emitter. The CNT FEA also exhibits good long term stability. The key feature of such type of CNT FEA design is that the control voltage for electron emission is greatly decreased. The sample has an emitter-gate gap of about 300 nm. Compare to the mesh gate of thin film emitters, which has a gate-emitter gap of over hundreds of microns and gate voltage over one thousand volts, the integrated gate electrode has much lower control voltage. As a result, the FE emission sensitivity is greatly improved. Besides, small control voltage is able to simplify and minimize the control circuit of the device significantly.

7.2 Structure design

A whole process of producing X-rays includes electron emission, focusing and accelerating electron beams, decelerating high energy electrons by target, and X-rays emission. In the process,

electron beam focusing determines the resolution of X-ray images; anode heat load determines the maximum power of an X-ray source; for our multi-pixel X-ray source, pixel configuration and collimator determines the X-ray profile and intensity distribution. Therefore, a proper design of the multi-pixel X-ray source is necessary.

7.2.1 Electron beam focusing investigation

Spatial resolution of an X-ray image depends primarily on the focal spot size of the electron beam on the anode target, the pixel pitch of the detector, and the imaging geometry. By choosing the optimum geometry magnification and given the pixel pitch of current detector technology, the spatial resolution is limited by the X-ray focal spot size. Thus, reducing the focal spot size is essential for achieving high resolution of X-ray imaging. The X-ray focal spot depend entirely on the focusing of the electron beam impinging on the anode. Either magnetic lenses or electrostatic lenses are used to focus the electron beam. Magnetic lenses offer lower aberrations and better focusing properties, which are widely applied in SEM and TEM. However, the magnetic focusing unit is usually large and requires complex power control unit. In contrast, electrostatic focusing only requires simple metal electrodes, which is effective and small.

In a conventional X-ray source, a negatively charged focusing cup containing the filament is used as the focusing electrode. However, the focusing cup approach consumes large space which will not be suitable for our multi-pixel X-ray source. In most X-ray source using CNT field emitter cathode, an independent focusing unit is used. For, example, Zhang et al chose a metal plane diaphragm as a single focusing electrode with an inner diameter of 3 mm, achieving a focal spot with a diameter of 250 μm for a CNT film cathode of 1 mm in diameter [104]. Choi et al used a double focusing electrode unit with inner diameter of 3 mm over a MWNT film cathode with a 5 mm in diameter. The focal spot diameter achieved is less than 1 mm [92]. Here we propose a detailed study on designing a single electrostatic focusing electrode for CNT FE based X-ray source using numerical simulation.

The model of the CNT FE based X-ray source studied comprises a FE cathode, a focusing electrode, and an anode housed in a vacuum chamber. Figure 7.2(a) schematically shows the cross-section view of the model system. Electrons are initially extracted from the CNT FEA

Table 7.1: Parameters that affect the focal spot size.

V_a (kV)	V_f (V)	D_{ac} (mm)	D_{cf} (mm)	d_f (mm)	h_f (mm)	l_c (mm)
40	500	10	3	6	5	1

cathode by the gate electrode (the voltage is V_g) and then focused by the focusing voltage (V_f) before reaching the high-voltage (V_a) anode for X-rays generation. A single focusing electrode, which is made of a piece of metal with a channel, was used in the current as focusing electrode. The X-ray focal spot size is determined by adjusting the focusing electrode voltage and the various geometrical parameters as illustrated in Figure 7.2(a). D_{ac} is the distance between the anode and the cathode; D_{cf} is the distance between the cathode and the focusing electrode; d_f is the diameter of the focusing electrode channel; h_f is the thickness of the focusing electrode; l_c is the square-shape cathode side length.

The relation between the X-ray focal spot size and the respective geometrical parameters is studied by the commercial finite element software COMSOL Multiphysics. Table 7.1 lists the parameters that potentially affect the electron trajectories. Figure 7.2(b) shows electron trajectory simulated with the same parameters shown in Table 7.1. The electron emission area in the simulation is the same as the designed CNT FE cathode, which is 1 mm^2. The electron crossover position on the cathode-anode axis just impinges on the anode surface generating an X-ray focal spot of a minimum diameter. Figure 7.2(c) shows the corresponding simulated focal spot of about 140 μm.

In order to pursue an optimum geometry for designing the X-ray source, individual factors in relation to the focal spot size are studied. The variation of the focusing voltage is to keep the electron focal spot is right on the anode surface without over or under focusing. Figure 7.3(a) shows that the focal spot size is proportional to the anode-cathode distance. The scale coefficient is 19.5 $\mu m \cdot mm^{-1}$ between 10 mm and 20 mm. It indicates that decreasing the distance between the anode and the cathode is able to reduce the focal spot size. The focal spot size is 140 μm at 10 mm anode-cathode distance and 340 μm at 20 mm anode-cathode distance, respectively. The focusing voltage is decreasing with the increase of the anode-cathode size. Figure 7.3(b)

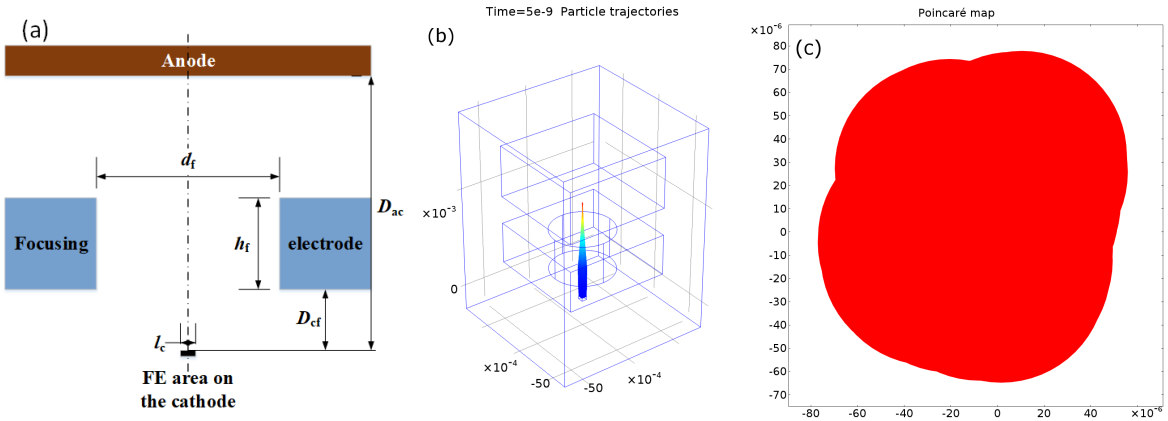

Figure 7.2: (a) Cross section view of the simulation model; (b) The simulated electron trajectory; (c) The simulated focal spot size on the anode, which is 140 μm.

shows that the focal spot size decreases as the distance between the cathode and the focusing electrode increases. The absolute value of focusing voltage increase as well to guarantee the electron beam is perfectly focused. Figure 7.3(c) indicates that increasing the focusing electrode thickness is able to decrease the focal spot size. The X-ray focal spot diameter decreases in a non-linear way relative to the increase of focusing electrode thickness. The effect of increasing the focusing electrode thickness on focal spot size is similar to that of increasing the distance between the cathode and the focusing electrode. The similarity is due to the outlet of the focusing electrode is closer to the anode in both cases. Figure 7.3(d) shows that the focal spot size almost does not change with the increase of the diameter of the focusing electrode. As the diameter increases, the symmetrical axis of the electron beam is farther away from the focusing electrode, higher focusing voltage is needed to maintain the electron beam focused on the anode surface. Therefore, the focusing voltage has approximately liner relationship with the diameter. Figure 7.3(e) shows the variation of the focal spot size with respect to the CNT FEA cathode size. The result reveals a very linear relationship between the focal spot size and the CNT FEA cathode size ranging from 0.2 to 2.0 mm. The focusing voltage is proportional to CNT FEA size as well. Therefore, decreasing the cathode dimension provides an alternative way of reducing the focal spot size. The variation of the focal spot size in related to the anode voltage is shown in Figure

7.3(e). The anode voltage has a slight impact on focal spots size as the focusing voltage increases linearly. In sum, a focal spot size as small as 140 μm can be achieved under the conditions shown in Table 7.1. The simulation study on electron beam focusing indicates that one focusing electrode and proper focusing voltage in CNT FE based X-ray tube is able to focus electron beam in a desired focal spot size. It can be concluded that a small anode-cathode distance, relatively large distance between the cathode and the focusing electrode, and reduced FE size are able reduce X-ray tube focal spot size. Smaller focusing aperture size and lower anode voltage result in lower focusing voltage.

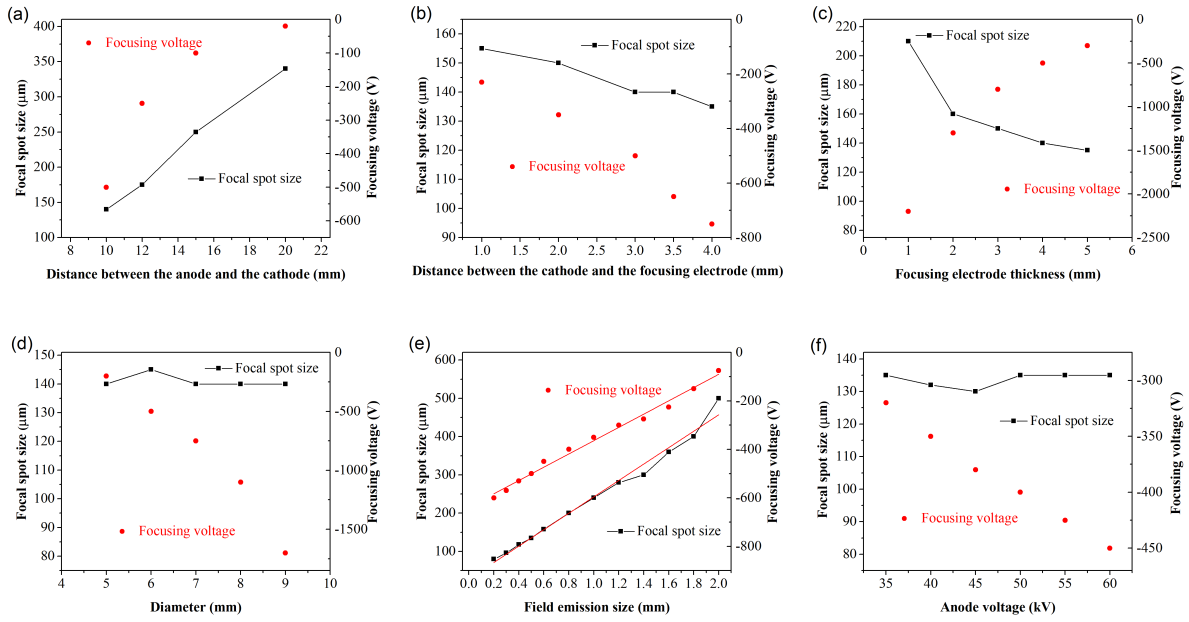

Figure 7.3: Simulation results of the relationships between the focal spot size and (a) the anode-cathode distance, (b) the distance between the cathode and the focusing electrode, (c) the focusing electrode thickness, (d) the focusing electrode diameter, (e) the CNT FEA cathode size, (f) the anode voltage, respectively.

7.2.2 Anode heat load analysis

The anode assembly in X-ray sources is important as the source of the X-rays, as the primary conductor of heat out of the X-ray source, and as an integral part of the high voltage circuit. In any X-ray source, whether thermionic emission or FE, the X-ray flux and the maximum power are ultimately limited by the anode heat load. It is known that as electrons hitting a target only less than 1% of the kinetic energy of electrons is transformed into photon energy as X-rays. The other 99% of the electron kinetic energy becomes the heat loading into the anode. Because the entire anode assembly has to be sealed within an evacuated tube, heat removal is a serious problem and further exacerbated by the high working power. Direct cooling by conduction or convection is difficult. Thermal radiation is greatly limited by small focal spot size of electron beam on the anode. Therefore, the anode target must be made of high melting point materials such tungsten (3695 K) or molybdenum (2896 K). Even so, long time exposure or high emission current is still able to melt the target and damage the anode assembly. In most modern X-ray tubes, the anode is a flat disc with an annular target close to the edge supported by a long stem supported by bearings within the tube with silver powder lubrication. The anode is rotated by electromagnetic induction at a very fast speed (around 3500 rpm). By spinning the anode, the electron beam hits a circular ring area on the target during the exposure, so the heat is spread over a much larger area. A recent development is liquid gallium lubricated fluid dynamic bearings which can withstand very high temperatures without contaminating the tube vacuum to conduct heat from the anode. The approach is able to increase the anode heat load but not suitable for multi-pixel X-ray source. It is necessary to investigate anode heat load features of CNT FE and find proper approach to make the best of anode heat load to increase the maximum X-ray source power.

The high energy electrons are focused within a small area on the target generating a very high heat flux, which results in a very high local temperature in the focal spot area. The focal spot size should be as small as possible to improve the image resolution, but the focus should occupy as large area as possible to limit the temperature rise of heat. Therefore, it is necessary to analyse heat load on X-ray tube anode assembly and identify the temperature distribution and maximum power to balance the two contradictory requirements. In the CNT FEA X-ray source, electrons are generated by the gate electrode from the CNT FEA cathode and accelerated by the anode (40-

100 kV). In simulation, all the electron kinetic energy is assumed to become heat (100%) and concentrates on the bombardment area on the target. The simulated target is a tungsten cylinder with a diameter of 10 mm and a height of 5 mm. The proposed multi-pixel X-ray source has an anode angle of 0°. While most common X-ray sources have anode angles ranging from 5° to 20°. The image resolution is determined by the effective focal spot size, which is the focal spot viewed along the central line of the X-ray beam (Figure 7.4). The real focal spot size has width "a" and length "b", but because the width of the focal spot is at perpendicular to electron beams and the central line of the X-ray, it is not affected by the anode angle. The long axis of the elliptical real focal area b is $1/\sin\theta$ times as the short axis of the elliptical real focal area a, also the diameter of the circular effective focal area, namely $b = a/\sin\theta$. In the simulation, $f_s = a$.

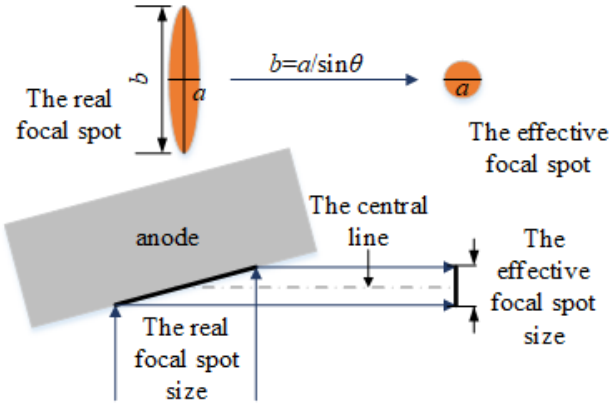

Figure 7.4: Illustration of the relationship between the real and the effective focal spot size.

The anode thermal analysis is conducted by finite element method to solve the three dimensional transient heat conduction differential equation:

$$\rho c_p \frac{\partial T}{\partial t} = \frac{\partial}{\partial x}\left(\frac{\partial}{\partial x}\right) + \frac{\partial}{\partial y}\left(\frac{\partial}{\partial y}\right) + \frac{\partial}{\partial z}\left(\frac{\partial}{\partial z}\right) + P_{in} - P_{out} \tag{7.1}$$

where ρ is the density of the tungsten; T is temperature in Kelvin; t is time in second, c_p and λ are the specific heat ($\mathrm{J \cdot kg^{-1} \cdot K^{-1}}$) and the thermal conductivity ($\mathrm{W \cdot m^{-2} \cdot K^{-1}}$) of the tungsten, respectively. Both the specific heat and the thermal conductivity are functions of temperature. The lists of data of the specific heat and the thermal conductivity of tungsten at

different temperature can be found in [160, 161]. The thermal diffusivity α ($m^2 \cdot s^{-1}$) is defined as $\alpha = \lambda/(\rho c_p)$. This parameter describes the thermal expansion capability of a material in transient heat conduction. Fitting Equations 7.2 and 7.3 are used in the simulation study to describe the functions of the specific heat and the thermal conductivity of the tungsten with temperature, respectively.

$$c_p = 118.21863 + 0.04708T - 2.14864 \times 10^5 T^2 + 5.75361 \times 10^{-9} T^3 \tag{7.2}$$

$$\lambda = 108.34 - 1.05 \times 10^{-4} T + 2.34 \times 10^4 T^{-1} \tag{7.3}$$

P_{in} is the electron beam power on the target. P_{out} is the heat loss from the target. Since X-ray tube anode assembly is sealed in an evacuated chamber, thermal radiation is the only way by which anode exchanges heat with ambient environment. According to Stefan-Boltzmann Law, the net radiation heat dissipation rate of the hot anode radiating energy to the cooler surroundings is expressed as:

$$P_{out} = \varepsilon \sigma A \left(T^4 - T_0^4\right) \tag{7.4}$$

where σ ($= 5.670310^{-8}$ $W \cdot m^{-2} \cdot K^{-4}$) is the Stefan-Boltzmann constant; A is the emitting surface area; ε is the surface emissivity of the tungsten target, which is also a function of temperature [161]. Equation 7.5 is the quadratic polynomial fitting equation of the surface emissivity use in the simulation.

$$\varepsilon = 0.04784 + 1.95695 \times 10^{-4} T - 2.30694 \times 10^{-8} T^2 \tag{7.5}$$

Figure 7.5 shows the specific heat, the thermal conductivity, the thermal diffusivity, and the the surface emissivity of tungsten in relation with temperature.

The criterion to determine the maximum power is that the maximum anode temperature does not exceeds 80% of the melting temperature of Tungsten (3000 K) within 10 ms electron beam bombardment (exposure time required by vivo small-animal imaging [162]). The penetration depth of electrons in target is on the order of several microns, which is far less than the size of the target. Thus, the incident power is defined as a boundary heat flux in simulation. To compare the effect of anode angle on the heat load on the target, anode angles of 0°, 5°, 10°, 15°, 20° are

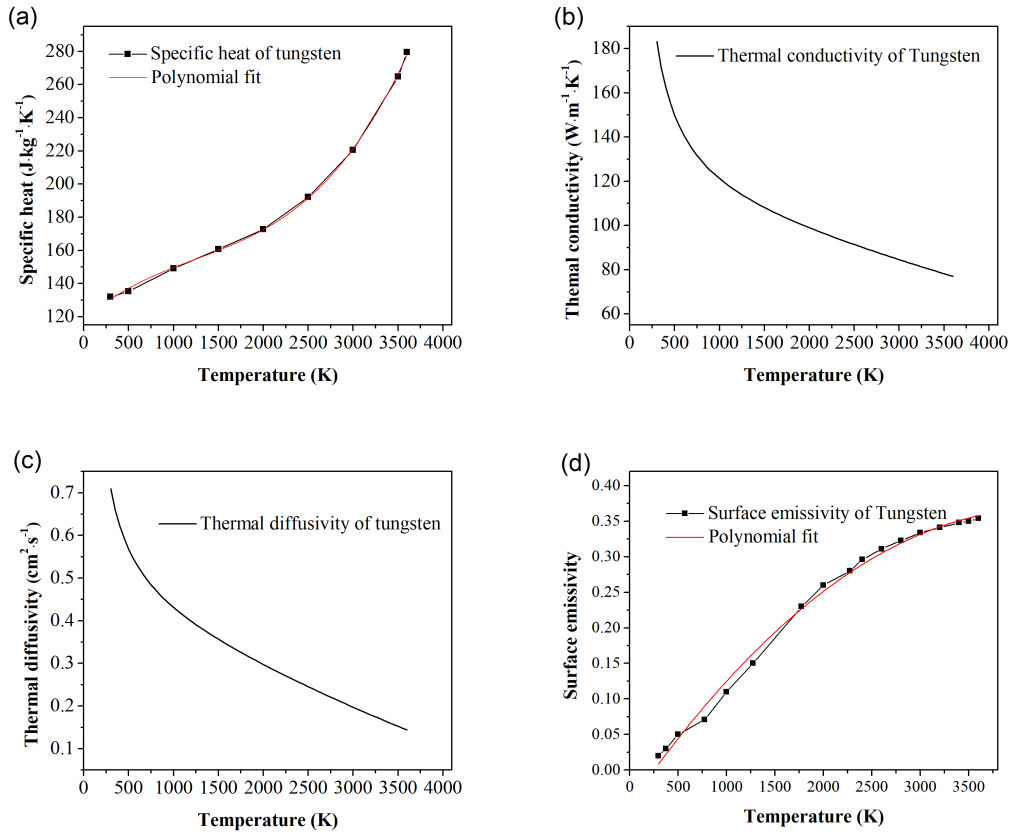

Figure 7.5: Thermal properties of tungsten in relation with temperature: (a) the specific heat, (b) the thermal conductivity, (c) the thermal diffusivity, (d) the surface emissivity.

simulated. Maximum powers limited by focal spot size ranging from 10-1000 μm on the anode is studied. Figure 7.6 shows the temperature distribution on the anode surface with an anode angle of 0° and focal spot size of 200 μm. The total incident power is 98.45 W.

It is seen from Figure7.6 that at the end of electron bombardment, heat is concentrated on focal area. Only the periphery of the focal area has a clear temperature rise, while the most of the anode surface is remaining at room temperature. Figure 7.7(a) shows the temperature distribution along the symmetrical axis along the x-coordinate , which is the short axis of the elliptical focal spot area, on the anode surfaces of different anode angles. According to the Figure 7.4, for the

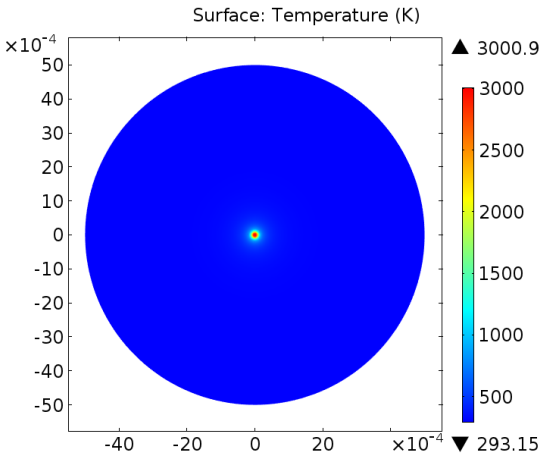

Figure 7.6: Temperature distribution on an anode surface (0°) at 10 ms. The focal spot size is 200 μm and the total energy is 98.45 W.

same effective focal spot area,a smaller the anode angle has a larger the real focal spot area. In this group of anode angles, 0° has the smallest real focal spot area, while 5° has the largest real focal spot area. For the same focal spot size of 100 μm, the maximum power of these five anode angles are 48.30 W, 271.50 W, 159.03 W, 113.30 W, and 89.65 W, respectively, since larger focal spot area can spread heat flux over a larger area, more periphery area of the real focal area is involved in conducting the heat. Figure 7.7(b) shows the maximum temperature on the anodes of different angles changing with time. The electron beam bombardment ends at 10 ms and followed by natural cooling of the anode. From Figure 7.7(b), the maximum temperature rises rapidly from room temperature (293 K) to 3000 K as the incident power is on and drops down at 10 ms when the power is off within a very short period, the same order as temperature rise. For the maximum power that anode can tolerate, Flynn et al gave an empirical expression of the maximum power (P) as function of focal spot size (f_s), which is used to compare with our simulation results [163].

$$P = 1.4 f_s^{0.88} \tag{7.6}$$

Figure 7.7(c) shows maximum power varies with different effective focal spot size (10-1000 μm) and with different anode angles (0°, 5°, 10°, 15°, and 20°), as well as the plot of the Equation

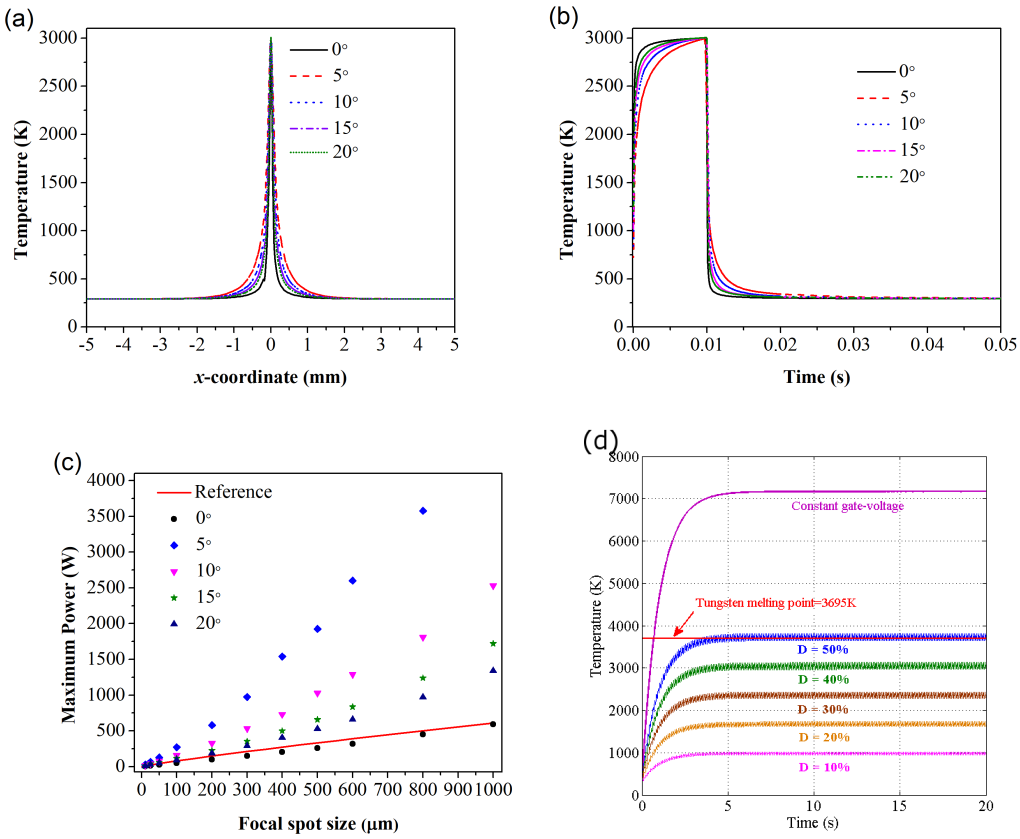

Figure 7.7: Simulation results of anode thermal analysis. (a) Temperature distribution on the symmetrical axis along the x-coordinate on the anode surfaces of different anode angles. (b) Maximum temperature on the anodes of different angles changing with time. (c) Maximum power of different effective focal spot size and different anode angles. (d) The effect of different duty cycle on maximum anode temperature.

7.6. The simulation results of maximum power at 0° fit well with Equation 7.6, indicating that Equation 7.6 can be potentially used to predict maximum power on X-ray anode at 0°. However, there is no explanation on Equation 7.6 that if this equation is used for 0° or other anode angles. In sum, the X-ray anode heat load has two major features: first, the heat load on the anode surface is very concentrated. A very large temperature gradient occurs within the focal spot area. While

the temperature of the anode surface out of the focal spot area remains at room temperature. Therefore, two neighbour pixels of our multi-pixel X-ray source switched on at same time, they will not affect each other. Also, turning on two neighbour pixels at the same time, the heat will not over load the anode. Second, the rapid increase and decrease of maximum temperature when power is on and off. Thus, using pulse mode with proper duty cycle is able to avoid heat load maintain tube efficiency (Figure 7.7(d)).

7.2.3 Geometrical analysis and Monte Carlo study

In order to obtain desired X-ray beams from the multi-pixel X-ray source and avoid inter-pixel interaction of X-ray beams, effects of X-ray source structure on X-ray output, angular distribution of X-ray intensities, and proper collimator design should be studied by geometrical analysis and Monte Carlo (MC) method.

Figure 7.8 shows the variables used for geometrical analysis. X-ray fluence field size on the top plane of the imaging region (A) is investigated with the collimator opening gap (δ), the collimator thickness (H), the aperture size (a), the source to the collimator distance (x), the collimator outlet to top X-ray imaging plane distance (y), and the distance between the top and the bottom plane of the imaging space (z). The X-ray fluence field on the bottom plane of the imaging region is $2A$.

According to the similar triangle theorems, the geometry of has a following relationships:

$$\frac{a}{A} = \frac{x+H}{x+H+y} \tag{7.7}$$

$$\frac{a}{2A} = \frac{x+H}{x+H+y+z} \tag{7.8}$$

where $A = a+\delta$. Considering the circuit arrangement and collimator machining, each CNT FEA cathode is 5 mm away from its neighbouring counterparts, a collimator has a septal thickness of 3 mm, and thus a collimator aperture width of 2 mm. Correspondingly, the X-ray fluence field size (A) on the top plane is 5 mm, $y = 1.5(x+H)$, and $z = 2.5(x+H)$. Since X-ray is a high energy photon beam, it has a strong penetration capability though materials. Besides, X-ray

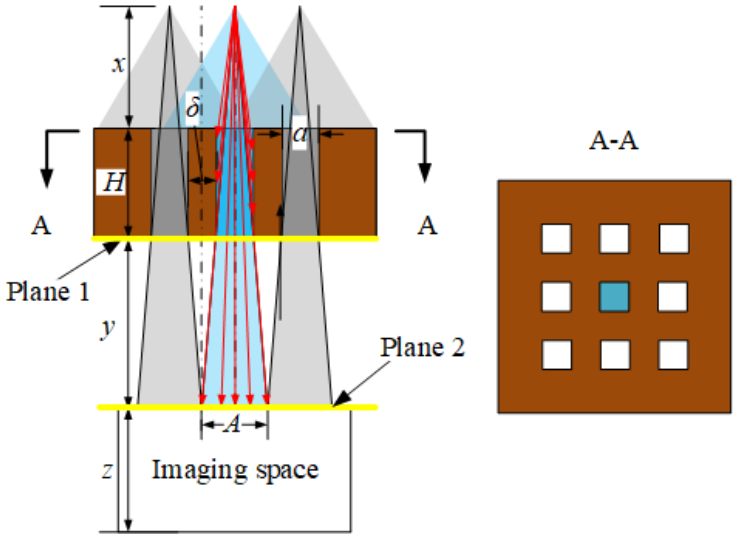

Figure 7.8: Geometric analysis and simulation model of the multi-pixel X-ray source for fluence field modulation.

photons interact with collimator materials. It is likely that X-ray beam width is not perfectly as designed in Figure 7.8. Therefore, MC method is used to find out the optimized collimator thickness (H), the source- to- collimator distance (x), and the distance between the collimator outlet to the top X-ray imaging plane (y). Ideally, the smallest H that effectively collimates X-ray beam is desired.

MC techniques have been widely used for clinical and research radiation dosimetry studies including X-ray dosimetry. MC study tools such as PNELOPE code system, GEANT4 toolkit, and Electron Gamma Shower (EGS) code system have successfully investigated collimator parameters on dose distribution and micro-beam parameters [164–166]. EGS code system is the latest in a line of electromagnetic radiation transport simulations used in high-energy, nuclear, and medical physics. The program is free to all users and developed by National Research Council Canada. The included BEAMnrc software component can model electron and photon beams travelling through consecutive material components, ranging from a simple slab to the full treatment head of a radiotherapy linear particle accelerator. Calculations in the X-ray device, including electron beam, anode, and collimator are performed using BEAMnrc. Data process is

performed by the companion package BEAMdp.

Figure 7.8 shows the model built in the MC simulation. The collimator has 3×3 square opening array. Each opening has a width of 2 mm and 5 mm centre to centre distance. The collimator material is copper for the sake of machining convenience. The simulation process starts with the electron pixel beam bombarding the target (anode) and followed by X-ray generation. The cone beam X-ray is projected from the anode surface that is 2 cm away from the top surface of the collimator right through the centre aperture. The X-ray beam has an energy of 100 keV and a focal spot size of 200 μm on the anode surface. There are two scoring plane in the simulation model. Plane 1 is set right on the downstream edge of the collimator to characterize the inter-pixel crosstalk. The distance between the Plane 1 and the X-ray source is $x + H$. For the multi-pixel X-ray source, inter-pixel crosstalk may be due to X-ray beam going through not only the designated collimator opening but also the neighbouring openings. The inter-pixel crosstalk can be mitigated by optimizing the design parameters including the collimator thickness and the position. Ideally, X-ray "leakage" through the neighbouring aperture should be less than 0.25%. The various Plane 2 is set on the top plane of the imaging region to characterize the X-ray beam profile entering the imaging region. The distance between the Plane 2 and the downstream edge of the collimator is y. Models with various combination of "x, H, and y" are simulated to find out the optimized position and thickness of the collimator. Table 7.2 shows the six models with various geometrical parameters.

Figure 7.9 indicates the resulting X-ray beam profiles of the centre X-ray source and the its "leakage" through the neighbouring collimator openings with different source-to-collimator distances and collimator thickness. The X-ray fluence field strength along the x-coordinate is normalized to the maximum fluence that is in the centre point.

It can be seen from the Figure 7.9 that collimator of the Model 6 is the thickest, leading to has the smallest inter-pixel crosstalk effect on the neighbouring openings. For the same collimator thickness, collimator that is placed closed to the X-ray source is able to mitigate the X-ray "leakage". For the source-to-collimator distance of 2 mm, 3 mm thick collimator is able to limit the maximum "leakage" to 0.18% compared with the centre X-ray fluence. While, Model 1, which has the largest inter-pixel crosstalk, has a maximum "leakage" of 0.46%. Therefore, Model 6

Table 7.2: MC simulation models with various combination of geometrical parameters.

Model number	x (cm)	H (cm)	y (cm)
Model 1	3	2	7.5
Model 2	2.5	2	6.75
Model 3	2	2	6
Model 4	2	2.5	6.75
Model 5	2.5	2.5	7.5
Model 6	2	3	7.5

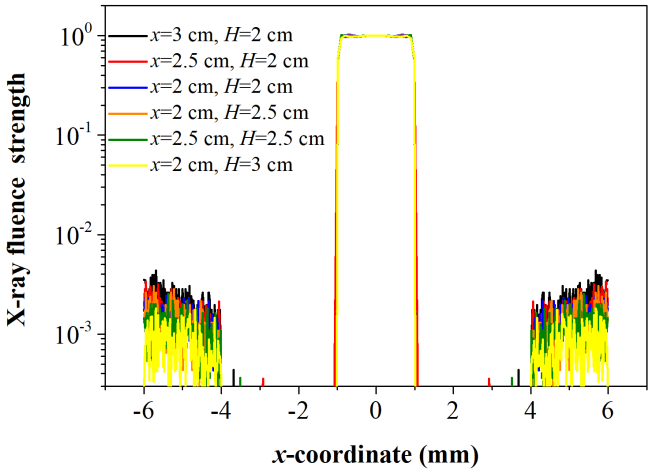

Figure 7.9: Inter-pixel crosstalk effect for various combination of source-to-collimator distances and collimator thickness characterized on the Plane 1.

meets the requirement of maximum "leakage" lower than 25%. Further simulation study shows that for the source-to-collimator distance of 2 mm, thick collimator makes no signification contribution to lowering the "leakage". Therefore, the collimator thickness of 3 mm is the smallest thickness that effectively eliminate the inter-pixel crosstalk.

Figure 7.10 shows the X-ray beam profile on the Plane 2. The "leakage" seen on the Plane 1 does not influence the X-ray beam profile on the Plane 2. This result verifies that 3 mm collimator placed 2 mm away from the X-ray source can effectively eliminate the inter-pixel crosstalk.

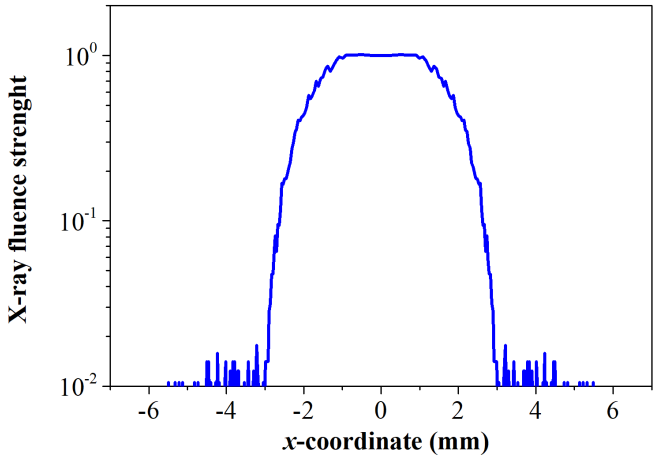

Figure 7.10: X-ray beam profile of the 3 mm collimator placed 2 mm away from the X-ray source characterized on the Plane 2.

Figure 7.11(a)and (b) shows the 3D view of the X-ray beam profile of the Model 6 on the Plane 1 and Plane 2, respectively. Inter-pixel crosstalk is mitigated by the designed collimator. The "leakage" through the neighbouring apertures seen on the Plane 1 does not reflected on the Plane 2. Figure 7.11(c)and (d) show the $x-y$ view of the X-ray fluence of Model 6 and Model 1 on the Plane 2, respectively. Model 1 has a larger inter-pixel crosstalk effect seen on the Plane 1. This crosstalk clearly influence the X-ray fluence field. This result verifies that the model 6 can be applied to setting up X-ray fluence field modulation experiment.

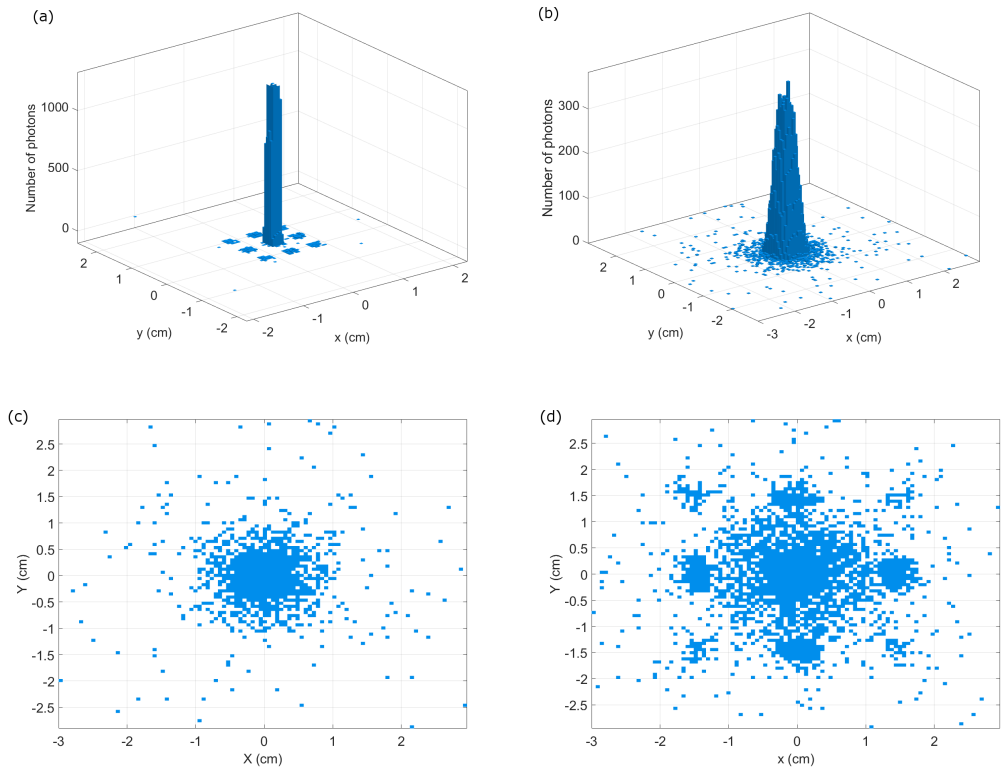

Figure 7.11: X-ray beam profiles: (a) the 3D view of the X-ray beam profile of the Model 6 on the Plane 1; (b) the 3D view of the X-ray beam profile of the Model 6 on the Plane 2; (c) the $x-y$ view of the X-ray fluence of the Model 6 on the Plane 2; (d) the $x-y$ view of the X-ray fluence of the Model 1 on the Plane 2.

7.3 Experimental study

7.3.1 Dual-pixel X-ray source

For a 2D multi-pixel X-ray source without a collimator, X-ray pixels can still work together as a multi-pixel cone beam X-ray source, which can be potentially applied for IGRT or stationary tomosynthesis. To demonstrate this feature and verify the set-ups, a dual-pixel X-ray source without a collimator is built. Figure 7.12 shows the structure of the set-up. The X-ray source em-

ploys diode configuration. The anode applies 45 kV voltage to the cathode, which is connected to the ground. The target is a tungsten plate embedded in to a copper plate with a diameter of 1 inch and a thickness of 1/8 inch. The CNT FEA cathode is the same as described in the Chapter 5 with 8620 CNT field emitters within 1 mm^2 and emitter-to-emitter distance of 10 μm in the array. The gap between the two cathodes is 10 mm. The anode-cathode gap is 5 mm. Anode-object gap is 35 mm. The X-ray film is placed 55 mm away from the anode. The set-up is housed in a vacuum chamber under a base pressure of 5×10^{-10} Torr.

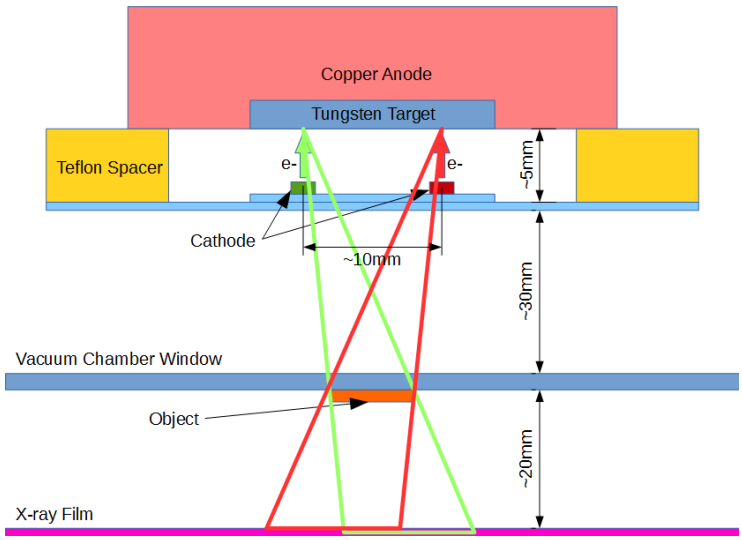

Figure 7.12: The schematic of the dual-pixel X-ray source.

As is shown in Figure 7.13, the pinhole image and indicates that multiple X-ray cathodes contributed to the X-ray image independently. The pinhole is a hole of 0.5 mm in diameter on a 1 mm thick lead plate. The X-ray exposure time is 100 s.

The X-ray image of the two objects are exposed for 45 s with a total FE current of 800 μA combined by the two CNT FEA cathodes combine. It can be seen from Figure 7.14(a) that both CNT cathodes are working stably. The X-ray dose generated is also very stable (Figure 7.14(b)).

The X-ray imaging objects are a piece of flat washer and a piece of integrated circuit board. Figure 7.15 shows the photo and the X-ray images of the two objects generated by the dual-pixel

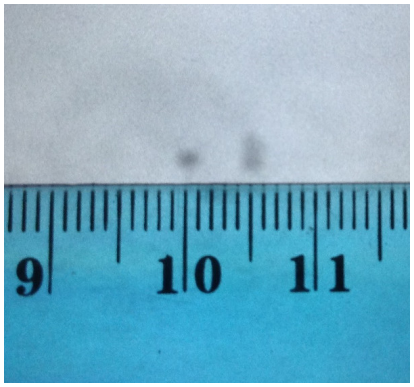

Figure 7.13: The X-ray image of the pinhole from the dual-pixel X-ray source.

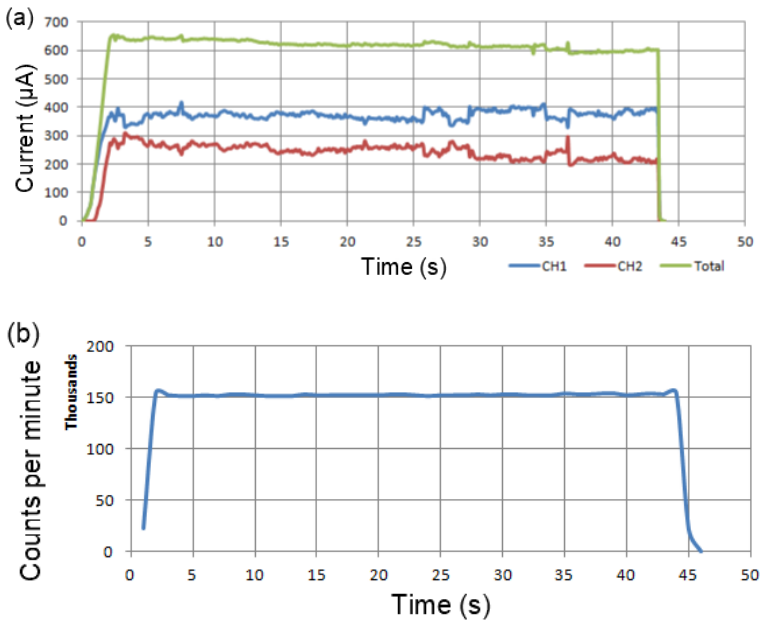

Figure 7.14: (a) FE current from the two CNT FEA cathode. The two cathodes combine a total FE current of 800 μA. (b) The X-ray dose generated during the 45 s exposure.

X-ray source. Since there is no electron focusing components, the resolution of the X-ray image is not as good as the X-ray image resolution in the Chapter 6.

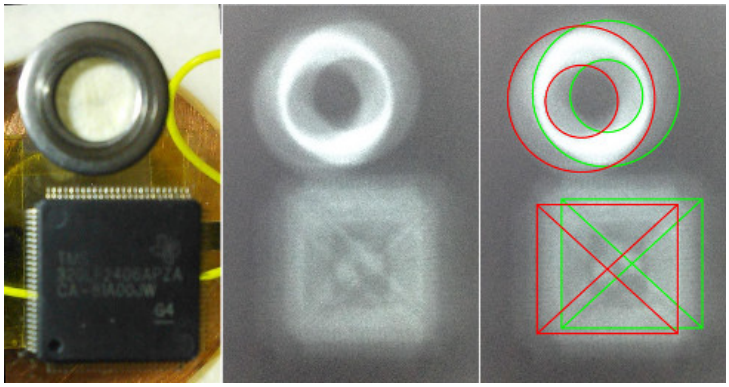

Figure 7.15: The photo and the X-ray images of a piece of flat washer and a piece of integrated circuit board.

7.3.2 X-ray fluence field study

Using the same set-up as the dual-pixel X-ray source, we apply the collimator to verify the MC simulation results. The collimator is made of copper and machined to have 5×5 openings. The four corner openings are round holes for making the CNT FEA cathode, the target, and the collimator well aligned along the same axis. As is determined by the MC simulation, the other openings are 2 mm square holes to for shaping the X-ray beam with 5 mm apart. The collimator is 3 cm thick. Figure 7.16 shows the collimator.

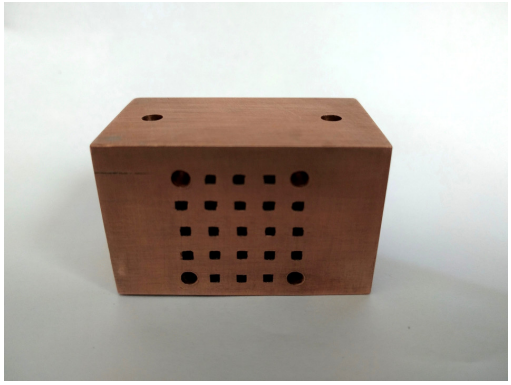

Figure 7.16: The photo of the copper collimator with 5×5 openings.

In the experiment, the anode-to-cathode distance is 2 cm, which is the same as that in the MC simulation. The CNT FEA cathode is aligned the to centre opening of the collimator. To verify that the collimator is capable of shaping the X-ray beam without inter-pixel crosstalk, we place a piece of Gafchromic EBT films on the bottom surface of the collimator. The Gafchromic EBT film is a type of self-developing X-ray film, which is designed for the measurement of absorbed doses of ionizing radiation. X-ray radiation darkens the radiation exposure area on the Gafchromic EBT film. With this film, X-ray fluence field through the collimator openings can be directly observed and recoded. Figure 7.17 hows the corresponding X-ray radiation delivered to a piece of Gafchromic EBT film.

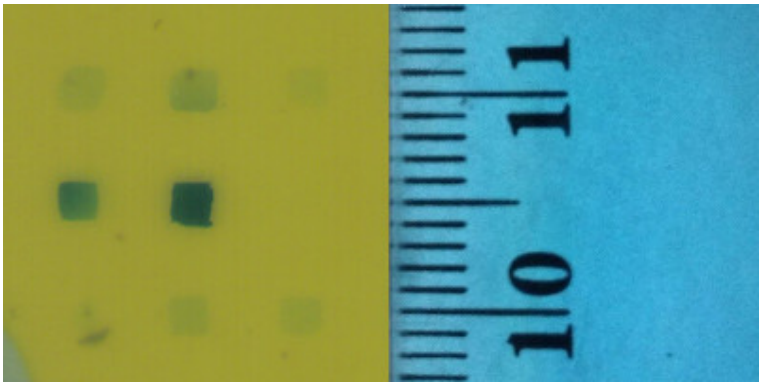

Figure 7.17: X-ray fluence field observed on a piece of Gafchromic EBT film.

It can be seen from the Figure 7.17 that the X-ray radiation patterns on the Gafchromic EBT film match well with MC simulation results shown in the Figure 7.11(a). The X-ray radiation patterns are 2 mm square and 5 mm apart, which is exactly the same as the openings on the collimator. The X-ray radiation though the centre opening of the collimator is the strongest, while the X-ray radiation through the neighbouring openings are very light. However, the X-ray radiation through the centre left openings is stronger than the other three openings adjacent to the centre opening. There is no X-ray radiation can been seen from the centre right. We believe this phenomenon is due to a little off-set of the CNT FEA to the left. The centre top and centre bottom X-ray radiation pattern are comparable to each other. This results verify that the MC simulation on designing the collimator can effectively eliminate the inter-pixel crosstalk.

7.4 Chapter summary

This chapter provides an comprehensive design and investigation on fluence field modulated X-ray source based on CNT FEA. The simulation study on electron beam focusing indicates that one focusing electrode and proper focusing voltage in CNT FE based X-ray tube is able to focus electron beam in a desired focal spot size. It can be concluded that a small anode-cathode distance, relatively large distance between the cathode and the focusing electrode, reduced FE size is able reduce X-ray tube focal spot size. Smaller focusing aperture size and lower anode voltage result in lower focusing voltage. Measurement of focal spot size is needed in practical situation.

The anode thermal analysis provide an proper solution to increase the maximum X-ray source power and lifetime of both anode and CNT FEA. Conventional thermionic emission based X-ray source employs rotation anode to maintain high tube power. However, this approach is not suitable for FE based multi-pixel X-ray source due to limited size and compact configuration. The temperature distribution on the anode when X-ray source is operating is quite concentrated. Using well-designed pulsed FE is able to achieve fast heat dissipation on anode.

MC simulation has played an irreplaceable role in the development of the multi-pixel X-ray system for X-ray fluence field modulation by providing guidance to the system design and performance evaluation. The MC simulation study on collimator design in this chapter successfully provides an insight on building system geometrical structure and collimator to achieve X-ray fulence field modulation and eliminating inter-pixel crosstalk. The experimental study on the X-ray fluence field verifies that the collimator designed by MC simulation is feasible and effective to eliminate the inter-pixel crosstalk.

Chapter 8

Summary and future work

8.1 Summary

The research reported in this thesis provides an systematic study on CNT FEA uniformity and failure mechanism and its application as the electron source for self-focusing X-ray source integrated with resonant transformer and X-ray fluence field modulation. The entire research starts with the fundamental study of FE uniformity and CNT field emitter failure mechanism. Based on the knowledge and understanding of FE uniformity and CNT field emitter failure mechanism, the research moves to design and fabricate stable and reliable CNT FEAs individually ballasted by silicon current limiters. Then, the research focuses on more practical applications, building and designing compact self-contained X-ray and multi-pixel X-ray source for X-ray fluence field modulation based on CNT FEA. In Chapter 3, a novel and effective FEM method based on PMMA thin film and microscopic camera is proposed and demonstrated to study the FE uniformity and observe the CNT field emitter failure of free-standing CNT FEA. In Chapter 4, a systematic characterization and understanding of the CNT emitter failure behaviour and mechanism are performed using the PMMA thin film based FEM method combined with various techniques. In Chapter 5, individually ballasted CNT FEAs using silicon current limiter is designed and demonstrated. In Chapter 6, CNT FEA cathode is applied to building a self-contained and self-focusing compact pulsed X-ray source integrated with a resonant transformer. In Chap-

ter 7, a comprehensive design and feasibility study of two-dimensional multi-pixel X-ray source for X-ray fluence field modulation is conducted using finite element analysis and MC simulation.

The FEM method based on PMMA thin film with microscopic camera is novel and effective to study the FE uniformity and CNT emitter failure of CNT FEA. The FE uniformity is visualized and recorded on the PMMA thin film by studying the FE uniformity of 11×11 and 20×20 free-standing CNT FEA under a low control voltage. The distinguishable size and shape of FEM patterns on the PMMA thin film indicate five levels of the FE current contribution from each emitter. By numbering the CNT emitters and the corresponding FEM patterns, the proposed approach allows to learn the details of the CNT emitter morphology from the FEM pattern. Multiple CNT emitters at an emission site can also be reflected by the FEM pattern on the PMMA thin film. The proposed approach is able to resolve the major challenge of building the relationship between CNT FE performance and emitter morphology from three aspects: observation and quantification of FE uniformity of CNT FEAs, locating any CNT emitter from a CNT FEA corresponding to its FEM pattern, and real-time FE performance study. With the help of microscopic camera, a unique phenomenon of light emission and Coulomb explosion of CNT field emitter failure is observed and captured. The CNT emitter failure behaviour is due to a combined effect of Joule heating and massive charging at high FE current. The FE current levels that disintegrate the CNT emitters range from 1.96 μA to 41.82 μA with an average of 11.82 μA. Joule heating heats a CNT emitter to over 2500 K within a very short period, melt the contact area, and weaken the carbon bond and van der Waals force of graphite basal planes in the CNT. With the aid of Joule heating, excessive charging disintegrates the CNT emitters into charge fragments. Then an instantaneous release of electrons from CNT fragments through the PMMA thin film leading to the annular crater and the sputter of PMMA all around in a range of about 100 mm. The explosion generates an "firework-like" FEM patterns on the PMMA thin film of about 60-70 μm in diameter.

Based on the knowledge and understanding of FE uniformity and CNT field emitter failure mechanism, it is of great importance to limit the FE current from each CNT field emitter in an FEA without sacrificing FE efficiency and performance. Individually ballasted FEA using carrier velocity saturation of well-doped silicon current limiter has been applied on silicon FEAs but is rarely seen in CNT FEAs. A novel and effective fabrication process of individually ballast CNT

FEA using silicon current limiters is designed. Each CNT emitter is patterned and synthesized in series with a well-designed silicon current limiter. The FE performance from CNT FEAs using silicon current limiter is experimentally investigated and characterized. The proposed CNT FEAs show an obvious current limiting effect without losing the sensitivity and efficiency. By exploiting the protective effect of the saturation current, the proposed CNT FEA exhibits improved repeatability and stability.

The CNT FEA is integrated with a self-contained and self-focusing compact X-ray source based on a resonant transformer. The proposed X-ray source has four benefits. First, the integrated resonant transformer is compatible with CNT FEA that are working under a well-designed pulsed mode. In the anode thermal analysis, it is found that the rapid increase and decrease of maximum temperature when power is on and off. Thus, using pulse mode with proper duty cycle is able to avoid heat load and maintain tube efficiency. Therefore, the accurate control of switching FE "ON" and "OFF" protects the CNT FEA and the anode parts from being damaged under high voltage and high current conditions. Second, high voltage generator is closely integrated with the X-ray components. Since there is no need for high voltage insulation outside the vacuum chamber, the reliability is further improved and the size of the system is further decreased. Third, the electron beam is self-focused by the magnetic field that is generated by the transformer. As such, no extra focusing components and circuit are needed. Fourth, FE of the CNT FEA operates only under high voltage. As a result, low energy electrons emission is eliminated. Benefiting from the integrated high voltage circuit and electron beam focusing features, the X-ray source has a sub-millimetre scale resolution.

In designing 2D multi-pixel X-ray source for X-ray fluence field modulation, a scanning pattern is demonstrated. The neighbouring pixels are activated alternatively. The pixels are divided into four groups and launched one by one. Each X-ray image needs four exposures. Finite element analysis is used to investigate the electron beam focusing and anode heat load. A focal spot size as small as 140 μm can be achieved. It can be concluded that a small anode-cathode distance, relatively large distance between the cathode and the focusing electrode, reduced FE size is able reduce X-ray tube focal spot size. Smaller focusing aperture size and lower anode voltage result in lower focusing voltage. The X-ray anode heat load has two major features: first, the heat load on the anode surface is very concentrated. A very large temperature gradient occurs

within the focal spot area. While the temperature of the anode surface out of the focal spot area remains at room temperature. Therefore, two neighbour pixels of our multi-pixel X-ray source switched on at same time, they will not affect each other. Also, turning on two neighbour pixels at the same time, the heat will not over load the anode. Second, the rapid increase and decrease of maximum temperature when power is on and off. Thus, using pulse mode with proper duty cycle is able to avoid heat load maintain tube efficiency. Using MC simulation, a copper collimator is design to regulate multi-pixel X-ray beams to achieve variation of X-ray fluence field shape. For the source-to-collimator distance of 2 mm, a collimator thickness of 3 mm is the smallest thickness that effectively eliminate inter-pixel crosstalk. The collimator designed by the MC study is successfully verified by the experimental study on the X-ray fluencce field.

8.2 Future work

Future work of this research can be performed from two aspects: optimizing the individually ballast CNT FEA using silicon current limiters and building 2D multi-pixel X-ray source for fluence field modulation.

In the Chapter 5, the designed n-type silicon current limiter has a doping concentration of 1×10^{14} cm^{-3}, a length of 10 μm and a cross-section area of 1 μm^2. Due to the velocity saturation of electrons in silicon, the designed silicon current limiter achieves a saturation current of 1.56 μA. For the CNT FEA optimization, various doping concentrations of the silicon current limiter can be experimentally characterized. Silicon current limiter iwth lower doping concentration should have a more evident saturation effect than that is studied in the Chapter 5. Different geometrical sizes such as smaller cross-sectional area are worth of being investigated. Integrated coaxial gate electrode could be fabricated after the CNT synthesized on top of the silicon current current limiter. Future work on optimizing the individually ballast CNT FEA using silicon current limiters should aim at figuring out the best doping concentration and geometric size of the silicon current limiter.

For building 2D multi-pixel X-ray source for fluence field modulation, gate electrode needs to be applied to achieve fast switching pulsed X-ray beams. A 2×2 or 3×3 multi-pixel X-ray

source could be built to demonstrate the performance of the fluence field modulation and the feasibility of the designed scanning pattern. Expanding the number of the pixel would bring more complicated control circuit design and a more clever routing strategy. Consistency and uniformity among CNT FEA cathodes in the multi-pixel X-ray source should be well characterized. X-ray beam quality characterization using pin-hole test and cross wire phantom needs to be performed. Demonstration of X-ray fluence field modulation should include variation in exposure time from pixel to pixel and variation of the X-ray fluence field shape. Calibration is demanded before experimental study and may be compared with the MC simulation in the Chapter 7.

References

[1] David J Brenner and Eric J Hall. Computed tomographyan increasing source of radiation exposure. *New England Journal of Medicine*, 357(22):2277–2284, 2007.

[2] Sumio Iijima. Helical microtubules of graphitic carbon. *Nature*, 354(6348):56, 1991.

[3] AG Rinzler, JH Hafner, P Nikolaev, P Nordlander, DT Colbert, RE Smalley, L Lou, SG Kim, and D Tománek. Unraveling nanotubes: field emission from an atomic wire. *Science*, 269(5230):1550–1553, 1995.

[4] Xueshen Wang, Qunqing Li, Jing Xie, Zhong Jin, Jinyong Wang, Yan Li, Kaili Jiang, and Shoushan Fan. Fabrication of ultralong and electrically uniform single-walled carbon nanotubes on clean substrates. *Nano Letters*, 9(9):3137–3141, 2009.

[5] Yucheng Lan, Yang Wang, and ZF Ren. Physics and applications of aligned carbon nanotubes. *Advances in Physics*, 60(4):553–678, 2011.

[6] Walt A De Heer, A Chatelain, and D Ugarte. A carbon nanotube field-emission electron source. *Science*, 270(5239):1179–1180, 1995.

[7] KBK Teo, SB Lee, M Chhowalla, V Semet, Vu Thien Binh, O Groening, M Castignolles, A Loiseau, G Pirio, P Legagneux, et al. Plasma enhanced chemical vapour deposition carbon nanotubes/nanofibres-how uniform do they grow? *Nanotechnology*, 14(2):204, 2003.

[8] Anatoli Vasilievich Melechko, Vladimir I Merkulov, Timothy E McKnight, MA Guillorn, Kate L Klein, Douglas H Lowndes, and Michael L Simpson. Vertically aligned carbon nanofibers and related structures: controlled synthesis and directed assembly. *Journal of Applied Physics*, 97(4):3, 2005.

[9] Yunhan Li, Yonghai Sun, and JTW Yeow. Nanotube field electron emission: principles, development, and applications. *Nanotechnology*, 26(24):242001, 2015.

[10] Yonghai Sun, John TW Yeow, and David A Jaffray. Design and fabrication of carbon nanotube field-emission cathode with coaxial gate and ballast resistor. *Small*, 9(20):3385–3389, 2013.

[11] Maya Doytcheva, Monja Kaiser, and Niels De Jonge. In situ transmission electron microscopy investigation of the structural changes in carbon nanotubes during electron emission at high currents. *Nanotechnology*, 17(13):3226, 2006.

[12] Yonghai Sun, David A Jaffray, and John TW Yeow. The design and fabrication of carbon-nanotube-based field emission X-ray cathode with ballast resistor. *IEEE Transactions on Electron Devices*, 60(1):464–470, 2013.

[13] Geng Zhang, Jun Chen, SZ Deng, JC She, and NS Xu. Damages of screen-printed carbon nanotube cold cathode during the field emission process. *Ultramicroscopy*, 109(5):385–389, 2009.

[14] Chi Li, Yan Zhang, Matthew T Cole, Sai G Shivareddy, Jon S Barnard, Wei Lei, Baoping Wang, Didier Pribat, Gehan AJ Amaratunga, and William I Milne. Hot electron field emission via individually transistor-ballasted carbon nanotube arrays. *ACS Nano*, 6(4):3236–3242, 2012.

[15] Edward Leo Murphy and RH Good Jr. Thermionic emission, field emission, and the transition region. *Physical review*, 102(6):1464, 1956.

[16] SG Christov and CM Vodenicharov. On the experimental proof of the general theory of electron emission from metals. *Solid-State Electronics*, 11(8):757–766, 1968.

[17] Owen Willans Richardson. The electrical conductivity imparted to a vacuum by hot conductors. *Proceedings of the Royal Society of London*, 71(467-476):415–418, 1903.

[18] CR Crowell. The richardson constant for thermionic emission in schottky barrier diodes. *Solid-State Electronics*, 8(4):395–399, 1965.

[19] ME Kiziroglou, X Li, AA Zhukov, PAJ De Groot, and CH De Groot. Thermionic field emission at electrodeposited ni–si schottky barriers. *Solid-State Electronics*, 52(7):1032–1038, 2008.

[20] Jon Orloff. *Charged Particle Optics*. Wiley Online Library, 2009.

[21] K Junker and K Heinz. Experimental examination of the field-enhanced thermal emission of holes in cds. *Physica Status Solidi (a)*, 21(2):451–456, 1974.

[22] George N Fursey. *Field emission in vacuum microelectronics*. Springer Science & Business Media, 2007.

[23] L Nordheim. Electron emission in intense electric fields. In *Proc. R. Soc. Lond. A*, volume 119, pages 173–181. The Royal Society, 1928.

[24] TE Stern and BS Gossling. Further studies in the emission of electrons from cold metals. In *Proc. R. Soc. Lond. A*, volume 124, pages 699–723. The Royal Society, 1929.

[25] Robert A Millikan and Charles C Lauritsen. Dependence of electron emission from metals upon field strengths and temperatures. *Physical Review*, 33(4):598, 1929.

[26] X Lu, Q Yang, C Xiao, and A Hirose. Nonlinear Fowler–Nordheim plots of the field electron emission from graphitic nanocones: influence of non-uniform field enhancement factors. *Journal of Physics D: Applied Physics*, 39(15):3375, 2006.

[27] CA Spindt. A thin-film field-emission cathode. *Journal of Applied Physics*, 39(7):3504–3505, 1968.

[28] Charles A Spindt, Christopher E Holland, and Robert D Stowell. Field emission cathode array development for high-current-density applications. *Applications of Surface Science*, 16(1-2):268–276, 1983.

[29] RN Thomas and HC Nathanson. Photosensitive field emission from silicon point arrays. *Applied Physics Letters*, 21(8):384–386, 1972.

[30] FS Baker, AR Osborn, and J Williams. The carbon-fibre field emitter. *Journal of Physics D: Applied Physics*, 7(15):2105, 1974.

[31] D Temple, WD Palmer, LN Yadon, JE Mancusi, D Vellenga, and GE McGuire. Silicon field emitter cathodes: Fabrication, performance, and applications. *Journal of Vacuum Science & Technology A: Vacuum, Surfaces, and Films*, 16(3):1980–1990, 1998.

[32] J Liu, VV Zhirnov, GJ Wojak, AF Myers, WB Choi, JJ Hren, SD Wolter, MT McClure, BR Stoner, and JT Glass. Electron emission from diamond coated silicon field emitters. *Applied Physics Letters*, 65(22):2842–2844, 1994.

[33] Junji Itoh, Yasushi Tohma, Kazutoshi Morikawa, Seigo Kanemaru, and Keizo Shimizu. Fabrication of double-gated Si field emitter arrays for focused electron beam generation. *Journal of Vacuum Science & Technology B: Microelectronics and Nanometer Structures Processing, Measurement, and Phenomena*, 13(5):1968–1972, 1995.

[34] Michael E Swanwick, Phillip D Keathley, Arya Fallahi, Peter R Krogen, Guillaume Laurent, Jeffrey Moses, Franz X Kartner, and Luis F Velasquez-García. Nanostructured ultrafast silicon-tip optical field-emitter arrays. *Nano Letters*, 14(9):5035–5043, 2014.

[35] SA Guerrera and AI Akinwande. Nanofabrication of arrays of silicon field emitters with vertical silicon nanowire current limiters and self-aligned gates. *Nanotechnology*, 27(29):295302, 2016.

[36] Luis Fernando Velasquez-Garcia, Stephen A Guerrera, Ying Niu, and Akintunde Ibitayo Akinwande. Uniform high-current cathodes using massive arrays of si field emitters individually controlled by vertical Si ungated FETs-Part 1: Device design and simulation. *IEEE Transactions on Electron Devices*, 58(6):1775–1782, 2011.

[37] Luis Fernando Velasquez-Garcia, Stephen A Guerrera, Ying Niu, and Akintunde Ibitayo Akinwande. Uniform high-current cathodes using massive arrays of si field emitters individually controlled by vertical Si ungated FETs-Part 2: Device fabrication and characterization. *IEEE Transactions on Electron Devices*, 58(6):1783–1791, 2011.

[38] Stephen A Guerrera, Luis Fernando Velasquez-Garcia, and Akintunde Ibitayo Akinwande. Scaling of high-aspect-ratio current limiters for the individual ballasting of large arrays of field emitters. *IEEE Transactions on Electron Devices*, 59(9):2524–2530, 2012.

[39] Anirban Basu, Michael E Swanwick, Arash A Fomani, and Luis Fernando Velásquez-García. A portable x-ray source with a nanostructured Pt-coated silicon field emission cathode for absorption imaging of low-Z materials. *Journal of Physics D: Applied Physics*, 48(22):225501, 2015.

[40] Shuo Cheng, Frances Ann Hill, Eric Vincent Heubel, and Luis Fernando Velásquez-García. Low-bremsstrahlung X-ray source using a low-voltage high-current-density nanostructured field emission cathode and a transmission anode for markerless soft tissue imaging. *Journal of Microelectromechanical Systems*, 24(2):373–383, 2015.

[41] RL Fink, Z Li Tolt, and Z Yaniv. The status and future of diamond thin film FED. *Surface and Coatings Technology*, 108:570–576, 1998.

[42] Ken Okano, Kimihiko Hoshina, Masamori Iida, Satoshi Koizumi, and Tadao Inuzuka. Fabrication of a diamond field emitter array. *Applied Physics Letters*, 64(20):2742–2744, 1994.

[43] JK Cochran, AT Chapman, DN Hill, and KJ Lee. Low-voltage field emission from tungsten fiber arrays in a stabilized zirconia matrix. *Journal of Materials Research*, 2(3):322–328, 1987.

[44] Jun Zhou, Li Gong, Shao Zhi Deng, Jun Chen, Jun Cong She, Ning Sheng Xu, Rusen Yang, and Zhong Lin Wang. Growth and field-emission property of tungsten oxide nanotip arrays. *Applied Physics Letters*, 87(22):223108, 2005.

[45] CJ Lee, TJ Lee, SC Lyu, Y Zhang, H Ruh, and HJ Lee. Field emission from well-aligned zinc oxide nanowires grown at low temperature. *Applied Physics Letters*, 81(19):3648–3650, 2002.

[46] Yunhan Li, Shruti Nambiar, Yonghai Sun, Chintamani NR Rao, and John TW Yeow. Experimental study on field emission performance of bismuth sulfide nanoflowers. In *Nanotechnology (IEEE-NANO), 2014 IEEE 14th International Conference on*, pages 1–4. IEEE, 2014.

[47] Mildred S Dresselhaus, Gene Dresselhaus, and Peter C Eklund. *Science of fullerenes and carbon nanotubes: their properties and applications*. Elsevier, 1996.

[48] Meyya Meyyappan. *Carbon nanotubes: science and applications*. CRC press, 2004.

[49] Hongjie Dai. Carbon nanotubes: synthesis, integration, and properties. *Accounts of Chemical Research*, 35(12):1035–1044, 2002.

[50] Jean-Christophe Charlier, Xavier Blase, and Stephan Roche. Electronic and transport properties of nanotubes. *Reviews of Modern Physics*, 79(2):677, 2007.

[51] Jian Ping Lu. Elastic properties of carbon nanotubes and nanoropes. *Physical Review Letters*, 79(7):1297, 1997.

[52] Philippe Poncharal, ZL Wang, Daniel Ugarte, and Walt A De Heer. Electrostatic deflections and electromechanical resonances of carbon nanotubes. *Science*, 283(5407):1513–1516, 1999.

[53] Eric Pop, David Mann, Qian Wang, Kenneth Goodson, and Hongjie Dai. Thermal conductance of an individual single-wall carbon nanotube above room temperature. *Nano Letters*, 6(1):96–100, 2006.

[54] Saion Sinha, Saimir Barjami, Germano Iannacchione, Alexander Schwab, and George Muench. Off-axis thermal properties of carbon nanotube films. *Journal of Nanoparticle Research*, 7(6):651–657, 2005.

[55] Andrea Szabó, Caterina Perri, Anita Csató, Girolamo Giordano, Danilo Vuono, and János B Nagy. Synthesis methods of carbon nanotubes and related materials. *Materials*, 3(5):3092–3140, 2010.

[56] Jan Prasek, Jana Drbohlavova, Jana Chomoucka, Jaromir Hubalek, Ondrej Jasek, Vojtech Adam, and Rene Kizek. Methods for carbon nanotubes synthesis. *Journal of Materials Chemistry*, 21(40):15872–15884, 2011.

[57] DS Bethune, Ch H Kiang, MS De Vries, G Gorman, R Savoy, J Vazquez, and R Beyers. Cobalt-catalysed growth of carbon nanotubes with single-atomic-layer walls. *Nature*, 363(6430):605, 1993.

[58] Zhong L Wang, Rui Ping Gao, Walt A de Heer, and P Poncharal. In situ imaging of field emission from individual carbon nanotubes and their structural damage. *Applied Physics Letters*, 80(5):856–858, 2002.

[59] Jung Inn Sohn, Seonghoon Lee, Yoon-Ho Song, Sung-Yool Choi, Kyoung-Ik Cho, and Kee-Soo Nam. Patterned selective growth of carbon nanotubes and large field emission from vertically well-aligned carbon nanotube field emitter arrays. *Applied Physics Letters*, 78(7):901–903, 2001.

[60] M Meyyappan. A review of plasma enhanced chemical vapour deposition of carbon nanotubes. *Journal of Physics D: Applied Physics*, 42(21):213001, 2009.

[61] Jiazhi Ma, John TW Yeow, James CL Chow, and Rob B Barnett. A carbon fiber-based radiation sensor for dosimetric measurement in radiotherapy. *Carbon*, 46(14):1869–1873, 2008.

[62] Xiomara Calderón-Colón, Huaizhi Geng, Bo Gao, Lei An, Guohua Cao, and Otto Zhou. A carbon nanotube field emission cathode with high current density and long-term stability. *Nanotechnology*, 20(32):325707, 2009.

[63] Sungsoo Kim, Jonghyuk Yim, Xuhua Wang, Donal DC Bradley, Soonil Lee, and John C deMello. Spin-and spray-deposited single-walled carbon-nanotube electrodes for organic solar cells. *Advanced Functional Materials*, 20(14):2310–2316, 2010.

[64] Kunitoshi Yamamoto, Seiji Akita, and Yoshikazu Nakayama. Orientation and purification of carbon nanotubes using ac electrophoresis. *Journal of physics D: Applied physics*, 31(8):L34, 1998.

[65] WB Choi, YW Jin, HY Kim, SJ Lee, MJ Yun, JH Kang, YS Choi, NS Park, NS Lee, and JM Kim. Electrophoresis deposition of carbon nanotubes for triode-type field emission display. *Applied Physics Letters*, 78(11):1547–1549, 2001.

[66] S_J Oh, J Zhang, Y Cheng, H Shimoda, and O Zhou. Liquid-phase fabrication of patterned carbon nanotube field emission cathodes. *Applied Physics Letters*, 84(19):3738–3740, 2004.

[67] Y Tu, Yuehe Lin, and ZF Ren. Nanoelectrode arrays based on low site density aligned carbon nanotubes. *Nano Letters*, 3(1):107–109, 2003.

[68] L Nilsson, O Groening, Ch Emmenegger, O Kuettel, E Schaller, L Schlapbach, H Kind, JM Bonard, and K Kern. Scanning field emission from patterned carbon nanotube films. *Applied Physics Letters*, 76(15):2071–2073, 2000.

[69] WI Milne, KBK Teo, E Minoux, O Groening, L Gangloff, L Hudanski, J-P Schnell, D Dieumegard, F Peauger, IYY Bu, et al. Aligned carbon nanotubes/fibers for applications in vacuum microwave amplifiers. *Journal of Vacuum Science & Technology B: Microelectronics and Nanometer Structures Processing, Measurement, and Phenomena*, 24(1):345–348, 2006.

[70] M Chhowalla, C Ducati, NL Rupesinghe, KBK Teo, and GAJ Amaratunga. Field emission from short and stubby vertically aligned carbon nanotubes. *Applied Physics Letters*, 79(13):2079–2081, 2001.

[71] KBK Teo, M Chhowalla, GAJ Amaratunga, WI Milne, G Pirio, P Legagneux, F Wyczisk, D Pribat, and DG Hasko. Field emission from dense, sparse, and patterned arrays of carbon nanofibers. *Applied Physics Letters*, 80(11):2011–2013, 2002.

[72] ZF Ren, ZP Huang, JW Xu, JH Wang, P Bush, MP Siegal, and PN Provencio. Synthesis of large arrays of well-aligned carbon nanotubes on glass. *Science*, 282(5391):1105–1107, 1998.

[73] ZF Ren, ZP Huang, DZ Wang, JG Wen, JW Xu, JH Wang, LE Calvet, J Chen, JF Klemic, and MA Reed. Growth of a single freestanding multiwall carbon nanotube on each nanonickel dot. *Applied Physics Letters*, 75(8):1086–1088, 1999.

[74] M Chhowalla, KBK Teo, C Ducati, NL Rupesinghe, GAJ Amaratunga, AC Ferrari, D Roy, J Robertson, and WI Milne. Growth process conditions of vertically aligned carbon nanotubes using plasma enhanced chemical vapor deposition. *Journal of Applied Physics*, 90(10):5308–5317, 2001.

[75] VI Merkulov, DH Lowndes, YY Wei, Gyula Eres, and E Voelkl. Patterned growth of individual and multiple vertically aligned carbon nanofibers. *Applied Physics Letters*, 76(24):3555–3557, 2000.

[76] MA Guillorn, Anatoli Vasilievich Melechko, Vladimir I Merkulov, Dale K Hensley, Michael L Simpson, and Douglas H Lowndes. Self-aligned gated field emission devices using single carbon nanofiber cathodes. *Applied Physics Letters*, 81(19):3660–3662, 2002.

[77] Vasile Bogdan Neculaes, Peter M Edic, Mark Frontera, Antonio Caiafa, Ge Wang, and Bruno De Man. Multisource x-ray and ct: Lessons learned and future outlook. *IEEE Access*, 2:1568–1585, 2014.

[78] KBK Teo, M Chhowalla, GAJ Amaratunga, WI Milne, P Legagneux, G Pirio, L Gangloff, D Pribat, V Semet, Vu Thien Binh, et al. Fabrication and electrical characteristics of carbon nanotube-based microcathodes for use in a parallel electron-beam lithography system. *Journal of Vacuum Science & Technology B: Microelectronics and Nanometer Structures Processing, Measurement, and Phenomena*, 21(2):693–697, 2003.

[79] AM Rao, D Jacques, RC Haddon, W Zhu, C Bower, and S Jin. In situ-grown carbon nanotube array with excellent field emission characteristics. *Applied Physics Letters*, 76(25):3813–3815, 2000.

[80] Alan M Cassell, Qi Ye, Brett A Cruden, Jun Li, Philippe C Sarrazin, Hou Tee Ng, Jie Han, and M Meyyappan. Combinatorial chips for optimizing the growth and integration of carbon nanofibre based devices. *Nanotechnology*, 15(1):9, 2003.

[81] YY Wei, Gyula Eres, VI Merkulov, and DH Lowndes. Effect of catalyst film thickness on carbon nanotube growth by selective area chemical vapor deposition. *Applied Physics Letters*, 78(10):1394–1396, 2001.

[82] Cari F Herrmann, FH Fabreguette, DS Finch, R Geiss, and SM George. Multilayer and functional coatings on carbon nanotubes using atomic layer deposition. *Applied Physics Letters*, 87(12):123110, 2005.

[83] MS Wang, L-M Peng, JY Wang, and Q Chen. Electron field emission characteristics and field evaporation of a single carbon nanotube. *The Journal of Physical Chemistry B*, 109(1):110–113, 2005.

[84] Jean-Marc Bonard, Christian Klinke, Kenneth A Dean, and Bernard F Coll. Degradation and failure of carbon nanotube field emitters. *Physical Review B*, 67(11):115406, 2003.

[85] John Cumings, Philip G Collins, and A Zettl. Materials: Peeling and sharpening multiwall nanotubes. *Nature*, 406(6796):586, 2000.

[86] Kenneth A Dean and Babu R Chalamala. Current saturation mechanisms in carbon nanotube field emitters. *Applied Physics Letters*, 76(3):375–377, 2000.

[87] Jean-Marc Bonard, Mirko Croci, Christian Klinke, Ralph Kurt, Olivier Noury, and Nicolas Weiss. Carbon nanotube films as electron field emitters. *Carbon*, 40(10):1715–1728, 2002.

[88] Seigo Kanemaru, Takayuki Hirano, Kenichi Honda, and Junji Itoh. Stable emission from a mosfet-structured emitter tip in poor vacuum. *Applied Surface Science*, 146(1-4):198–202, 1999.

[89] H Sugie, Masaki Tanemura, V Filip, K Iwata, K Takahashi, and F Okuyama. Carbon nanotubes as electron source in an X-ray tube. *Applied Physics Letters*, 78(17):2578–2580, 2001.

[90] P Sarrazin, D Blake, L Delzeit, M Meyyappan, B Boyer, S Snyder, and B Espinosa. Carbon-nanotube field emission X-ray tube for space exploration XRD/XRF instrument. *Advances in X-Ray Analysis*, 47:232–239, 2004.

[91] Je Hwang Ryu, Wan Sun Kim, Seung Ho Lee, Jung Su Kang, Jae Gon Kim, Soo Yeol Lee, Kyu Chang Park, and Hun Kuk Park. Carbon nanotube field emission X-ray system for computed tomography. In *Medical Imaging 2013: Physics of Medical Imaging*, volume 8668, page 866860. International Society for Optics and Photonics, 2013.

[92] Hae Young Choi, Chae Hwa Shon, and Jong Uk Kim. Development of new X-ray source based on carbon nanotube field emission and application to the non destructive imaging technology. *IEEE Transactions on Nuclear Science*, 56(3):1297–1300, 2009.

[93] WP Dyke and WW Dolan. Field emission. In *Advances in Electronics and Electron Physics*, volume 8, pages 89–185. Elsevier, 1956.

[94] Francis M Charbonnier, John P Barbour, and Walter P Dyke. Resolution of field-emission X-ray sources. *Radiology*, 117(1):165–172, 1975.

[95] George S Hallenbeck. Clinical evaluation of the 350-kV chest radiography system. *Radiology*, 117(1):1–4, 1975.

[96] Pelle Rangsten, Carolina Ribbing, Carola Strandman, Bertil Hök, and L Smith. Field-emitting structures intended for a miniature X-ray source. *Sensors and Actuators A: Physical*, 82(1-3):24–29, 2000.

[97] Robert R Whitlock, Michael I Bell, David V Kerns, Sherra Kerns, Jimmy L Davidson, and Weng Poo Kang. Transmission cathode for X-ray production, December 25 2001. US Patent 6,333,968.

[98] Otto Z Zhou and Jianping Lu. X-ray generating mechanism using electron field emission cathode, April 22 2003. US Patent 6,553,096.

[99] Otto Z Zhou, Jianping Lu, and Qi Qiu. Large-area individually addressable multi-beam x-ray system and method of forming same, April 5 2005. US Patent 6,876,724.

[100] GZ Yue, Q Qiu, Bo Gao, Y Cheng, J Zhang, H Shimoda, S Chang, JP Lu, and O Zhou. Generation of continuous and pulsed diagnostic imaging x-ray radiation using a carbon-nanotube-based field-emission cathode. *Applied Physics Letters*, 81(2):355–357, 2002.

[101] Jin-Woo Jeong, Jun-Tae Kang, Sungyoul Choi, Jae-Woo Kim, Seungjoon Ahn, and Yoon-Ho Song. A digital miniature x-ray tube with a high-density triode carbon nanotube field emitter. *Applied Physics Letters*, 102(2):023504, 2013.

[102] Cameron J Ritchie, J David Godwin, Carl R Crawford, William Stanford, Hirofumi Anno, and YONGMIN Kim. Minimum scan speeds for suppression of motion artifacts in CT. *Radiology*, 185(1):37–42, 1992.

[103] J Zhang, G Yang, Yuan Cheng, Bo Gao, Qi Qiu, YZ Lee, JP Lu, and Otto Zhou. Stationary scanning x-ray source based on carbon nanotube field emitters. *Applied Physics Letters*, 86(18):184104, 2005.

[104] J Zhang, Y Cheng, YZ Lee, B Gao, Q Qiu, WL Lin, D Lalush, JP Lu, and O Zhou. A nanotube-based field emission x-ray source for microcomputed tomography. *Review of Scientific Instruments*, 76(9):094301, 2005.

[105] Zejian Liu, Guang Yang, Yueh Z Lee, David Bordelon, Jianping Lu, and Otto Zhou. Carbon nanotube based microfocus field emission x-ray source for microcomputed tomography. *Applied Physics Letters*, 89(10):103111, 2006.

[106] G Cao, YZ Lee, R Peng, Z Liu, R Rajaram, X Calderon-Colon, L An, P Wang, T Phan, S Sultana, et al. A dynamic micro-ct scanner based on a carbon nanotube field emission x-ray source. *Physics in Medicine & Biology*, 54(8):2323, 2009.

[107] Emily Gidcumb, Bo Gao, Jing Shan, Christy Inscoe, Jianping Lu, and Otto Zhou. Carbon nanotube electron field emitters for x-ray imaging of human breast cancer. *Nanotechnology*, 25(24):245704, 2014.

[108] Je Hwang Ryu, Jung Su Kang, and Kyu Chang Park. Carbon nanotube electron emitter for x-ray imaging. *Materials*, 5(11):2353–2359, 2012.

[109] M Hadsell, J Zhang, P Laganis, F Sprenger, J Shan, L Zhang, L Burk, H Yuan, S Chang, J Lu, et al. A first generation compact microbeam radiation therapy system based on carbon nanotube X-ray technology. *Applied Physics Letters*, 103(18):183505, 2013.

[110] N Mail, DJ Moseley, JH Siewerdsen, and DA Jaffray. The influence of bowtie filtration on cone-beam CT image quality. *Medical Physics*, 36(1):22–32, 2009.

[111] SA Graham, DJ Moseley, JH Siewerdsen, and DA Jaffray. Compensators for dose and scatter management in cone-beam computed tomography. *Medical Physics*, 34(7):2691–2703, 2007.

[112] Steven J Bartolac. *Fluence field modulated computed tomography*. PhD thesis, 2012.

[113] J Rottmann, P Keall, and R Berbeco. Markerless EPID image guided dynamic multi-leaf collimator tracking for lung tumors. *Physics in Medicine & Biology*, 58(12):4195, 2013.

[114] Christopher J Moore, Thomas E Marchant, and Ali M Amer. Cone beam CT with zonal filters for simultaneous dose reduction, improved target contrast and automated set-up in radiotherapy. *Physics in Medicine & Biology*, 51(9):2191, 2006.

[115] Xiaoxia Yang, Zhenjun Li, Feng He, Mingju Liu, Bing Bai, Wei Liu, Xiaohui Qiu, Hang Zhou, Chi Li, and Qing Dai. Enhanced field emission from a carbon nanotube array coated with a hexagonal boron nitride thin film. *Small*, 11(30):3710–3716, 2015.

[116] DA Kurnosov, AS Baturin, AS Bugaev, KN Nikolski, RG Tchesov, and EP Sheshin. Influence of the interelectrode distance in electrophoretic cold cathode fabrication on the emission uniformity. *Applied Surface Science*, 215(1-4):232–236, 2003.

[117] Hyung Soo Uh and Sangsik Park. Improved field emission properties from carbon nanotubes grown onto micron-sized arrayed silicon pillars with pyramidal bases. *Diamond and Related Materials*, 54:74–78, 2015.

[118] B Barwinski and S Sendecki. Fine structure of scanning field emission microscope (SFEM) image. *Vacuum*, 47(12):1479–1482, 1996.

[119] Junko Yotani, Sashiro Uemura, Takeshi Nagasako, Hiroyuki Kurachi, Hiromu Yamada, Tomotaka Ezaki, Tsuyoshi Maesoba, Takehiro Nakao, Masaaki Ito, Toshiyuki Ishida, et al. Emission enhancement by excimer laser irradiation over a weblike carbon nanotube layer. *Japanese Journal of Applied Physics*, 43(11B):L1459, 2004.

[120] Hiroyuki Kurachi, Sashiro Uemura, Jyunko Yotani, Takeshi Nagasako, Hiromu Yamada, Tomotaka Ezaki, Tsuyoshi Maesoba, Takehiro Nakao, Masaaki Ito, Akira Sakurai, et al. Uniform carbon-nanotube emitter for field-emission displays. *Journal of the Society for Information Display*, 13(9):727–733, 2005.

[121] Yonghai Sun, David A Jaffray, Liang-Yih Chen, and John TW Yeow. Polymethyl methacrylate thin-film-based field emission microscope. *IEEE Transactions on Nanotechnology*, 11(3):441–443, 2012.

[122] M Drechsler. Erwin müller and the early development of field emission microscopy. *Surface Science*, 70(1):1–18, 1978.

[123] N Savvides and B Window. Electrical transport, optical properties, and structure of TiN films synthesized by low-energy ion assisted deposition. *Journal of Applied Physics*, 64(1):225–234, 1988.

[124] Koichi Hata, Akihiro Takakura, and Yahachi Saito. Field emission microscopy of adsorption and desorption of residual gas molecules on a carbon nanotube tip. *Surface Science*, 490(3):296–300, 2001.

[125] Kenneth A Dean and Babu R Chalamala. Field emission microscopy of carbon nanotube caps. *Journal of Applied Physics*, 85(7):3832–3836, 1999.

[126] Yonghai Sun, David A Jaffray, and John TW Yeow. Self-heating schottky emission from a ballasted carbon nanotube array. *Carbon*, 58:87–91, 2013.

[127] ST Purcell, P Vincent, C Journet, and Vu Thien Binh. Hot nanotubes: stable heating of individual multiwall carbon nanotubes to 2000 K induced by the field-emission current. *Physical review letters*, 88(10):105502, 2002.

[128] Tarek Ragab and Cemal Basaran. Joule heating in single-walled carbon nanotubes. *Journal of Applied Physics*, 106(6):063705, 2009.

[129] Yunhan Li, Yonghai Sun, David A Jaffray, and John TW Yeow. A novel field emission microscopy method to study field emission characteristics of freestanding carbon nanotube arrays. *Nanotechnology*, 28(15):155704, 2017.

[130] Th Döppner, Th Fennel, Th Diederich, J Tiggesbäumker, and KH Meiwes-Broer. Controlling the Coulomb explosion of silver clusters by femtosecond dual-pulse laser excitation. *Physical Review Letters*, 94(1):013401, 2005.

[131] Seiji Shimizu, Vasilii Zhakhovskii, Fuminobu Sato, Shinichiro Okihara, Shuji Sakabe, Katsunobu Nishihara, Yasakazu Izawa, Tomoyuki Yatsuhashi, and Nobuaki Nakashima. Coulomb explosion of benzene induced by an intense laser field. *The Journal of Chemical Physics*, 117(7):3180–3189, 2002.

[132] B Manschwetus, T Nubbemeyer, K Gorling, G Steinmeyer, U Eichmann, H Rottke, and W Sandner. Strong laser field fragmentation of H2: Coulomb explosion without double ionization. *Physical Review Letters*, 102(11):113002, 2009.

[133] Xianlong Wei, Dai-Ming Tang, Qing Chen, Yoshio Bando, and Dmitri Golberg. Local Coulomb explosion of boron nitride nanotubes under electron beam irradiation. *ACS Nano*, 7(4):3491–3497, 2013.

[134] M Lenner, A Kaplan, and RE Palmer. Nanoscopic Coulomb explosion in ultrafast graphite ablation. *Applied Physics Letters*, 90(15):153119, 2007.

[135] Philip E Mason, Frank Uhlig, Václav Vaněk, Tillmann Buttersack, Sigurd Bauerecker, and Pavel Jungwirth. Coulomb explosion during the early stages of the reaction of alkali metals with water. *Nature Chemistry*, 7(3):250, 2015.

[136] Richard Neutze, Remco Wouts, David van der Spoel, Edgar Weckert, and Janos Hajdu. Potential for biomolecular imaging with femtosecond X-ray pulses. *Nature*, 406(6797):752, 2000.

[137] WI Milne, KBK Teo, M Chhowalla, GAJ Amaratunga, SB Lee, DG Hasko, H Ahmed, O Groening, P Legagneux, L Gangloff, et al. Electrical and field emission investigation of individual carbon nanotubes from plasma enhanced chemical vapour deposition. *Diamond and Related Materials*, 12(3-7):422–428, 2003.

[138] Seong Gon Kim, Young Hee Lee, Peter Nordlander, and David Tománek. Disintegration of finite carbon chains in electric fields. *Chemical Physics Letters*, 264(3-4):345–350, 1997.

[139] Lord Rayleigh. XX. On the equilibrium of liquid conducting masses charged with electricity. *The London, Edinburgh, and Dublin Philosophical Magazine and Journal of Science*, 14(87):184–186, 1882.

[140] Olof Echt, Paul Scheier, and Tilmann D Märk. Multiply charged clusters. *Comptes Rendus Physique*, 3(3):353–364, 2002.

[141] S Nuriel, L Liu, AH Barber, and HD Wagner. Direct measurement of multiwall nanotube surface tension. *Chemical Physics Letters*, 404(4-6):263–266, 2005.

[142] Kosuke Nagashio, Tomonori Nishimura, Koji Kita, and Akira Toriumi. Mobility variations in mono-and multi-layer graphene films. *Applied Physics Express*, 2(2):025003, 2009.

[143] Guangtong Liu, Yuanchun Zhao, Kaihong Zheng, Zheng Liu, Wenjun Ma, Yan Ren, Sishen Xie, and Lianfeng Sun. Coulomb explosion: a novel approach to separate single-walled carbon nanotubes from their bundle. *Nano Letters*, 9(1):239–244, 2008.

[144] JF Widmann, CL Aardahl, and EJ Davis. Observations of non-Rayleigh limit explosions of electrodynamically levitated microdroplets. *Aerosol Science and Technology*, 27(5):636–648, 1997.

[145] Isidore Last, Yaakov Levy, and Joshua Jortner. Beyond the Rayleigh instability limit for multicharged finite systems: From fission to Coulomb explosion. *Proceedings of the National Academy of Sciences*, 99(14):9107–9112, 2002.

[146] J-M Bonard, J-P Salvetat, T Stöckli, L Forro, and A Chatelain. Field emission from carbon nanotubes: perspectives for applications and clues to the emission mechanism. *Applied Physics A*, 69(3):245–254, 1999.

[147] X Jack Hu, Antonio A Padilla, Jun Xu, Timothy S Fisher, and Kenneth E Goodson. 3-omega measurements of vertically oriented carbon nanotubes on silicon. *Journal of Heat Transfer*, 128(11):1109–1113, 2006.

[148] Lan Zhang, Derek Austin, Vladimir I Merkulov, Anatoli V Meleshko, Kate L Klein, Michael A Guillorn, Douglas H Lowndes, and Michael L Simpson. Four-probe charge transport measurements on individual vertically aligned carbon nanofibers. *Applied Physics Letters*, 84(20):3972–3974, 2004.

[149] Kaiwang Zhang, G Malcolm Stocks, and Jianxin Zhong. Melting and premelting of carbon nanotubes. *Nanotechnology*, 18(28):285703, 2007.

[150] Clarence H Hinrichs, William A Mackie, Philip A Pincosy, and PETER Poulsen. The extended Schottky cathode. *IEEE Transactions on Electron Devices*, 37(12):2575–2580, 1990.

[151] Yunhan Li, Yonghai Sun, David A Jaffray, and John TW Yeow. Coulomb explosion of vertically aligned carbon nanofibre induced by field electron emission. *RSC Advances*, 7(64):40470–40479, 2017.

[152] Zhenjun Li, Xiaoxia Yang, Feng He, Bing Bai, Hang Zhou, Chi Li, and Qing Dai. High current field emission from individual non-linear resistor ballasted carbon nanotube cluster array. *Carbon*, 89:1–7, 2015.

[153] A Haga, S Senda, Y Sakai, Y Mizuta, S Kita, and F Okuyama. A miniature x-ray tube. *Applied Physics Letters*, 84(12):2208–2210, 2004.

[154] Jun-Tae Kang, Hyeong-Rag Lee, Jin-Woo Jeong, Jae-Woo Kim, Sora Park, Min-Sik Shin, Ji-Hwan Yeon, Hyojin Jeon, Sung-Hee Kim, Young Chul Choi, et al. Fast and stable operation of carbon nanotube field-emission X-ray tubes achieved using an advanced active-current control. *IEEE Electron Device Letters*, 36(11):1209–1211, 2015.

[155] Jae-Woo Kim, Min-Sik Shin, Jin-Woo Jeong, Jun-Tae Kang, Sungyoul Choi, Sora Park, Ji-Hwan Yeon, Seungjoon Ahn, and Yoon-Ho Song. Electrostatic focusing lens module with large focusing capability in carbon nanotube emitter-based X-ray sources. *IEEE Electron Device Letters*, 36(4):396–398, 2015.

[156] EA Litvinov. Theory of explosive electron emission. *IEEE Transactions on Electrical Insulation*, (4):683–689, 1985.

[157] Nikolay Egorov and Evgeny Sheshin. *Field emission electronics*, volume 60. Springer, 2017.

[158] Masashi Shiraishi and Masafumi Ata. Work function of carbon nanotubes. *Carbon*, 39(12):1913–1917, 2001.

[159] Ravindra Arora and Wolfgang Mosch. *High voltage and electrical insulation engineering*, volume 69. John Wiley & Sons, 2011.

[160] Lassner Erik and Schubert Wolf-Dieter. Tungsten: properties, chemistry, technology of the element, alloys, and chemical compounds, 1999.

[161] Robert D Allen, Louis F Glasier Jr, and Paul L Jordan. Spectral emissivity, total emissivity, and thermal conductivity of molybdenum, tantalum, and tungsten above 2300 k. *Journal of Applied Physics*, 31(8):1382–1387, 1960.

[162] CT Badea, M Drangova, David W Holdsworth, and GA Johnson. In vivo small-animal imaging using micro-ct and digital subtraction angiography. *Physics in Medicine & Biology*, 53(19):R319, 2008.

[163] Michael J Flynn, Sean M Hames, David A Reimann, and Scott J Wilderman. Microfocus x-ray sources for 3D microtomography. *Nuclear Instruments and Methods in Physics Research Section A: Accelerators, Spectrometers, Detectors and Associated Equipment*, 353(1-3):312–315, 1994.

[164] J Baro, J Sempau, JM Fernández-Varea, and F Salvat. PENELOPE: an algorithm for Monte Carlo simulation of the penetration and energy loss of electrons and positrons in matter. *Nuclear Instruments and Methods in Physics Research Section B: Beam Interactions with Materials and Atoms*, 100(1):31–46, 1995.

[165] J Stepanek, H Blattmann, JA Laissue, N Lyubimova, M Di Michiel, and DN Slatkin. Physics study of microbeam radiation therapy with PSI-version of Monte Carlo code GEANT as a new computational tool. *Medical Physics*, 27(7):1664–1675, 2000.

[166] M De Felici, R Felici, M Sanchez del Rio, C Ferrero, T Bacarian, and FA Dilmanian. Dose distribution from x-ray microbeam arrays applied to radiation therapy: An EGS4 Monte Carlo study. *Medical Physics*, 32(8):2455–2463, 2005.